

**Department of Chemical Engineering**

**Local Bubble Hydrodynamics in Multiphase Stirred Tanks**

**Baranivignesh Prakash**

**This thesis is presented for the Degree of**

**Doctor of Philosophy**


**of**

**Curtin University**

**January 2018**

## Declaration

To the best of my knowledge and belief this thesis contains no material previously published by any other person except where due acknowledgment has been made. This thesis contains no material which has been accepted for the award of any other degree or diploma in any university.

Signature: 

Date: 21-01-2018

## **Acknowledgements**

First and foremost, I would like to express my gratitude to my supervisor, Dr Ranjeet Utikar for his guidance, encouragement, and for giving me a lot of freedom in my research. I would also like to thank him for his mentorship and time when most needed. I am indebted to him for his efforts in improving my communication skills, and constructive criticism on my work which helped me to understand the complexity of multiphase systems.

I am grateful to Dr Milinkumar Shah, for his support and all the productive conversations we had throughout my research. I would also like to thank him for his valuable suggestions, and time during the early stages of this research especially for optical probe signal processing. I would also like to thank Prof Vishnu Pareek, for giving me the opportunity, support and facilities to carry out this research. My special thanks to Mr Bill Baguley, for his valuable inputs and allowing me to carry out scale up studies at MIXTEC Australia.

I undoubtedly owe a lot to Araya, Jimmy, Andrew, Lyon and Ross for their outstanding support to set up B001 laboratory and to complete my experiments on time. I would also like to thank Evelyn, Lemlem and Randal for their assistance during the tenure of my work. My acknowledgement extends to Dr Divyamaan, Dr Harisinh, and Dr Tejas for their valuable suggestions in CFD studies. I appreciate the help provided by Vishal Chaugule, for his insightful suggestions in PIV experiments. I would also like to acknowledge the financial assistance (CIPRS) provided by Department of Chemical Engineering, Curtin University during my PhD.

Lastly, I would like to thank my family and friends for their love, support, and encouragement.

## **Abstract**

Multiphase stirred tanks are commonly used in various industries for gas dispersion applications owing to their good heat and mass transfer characteristics. To improve the gas dispersion efficiency in stirred tanks, knowledge on the spatial distribution of dispersed phase on a continuous phase is essential. The present work serves to understand the local bubble hydrodynamics of multiphase stirred tanks under various operating and geometric conditions.

Exhaustive research has been done on gas-liquid stirred tanks to understand gas phase hydrodynamics. However, most of the previous work has focused on the effect of operating conditions, and impeller geometry on overall gas holdup. Very few reports have intended to examine local bubble hydrodynamics (bubble size, bubble velocity, and gas hold up). Nevertheless, the results were mostly confined to dilute gas flow conditions, and lab scale experiments due to limitation in measurement techniques. It has been emphasized that a reliable measurement technique is required to measure and analyze local bubble hydrodynamics. In this thesis optical probes are used to obtain detailed spatial data on the local bubble hydrodynamics. The measurement obtained by optical probes are initially validated using PIV and high speed imaging. The optical probes are then used under dense gas flow conditions in two and three phase systems. The optical probe system is then used to understand the local bubble hydrodynamics of two and three phase systems in baffled and unbaffled stirred tanks.

The optical probes were employed to simultaneously measure liquid/solid velocities and local bubble hydrodynamics in a slurry bubble column. In addition, liquid velocity, and bubble chord length obtained from probe measurements were successfully validated using PIV, and high speed imaging techniques. Discrepancies on liquid velocity, and chord length were confined within 13% and 8% respectively and thus, optical probe technique was deemed suitable to measure local hydrodynamics in stirred tanks.

Prior to employing probe in highly turbulent pilot scale baffled stirred tank, additional measurements were carried out in a lab scale unbaffled stirred tank. Vortex ingestion in unbaffled tanks governs the local bubble hydrodynamics and therefore effect of

impeller speed on vortex shape, and gas holdup, and bubble size was investigated. Furthermore, to understand the impact of vortex shape on gas-liquid dynamics, volume of fluid simulations were carried out. It was observed that tangential velocities play a major role in dictating the vortex shape, and its free surface movement. With vortex ingestion, impeller generated significantly higher axial, and radial flow due to the presence of recirculation loops above and below the blades.

Measurements were then carried out in a pilot scale baffled stirred tank equipped with either standard Rushton turbine (SRT) or high solidity pitched blade turbine (HSPBT). For SRT experiments, effect of solid loading on local bubble hydrodynamics was investigated. It was observed that, power dissipated from impeller was mostly used for suspending solids rather than to impart shear on bubbles. Subsequently, bubble size, and gas phase velocities increased causing reduction in gas holdup. Furthermore, the influence of impeller diameter on local bubble dynamics was examined. Blade width, and length proportionately increased with increase in diameter. This led to more contact area between blades and gas phase causing enhanced gas dispersion. In HSPBT experiments, the impact of blade angle on power consumption and local bubble hydrodynamics was studied. Increase in blade angle increased overall gas holdup, and gas fraction of larger bubbles at the expense of power consumption. Significant amount of finer bubbles were found to concentrate below the impeller trailing edge and tank centre than wall. It was also observed that based on the bubble population classification, HSPBT45 generated more finer bubbles.

The results presented in this thesis are crucial in enhancing the understanding of bubble flow in multiphase stirred tank and would be invaluable for CFD model validation, design and scale up.

# Publications

## Peer reviewed journal publications

Prakash, B., M. T. Shah, V. K. Pareek and R. P. Utikar (2017). "Impact of HSPBT blade angle on gas phase hydrodynamics in a gas-liquid stirred tank." Chemical Engineering Research and Design.

Prakash, B., D. Wadnerkar, T. Bhatelia, M. T. Shah, V. K. Pareek and R. P. Utikar. "Effect of vortex ingestion on gas-liquid dynamics in unbaffled stirred tank." The Candian Journal of Chemical Engineering, (under review), 2018.

Prakash, B., H Parmar, M. T. Shah, V. K. Pareek and R. P. Utikar. "Simultaneous measurements of local bubble hydrodynamics and particle velocities using optical probe." Industrial & Engineering Chemistry Research, (to be submitted), 2018.

## Conference proceedings

Prakash, B., M. T. Shah, V. K. Pareek and R. P. Utikar (2016). "Optical Measurements of Local Bubble Characteristics in Gas-Liquid Stirred Tank Equipped with Axial Impellers." Proceedings of 24th International Symposium on Chemical Reaction Engineering Conference, Minnesota, USA.

# Table of contents

Acknowledgments		i
Abstract		ii
Publications		iv
Nomenclature		x
List of Figures		xv
List of Tables		xx
<b>Chapter 1</b>	<b>Introduction</b>	
1.1	Introduction	1
1.2	Motivation	2
1.3	Research objectives	4
1.4	Thesis layout	4
<b>Chapter 2</b>	<b>Literature review</b>	
2.1	Flow characteristics of baffled stirred tanks	6
2.1.1	Basic definitions	6
2.1.2	Operating regimes and power consumption	7
2.1.3	Flow patterns	9
2.1.4	Gas phase hydrodynamics	10

2.1.5	Local bubble hydrodynamics	17
2.2	Unbaffled stirred tanks	23
2.3	Selection of multiphase flow measurement technique	28
2.5	Summary	28
<b>Chapter 3</b>	<b>Simultaneous measurements of local bubble dynamics and particle velocities using optical probe</b>	
3.1	Introduction	30
3.2	Experimental setup	30
3.3	Measurement techniques	33
3.3.1	Optical probe	33
3.3.2	High speed imaging	37
3.3.3	Particle image velocimetry	39
3.4	Results and discussion	40
3.4.1	Validation of optical probe measurements	40
3.4.2	Liquid velocity profiles	43
3.4.3	Simultaneous measurements of local bubble dynamics and particle velocities	46
3.5	Summary	50
<b>Chapter 4</b>	<b>Vortex shape and gas-liquid dynamics in unbaffled stirred tank</b>	
4.1	Introduction	52



4.2	Materials and methods	53
4.2.1	Experimental setup	53
4.2.2	CFD model and simulation setup	53
4.3	Results and discussion	58
4.3.1	Vortex shape	58
4.3.2	Gas-liquid velocity distribution	61
4.3.3	Local gas holdup and bubble chord length distribution	63
4.4	Summary	66
<b>Chapter 5</b>	<b>Local bubble hydrodynamics in baffled stirred tanks</b>	
5.1	Introduction	67
5.2	Experimental setup & operating conditions	69
5.2.1	GLS-ST with SRT	69
5.2.2	GL-ST with RT	70
5.2.3	GL-ST with HSPBT	71
5.3	Results and discussions	73
5.3.1	GLS-ST with SRT	73
	Local bubble hydrodynamics in GL-ST	73
	Particle velocity distribution in GLS-ST	78
	Local bubble dynamics in GLS-ST	79
5.3.2	GL-ST with RT	81

	Flow regime identification	81
	Effect of impeller speed and D/T	84
	Effect of superficial gas velocity	85
	Power consumption	87
5.3.3	GL-ST with HSPBT	88
	Overall gas holdup	89
	Power spectra analysis	90
	Local bubble dynamics	92
	Bubble population classification	95
	Power consumption	96
5.4	Summary	100
<b>Chapter 6</b>	<b>Conclusions and future work</b>	
6.1	Conclusions	103
6.1.1	Simultaneous measurements of local bubble dynamics and particle velocities using optical probe	103
6.1.2	Vortex ingestion in unbaffled tank	104
6.1.3	Local bubble hydrodynamics in baffled stirred tanks	105
6.2	Recommendations for future work	106
	<b>References</b>	109



# Nomenclature

## Symbols

$\varepsilon_G$	Global gas holdup, %
$\varepsilon_g$	Local gas holdup, %
$h_g$	Change in liquid height with aeration, m
$m_G$	Mass fraction of gas phase in flow domain, dimensionless
$m_L$	Mass fraction of liquid phase in flow domain, dimensionless
$N_a$	Aeration number, dimensionless
$N_p$	Impeller power number
$N_{we}$	Weber number, dimensionless
$U_g$	Superficial gas velocity, m/s
$U_L$	Superficial liquid velocity, m/s
$\mu_G$	Gas viscosity, kg/ms
$\mu_L$	Liquid viscosity, kg/ms
$\mu_t$	Turbulence viscosity, kg/ms
$\rho_G$	Density of gas phase, kg/m <sup>3</sup>
$\rho_L$	Density of liquid phase, kg/m <sup>3</sup>
$\varepsilon_G$	Volume fraction of gas phase in flow domain, dimensionless
$\varepsilon_L$	Volume fraction of liquid phase in flow domain, dimensionless

$\lambda$	Wavelength of laser, nm
B	Baffle width, m
C	Impeller clearance from the bottom of tank, m
$C_o$	Courant number, dimensionless
D	Impeller diameter, m
E	Experimental results
$\varepsilon$	Rate of dissipation of turbulent kinetic energy, $m^2/s^3$
f	Doppler frequency, Hz
$F_b$	Bubble frequency, 1/s
$F_v$	Volume force, $kgm/s^2$
g	Gravitational constant, m/s
$G_b$	Generation of turbulent kinetic energy due to buoyancy, $m^2/s^2$
$G_k$	Generation of turbulent kinetic energy due to mean velocity gradients, $m^2/s^2$
H	Height of the tank, m
h	Change in liquid height without aeration, m
$H_L$	Liquid height inside the tank, m
k	Turbulent kinetic energy, $m^2/s^2$
K	Interface curvature, dimensionless
L	Blade length, m
n	Refractive index of medium

N	Impeller speed, rpm or rps
$N_{tip}$	Impeller tip velocity, m/s
P	Impeller power input, W
$\phi$	Chord length, cm
Q	Gas flow rate, m <sup>3</sup> /s
R	Tank radius, m
r	radial position from the centre of the tank towards wall, m
R	Tank radius, m
r/R	Dimensionless radial coordinate of vortex
S	Simulation results
s	Modulus of the mean rate of strain tensor
T	Tank internal diameter, m
t	Time step, s
$T_G$	Residence time, s
$T_T$	Total measurement time, s
$u_\theta$	Mean tangential velocity, m/s
$u_r$	Mean radial velocity, m/s
$u_y$	Mean axial velocity, m/s
V	Liquid velocity magnitude, m/s
$V_b$	Bubble velocity, cm/s

$V_p$	Particle velocity, m/s
$W$	Blade width, m
$X$	Distance from wall (left) for 2D column, m
$Y$	Axial distance from distributor plate for 2D column, m
$Z$	Axial distance from tank bottom for probe measurements, m
$z$	Axial distance from unbaffled tank bottom, m
$z/H$	Dimensionless axial coordinate of vortex
$\Delta x$	mesh width, m
$\rho$	Density of water, kg/m <sup>3</sup>
$\sigma$	Surface tension coefficient, N/m

### **Abbreviations**

AIP	Above impeller plane
BIP	Below impeller plane
BSD	Bubble size distribution
CFD	Computational fluid dynamics
Fl	Flow number
Fr	Froude number
GL	Gas-liquid bubble column experiments
GLS-20 $\mu$	Slurry bubble column experiments with 20 $\mu$ seeding particles

GLS-350 $\mu$	Slurry bubble column experiments with 350 $\mu$ fine sand
GLS-ST	Gas-liquid-solid stirred tank
GL-ST	Gas-liquid stirred tank
HSI	High speed imaging
HSPBT	High solidity pitched blade turbine
ID	Internal diameter
IP	Impeller plane
PIV	Particle image velocimetry
QUICK	Quadratic upstream interpolation for convective kinetics
RSM	Reynolds stress model
RT	Rushton turbine
SIMPLE	Semi-implicit method for pressure-linked equations
SL-ST	Solid-liquid stirred tank
SRT	Standard Rushton turbine
VOF	Volume of fluid
vvm	volume of air per volume of medium per minute



# List of Figures

<b>Figure no.</b>	<b>Figure title</b>	<b>Page no.</b>
1.1	Flowchart explaining the factors influencing local bubble hydrodynamics	1
2.1	Schematic representation of flow patterns in GL-ST	7
2.2	Plot for power number as a function of flow number at constant gas superficial velocity	8
2.3	Flow patterns generated by (a) radial and (b) axial impeller	9
2.4	Gas dispersion impellers	11
2.5	vortex shape (a) without vortex ingestion and (b) with vortex ingestion	24
2.6	Vortex formation in an unbaffled stirred tank	33
3.1	Schematic of (a) experimented pseudo rectangular column with optical probe measurement locations; (b) distributor plate and (c) PIV field of view	31
3.2	Optical probes used in this study	33
3.3	(a) Optical probe signal in a gas-liquid-solid system; (b) Signal for probe piercing a bubble; (c) Signal when probe encounters a particle; (d) Signal for probe piercing a bubble close to normal; (e) Partially developed voltage signal due to improper piercing; (f) Voltage fluctuation at exit for valid bubble (distinct oscillations with more than 10 fringes) and (g) Voltage fluctuation at exit for invalid	36

bubble (distinct oscillations with less than 10 fringes) [ $U_L$   
= 0.013 m/s;  $U_G$  = 0.25 m/s]

3.4	(a) Snapshots of an optical probe tip piercing a single bubble; (b) voltage signal of a bubble exhibiting three characteristics points (A-C) and (c) post-processing of the pierced bubble using ImageJ software	38
3.5	(a) Comparison of chord lengths calculated using high speed imaging and optical probe techniques and (b) & (c) comparison of velocity magnitudes with and without probe (Y3 & Frame-2) at different superficial liquid velocity	42
3.6	Variation of seeding particle velocity magnitudes with (a) axial locations (fixed $U_L$ = 0.033 m/s) and (b) $U_L$ on (fixed $Y$ = 0.40 m)	44
3.7	Recirculation loops observed near inlet	46
3.8	Effect of addition of solids and particle size on local bubble hydrodynamics in slurry bubble column	47
3.9	Effect of particle size on bubble & particle velocity and (b) bubble and particle velocity distribution	48
3.10	Normalized voltage distribution for Case-1 and Case-2	49
4.1	Schematic diagram and geometrical configuration of the experimental setup and (b) Illustration of straight and bent probe configurations	53
4.2	Computational domain and grid distribution	56

4.3	(a) Grid independency test ( $N = 500$ rpm) and (b) comparison of turbulence models ( $N = 800$ rpm) with optical probe measurements	57
4.4	Instantaneous photographs of vortex shape (a) without vortex ingestion and (b) with vortex ingestion	58
4.5	Effect of impeller speed on vortex shape (a) without vortex ingestion; (b) with vortex ingestion	60
4.6	Velocity profiles at different axial heights ( $N = 700$ rpm)	62
4.7	(a) Axial profiles of gas holdup and (b) path lines (coloured by phases: red-water; yellow-air) of bubbles released from impeller plane ( $Z = 0.08$ m)	64
4.8	(a) Axial profiles of chord length and (b) chord length distribution at impeller plane ( $z = 0.08$ m)	65
5.1	Schematic diagram and geometrical configuration of the experimental setup	69
5.2	RTs used in this study	70
5.3	(a) Schematic diagram and geometrical configuration (b) HSPBTs used in this study	71
5.4	(a) Probe tip facing upwards and downwards and (b) Effect of probe orientation on local gas holdup [HSPBT30°; $N = 425$ rpm ; $u_g = 0.013$ m/s ]	72
5.5	(a) Flow pattern in stirred tank equipped with SRT and (b-d) radial profiles of time-averaged gas holdup	74

5.6	Distribution of bubble chord length at various axial locations	76
5.7	Distribution of gas phase velocity at various axial locations	77
5.8	Effect of impeller speed on particle velocity distribution at IP ( $Y = 0.15$ m)	79
5.9	Effect of solid loading on local bubble dynamics at IP ( $Y = 0.15$ m)	81
5.10	Identification of operating regimes using optical probe	82
5.11	Effect of impeller diameter and speed on gas dispersion ( $U_g = 0.0156$ m/s)	84
5.12	Effect of gas superficial velocity and impeller speed on gas dispersion ( $D/T = 0.36$ )	86
5.13	Effect of impeller diameter and speed on power consumption ( $U_g = 0.0156$ m/s)	87
5.14	Instantaneous photographs for three blade angles [ $N = 425$ rpm; $u_g = 0.013$ m/s; $N_p(30^\circ) = 1.2$ ; $N_p(45^\circ) = 2.5$ and $N_p(60^\circ) = 3.2$ ]	88
5.15	Effect of (a) Impeller speed ( $u_g = 0.013$ m/s) and (b) Superficial gas velocity ( $N = 525$ rpm) on overall gas holdup [ $N_p(30^\circ) = 1.2$ ; $N_p(45^\circ) = 2.5$ and $N_p(60^\circ) = 3.2$ ]	89
5.16	(a) Influence of blade angle on time-averaged bubble frequency; (b) PSD for HSPBT30°; (c) Effect of blade angle on PSD [ $N = 425$ rpm; $u_g = 0.013$ m/s; $N_p(30^\circ) = 1.2$ ; $N_p(45^\circ) = 2.5$ and $N_p(60^\circ) = 3.2$ ]	90

5.17	Influence of blade angle on (a) Gas phase velocity and (b) Chord length [N = 425 rpm; $u_g = 0.013$ m/s; $N_p(30^\circ) = 1.2$ ; $N_p(45^\circ) = 2.5$ and $N_p(60^\circ) = 3.2$ ]	93
5.18	Effect of blade angle on chord length distribution (a) $r/R = 0.8$ ; (b) $r/R = 0.4$ ; (c) $r/R = 0$	94
5.19	Bubble size classification (HSPBT60°) [ $N_p(30^\circ) = 1.2$ ; $N_p(45^\circ) = 2.5$ and $N_p(60^\circ) = 3.2$ ]	96
5.20	Influence of (a) impeller speed and (b) superficial gas velocity on power consumption, (c) Effect of superficial gas velocity and power number on gas holdup and bubble chord length	98
5.21	(a) Model predicted holdup vs. experimental holdup and (b) Comparison of gas holdup between proposed model and model from literature	99

## List of Tables

<b>Table no.</b>	<b>Table title</b>	<b>Page no.</b>
2.1	Previous experimental studies on gas-liquid stirred tanks with measurements of gas phase hydrodynamics	12
2.2	Empirical correlations to predict gas holdup	17
2.3	Previous experimental * and CFD # studies on gas-liquid unbaffled tank	26
3.1	Operating Parameters and measurement locations	33
3.2	PIV parameters	40
4.1	Governing equations for VOF and turbulence models	54

# Chapter 1

## Introduction

### 1.1 INTRODUCTION

Stirred tanks are widely employed in chemical, petrochemical, pharmaceutical and mineral processing industries for gas dispersion applications (1-3). In these tanks, mass transfer between gas and liquid phase is often the rate-limiting step and a key parameter in design, and scale-up. In order to quantify the mass transfer rate, investigation on local bubble hydrodynamics which includes gas hold-up, interfacial area, bubble size, and velocity distribution along with operating regime, and phase velocities is crucial (1, 4). This work is focussed on understanding the local gas phase hydrodynamics in stirred tanks. The spatial distribution of local hydrodynamics inside a stirred tank is governed by impeller geometry, operating parameters, and physical properties of the phases as shown in Figure-1.1.

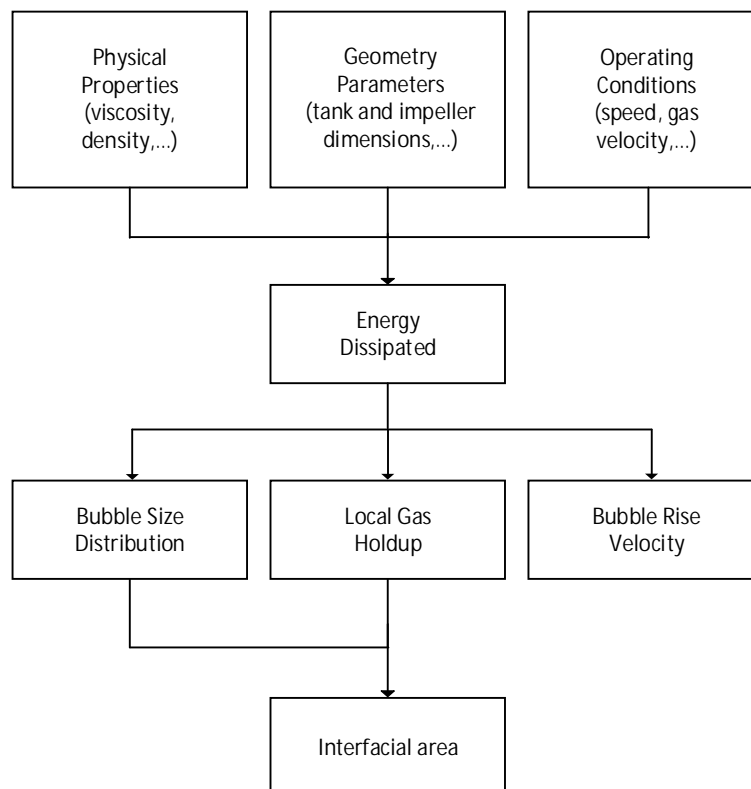


Figure-1.1: Flowchart explaining the factors influencing local bubble hydrodynamics

All these parameters affect the energy dissipated in the stirred tank. The dissipated energy is used for mixing, as well as gas/solids dispersion and affect local gas holdup, and bubble rise velocity which in turn govern the interfacial area, and the mass transfer between the gas and liquid.

## **1.2 MOTIVATION**

Over the past few decades researchers have extensively investigated the hydrodynamics of multiphase stirred tanks with an objective to maximize mass transfer efficiency, and reduce power consumption. Subsequently, empirical correlations were developed (5-9) which primarily relates overall gas holdup, or power consumption to the operating conditions and impeller geometry. However, these empirical correlations alone are not sufficient to gain a superior understanding of the local gas-liquid dynamics which dictates mass transfer rate. Consequently, numerous experimental and computational studies have been carried out in gas-liquid stirred tanks (GL-STs) to explore local hydrodynamics but mainly focussing on the measurement of liquid phase in the presence of gas bubbles (10-13). However, only few studies have reported local bubble hydrodynamics in stirred tanks (14-17). Moreover, studies on gas-liquid-solid stirred tanks (GLS-STs) have been focused on the effect of operating conditions and impeller geometry on power consumption. GLS-STs are very common in the chemical process industries for applications such as Fischer-Tropsch synthesis, polymer production, bioleaching of ores and catalytic hydrogenation (18-20). Typically in GLS-STs the percentage of solid loading varies from 5 to 50% by weight depending on the size of solid particles (21). To the best of authors' knowledge, only Yang et al., (22) has reported time-averaged local gas holdup and bubble size in a GLS-ST. Majority of the industrial stirred tanks are GLS-STs in which the addition of solid phase significantly alters the flow field and hydrodynamics. Local hydrodynamics of GLS-STs cannot be quantified by using GL-ST data which further limits the optimised design of multiphase stirred tanks for industrial application. On the other hand, computational fluid dynamics (CFD) models were developed and validated to examine the flow patterns and phase velocities in stirred tanks vastly for single phase flow. For multiphase flow, knowledge of spatial distribution of gas phase is essential for CFD models to evaluate momentum exchange by drag forces on the bubbles. Lack of experimental data on bubble size distribution



for validation of CFD models to predict local gas-liquid dynamics have been pointed out many researchers (14, 23-25).

Measurement technique is one of the key factors for limited measurements on local hydrodynamics in stirred tanks (14, 24, 26). Majority of the experimental techniques such as particle image velocimetry, phase anemometry (27, 28) can be employed only at low gas holdup (less than 10%), and demands transparent columns. But, almost all industrial stirred reactors are opaque, and operates at dense gas flow conditions (gas holdup greater than 10%). Consequently, researchers have developed advanced measurement techniques such as X-ray tomography, radioactive particle tracking (4, 29, 30) which are capable of scanning the opaque reactors. However, these techniques suffers from radiation hazards, high cost, complex calibration and poor post processing methods. Therefore, relatively simple, and inexpensive techniques such as needle probes (24, 25) which can be used in opaque column, and at dense flow conditions have been also employed in multiphase stirred tank to measure local bubble hydrodynamics. However needle probes also suffer from few limitations such as intrusive nature, delicate probe tip that erodes over the time, impact angle of the bubble/particle and size, velocity, and concentration of the solid particles.

Recently, unbaffled tanks have been identified as a possible alternative to sparged baffled tanks for bioreactor applications due to slow mixing times, relatively small gas transfer rates and less power consumption (31-33). In unbaffled stirred tanks, centrifugal forces increase the angular velocity of liquid leading to a greater deformation of free liquid surface and vortex ingestion which dictates the interface area between phases and overall hydrodynamics. However, existing information on unbaffled tanks is limited to vortex shape and hydrodynamics for a single phase system without vortex ingestion. Detailed data on gas phase hydrodynamics would be invaluable for design and scale up of unbaffled tanks.

To summarise, detailed data on local bubble hydrodynamics for GL and GLS STs is limited due to shortcomings of experimental techniques. Such data and its thorough analysis to understand the spatial distribution is essential for optimisation of stirred tanks, CFD modelling, and scale-up.

### **1.3 RESEARCH OBJECTIVES**

The major aim of this work is to provide a better understanding of local bubble hydrodynamics in multiphase stirred tanks using advanced optical probe measurement technique. Based on that, following objectives are formulated:

1. Validate the measurements from optical probe technique using particle image velocimetry and high speed imaging.
2. Verify the potential of optical probe to measure local bubble hydrodynamics and particle velocities at dense gas flow conditions and in a GLS system using slurry bubble column experiments.
3. Investigate the effect of vortex ingestion on gas-liquid dynamics in unbaffled stirred tank using optical probe measurements and CFD simulations.
4. Examine the effect of operating conditions, solid loading, and impeller geometry on local bubble hydrodynamics, and power consumption in baffled stirred tanks.

### **1.4 THESIS LAYOUT**

This thesis is assembled in 5 chapters in following manner upon the above research objectives

Chapter-1: Brief introduction to local bubble hydrodynamics in stirred tanks, motivation and research objectives are described.

Chapter-2: Hydrodynamics of baffled stirred tanks that includes operating regimes, flow patterns, gas holdup and bubble size distribution, and power consumption are explained. Further, comprehensive literature review on the experimental and numerical studies carried out in baffled and unbaffled stirred tanks to investigate gas phase hydrodynamics are presented. Chapter-2 also explains the measurement techniques available for hydrodynamic studies in multiphase stirred tanks followed by the basis for selection of optical probe technique is presented.

Chapter-3: Details of the optical probe measurement technique and signal analysis are explained. Preliminary experiments to validate optical probe measurements are discussed. In these experiments the flow in a pseudo 2D rectangular column is measured using three different methods, namely, optical probes, particle image velocimetry (PIV), and high speed imaging. Further, measurements and analysis of

local bubble dynamics in a dense bubble column and simultaneous measurements of particle velocities and local bubble dynamics in a slurry bubble column are presented.

Chapter-4: Experimental and numerical study on the effect of vortex ingestion on gas-liquid dynamics in a lab scale unbaffled tank is presented. Experiments to measure vortex coordinates and local bubble hydrodynamics carried out using optical probe measurements are explained. Further, volume of fluid simulations to investigate the effect of vortex on gas-liquid dynamics are presented.

Chapter-5: Experimental studies in a pilot scale baffled stirred tank focusing on the effect of operating conditions, solid loading and impeller geometry on local bubble hydrodynamics and power consumption are discussed. For ease of understanding materials and methods, and results and discussion of this chapter are divided into three sections as follows:

- Section-5.3.1: Effect of operating conditions and solid loading on local bubble hydrodynamics and particle velocity distribution in GLS-ST equipped with standard Rushton turbine (SRT).
- Section-5.3.2: Effect of Rushton turbine (RT)'s impeller diameter on gas phase hydrodynamics and power consumption in GL-ST
- Section-5.3.3: Investigation on the impact of high solidity pitched blade turbine (HSPBT)'s blade angle on gas phase hydrodynamics and power consumption in GL-ST.

Chapter-6: Summary on the major findings of this thesis and suggestions for future work are provided.

## Chapter 2

### Literature Review

Optimization and scale up of multiphase stirred tanks for industrial applications depend on the detailed description of interaction between the continuous phase and the dispersed phase. Spatial dispersion of gas phase governs the phase homogeneity, and the rate of heat and mass transfer in these tanks. Dispersion of gas phase is dictated by several key factors including operating conditions and impeller geometry. Therefore, a number of studies have been published on the effect of impeller type, impeller speed and gas superficial velocity. However, most of the available literature focusses on overall gas holdup and average bubble size and very limited data is available on local hydrodynamics. Understanding local hydrodynamics is important for successful optimization and scale-up of stirred tank as local mass transfer rates are dependent on it. This chapter presents a review of previous experimental and numerical studies on global and local bubble hydrodynamics of baffled and unbaffled stirred tanks. Measurement techniques for multiphase flows are also reviewed and compared for their suitability for measuring the local bubble hydrodynamics of stirred tanks.

#### 2.1. FLOW CHARACTERISTICS OF BAFFLED STIRRED TANKS

##### 2.1.1 Basic Definitions

In literature, the hydrodynamic behaviour of gas-liquid stirred tanks (GL-ST) is mostly described using the following dimensionless numbers:

##### **Flow Number**

Flow number (Fl) is the ratio of gas flow rate to the flow generated by impeller rotation and is defined by:

$$Fl = \frac{Q}{ND^3}$$

Here, Q is gas flow rate, N is impeller speed and D is impeller diameter

##### **Froude Number**

Froude number (Fr) is the ratio of acceleration due to impeller motion to the gravitational force and is defined by:

$$Fr = \frac{N^2 D}{g}$$

Here,  $g$  is acceleration due to gravity. For GL-ST fitted with SRT, ranges of  $Fr$  and  $Fr$  for different operating regime are determined using flow regime map (15, 34).

### Power Number

Power number ( $N_p$ ) is the ratio of pressure to the inertial forces of the dispersion and is defined as:

$$N_p = \frac{P}{\rho N^3 D^5}$$

Where  $\rho$  is the density of fluid;  $P$  is impeller power input into the liquid.

### 2.1.2 Operating regimes and power consumption

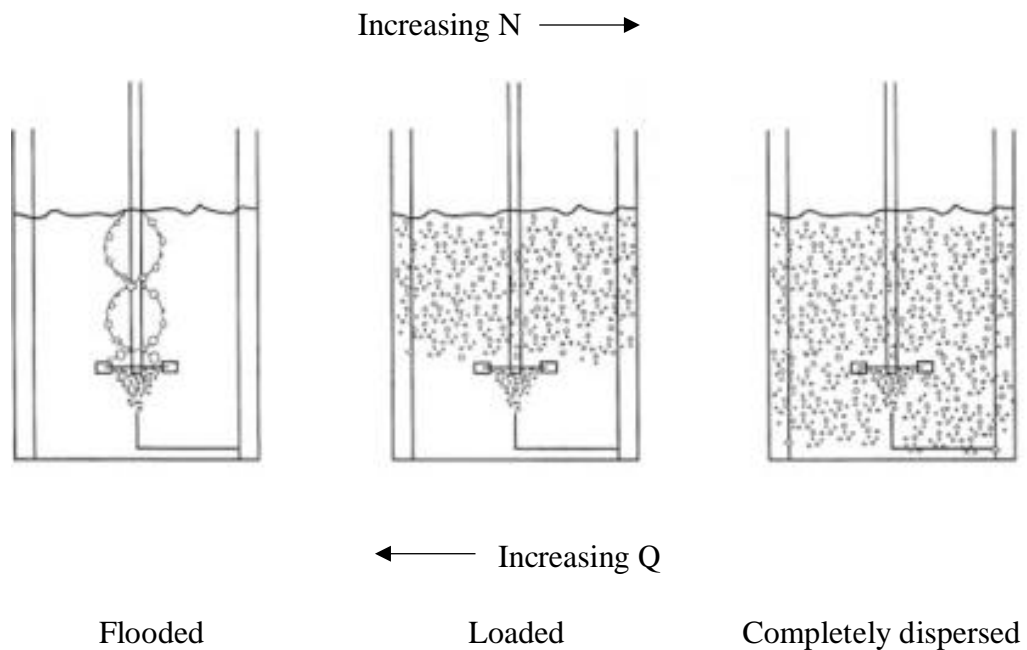


Figure-2.1: Schematic representation of flow patterns in GL-ST (15)

In stirred tanks operated at a fixed superficial gas velocity, different flow patterns ranging from flooding to a completely dispersed flow regime are exhibited when the impeller speed is increased from minimum to maximum (15, 34, 35) as shown in Figure-2.1. At low impeller speed, superficial velocity of gas dominates impeller propelling action leading to poor dispersion of gas bubbles. At this speed, most of the gas bubbles escape through blades leading to flooding of impeller and the stirred tanks

exhibit a behaviour similar to a bubble column. When the speed is increased, impeller starts discharging the gas bubbles radially outward; however below the impeller, no or minimal bubbles are observed. This is referred to as loaded operating regime. When impeller speed is increased further, impeller propelling action overcomes the gas velocity from sparger and the gas bubbles are found throughout the tank leading to a condition called completely dispersed regime. Figure-2.2 demonstrates general trend of the power curve in a GL-ST at constant superficial gas velocity (36).

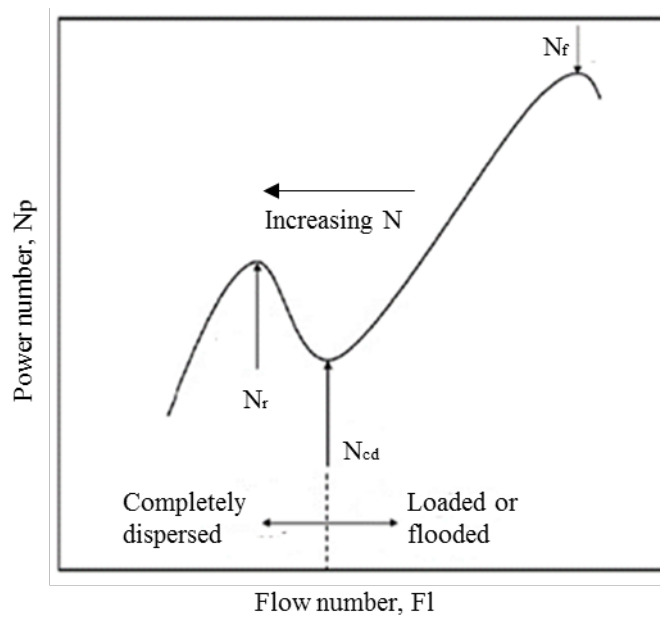


Figure-2.2: Plot for power number as a function of flow number at constant gas superficial velocity (36)

In this curve, the plot of power number ( $N_p$ ) vs gas flow number ( $Fl$ ) is used to identify the operating regime. In Figure-2.2,  $N_{cd}$  represents impeller speed at completely dispersed regime and the flow pattern of dispersed phase is similar as shown in Figure-2.1 (completely dispersed).  $N_f$  represents the flooded regime and  $N_r$  stands for the recirculation loop where two recirculation loops, one above and one below impeller can be observed (explained in the following section 2.1.2). The prediction of operating regime is of paramount importance in GL-ST and hence significant amount of work had been carried out by employing either visual observations or by power consumption measurements. Since majority of the prevailing industrial stirred tanks operates in a

dispersed flow regime, all experiments reported in this thesis are carried out only in completely dispersed regime.

### 2.1.3 Flow patterns

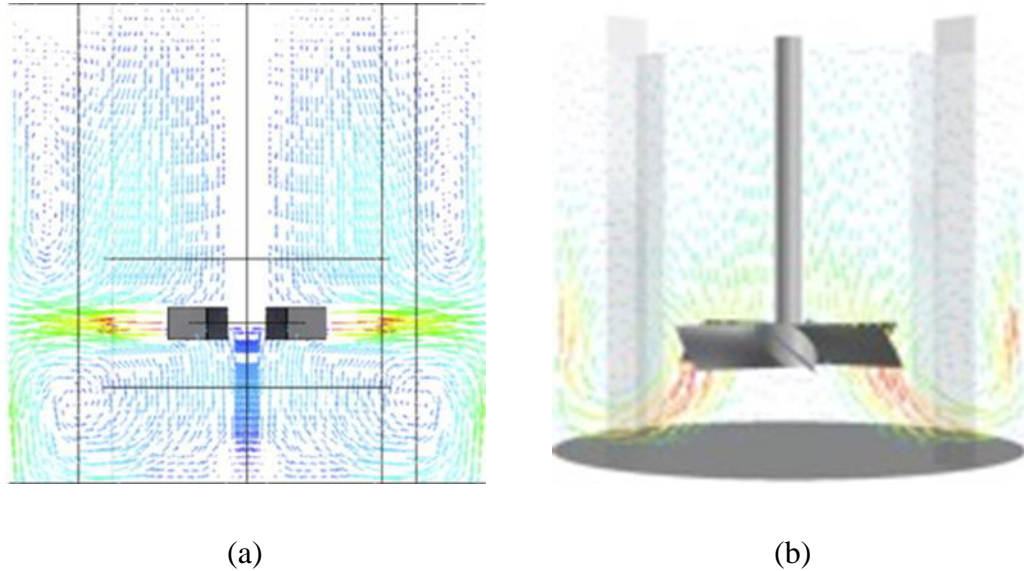


Figure-2.3: Flow patterns generated by (a) radial and (b) axial impeller (37, 38)

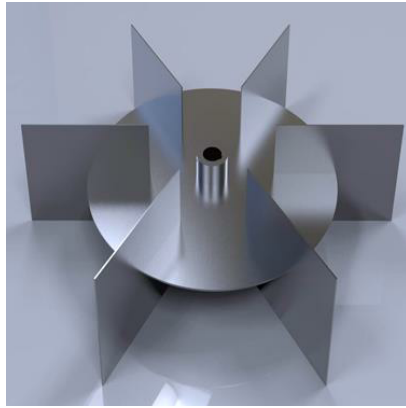
Spatial distribution of local bubble dynamics inside a stirred tank is predominantly dictated by the flow patterns generated by an impeller. Such flow patterns are dependent on the fluid discharge direction, which in turn relies on the impeller geometry. In baffled stirred tanks, the two most commonly observed flow patterns are: radial and axial as shown in Figure-2.3. The radial flow pattern is found in stirred tanks fitted with flat blade turbines such as SRT, disc turbines and paddles whereas axial flow pattern prevails in stirred tanks equipped with down or up pumping impellers. Radial flow pattern is advantageous for blending viscous solutions due to low pumping number whereas axial impellers are beneficial for solid suspension and gas dispersion applications. Figure-2.3(a) illustrates that for radial impellers, fluid is propelled out radially towards the tank wall. When fluid strikes the wall, it splits into two streams forming circulation loops. One stream circles axially upwards the impeller plane while the other one forms a circulation loop below impeller. The fluid velocity is strong in radial direction compared to bottom portion of tank and therefore, radial impellers are often not used in solid suspension applications. In case of axial impellers, based on direction of rotation, flow is discharged either axially downward (Figure-2.3b) or upward from the blade edge. For stirred tank fitted with axial impellers, apart from

impeller speed, the blade angle also determines the flow pattern and amount of power discharged into the fluid.

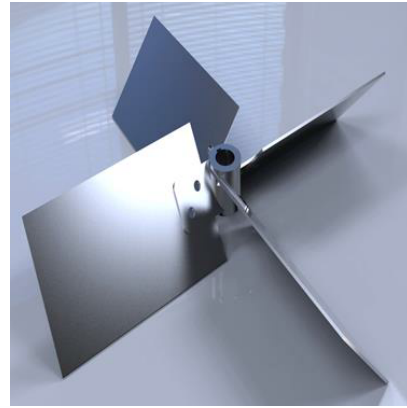
#### **2.1.4 Gas phase hydrodynamics**

The rate of mass transfer between phases in a stirred tank is determined based on the gas phase hydrodynamics which includes gas holdup and bubble size distribution (1). Overall gas holdup is defined as the ratio of volume occupied by gas phase to the total volume of fluid in GL-ST and to the total volume of solid and fluid in gas-liquid-solid stirred tank (GLS-ST). Impeller is one of the key factors that dictates gas holdup and bubble size in stirred tanks. The effectiveness of an impeller for gassing applications depends on blade geometry, blade angle, impeller speed, gas flowrate, and physical properties of the fluids involved. Figure-2.4 shows commonly used gas dispersion impellers for industrial applications. Conventionally, standard Rushton turbine (SRT) and pitched blade turbine (PBT) are used based on the desired flow pattern. Also, SRT has been mostly employed in academic research to investigate the gas phase hydrodynamics in lab scale experiments (Table-2.2). PBTs replaced SRTs for gas dispersion applications owing to few shortcomings of SRT which includes high power consumption and discharge of bubbles mostly at radial direction. While the power consumption by PBT ( $N_p = 2.7$ ) is almost half of the SRT ( $N_p = 4.5$ ), it suffers from high torque instabilities which causes fluctuation in the power dissipated to fluid resulting in improper mixing. In order to reduce torque instabilities, new impellers have been developed by modifying the solidity ratio of PBT (39, 40). For standard PBT, solidity ratio, defined as a ratio of total area of blade to swept area of impeller, varies from 0.25 to 0.4. If the solidity ratio lies below 0.25, then the impeller is known as low solidity pitched blade turbine (LSPBT) For high solidity pitched blade turbines (HSPBTs), solidity ratio is in the range of 0.60 to 0.9 depending on blade angle, curvature of the blades, and number of blades. The power number of LSPBT is lower in comparison to a standard PBT and HSPBT is mainly used for applications which demands less gas dispersion such as fermentation and bio-reactors. On the other hand, mineral processing applications such as cyanide destruction, bio-leaching of copper, and bio-oxidation of ferric iron, etc. demands an impeller to handle large volumes of gas and also to keep solids in suspension. Therefore, HSPBTs are used for such applications.





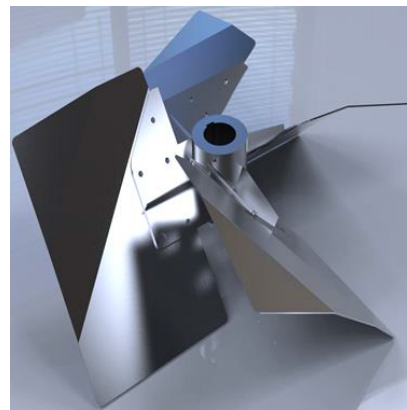
SRT



PBT



LSPBT



HSPBT

Figure-2.4: Gas dispersion impellers

Numerous researchers have investigated the gas phase hydrodynamics mostly in gas-liquid stirred tanks. Many studies are focused on the effect of impeller speed, power consumption, or superficial gas velocity on the overall gas holdup. Summary of experimental studies carried out so far in GL-ST to investigate gas holdup and local bubble hydrodynamics is listed in Table-2.1. It can be seen that majority of the studies have focused on overall gas holdup; and experiments have been conducted using either SRT or low solidity PBT. In addition, most of the previous studies have been conducted with PBT at a fixed blade angle of  $45^\circ$  and, modern impellers such as HSPBTs have not been investigated.

Table-2.1: Previous experimental studies on gas-liquid stirred tanks with measurements of gas phase hydrodynamics

<i>Author</i>	<i>Impeller</i>	$\theta$ ( $^{\circ}$ )	<i>N (rps)</i>	<i>T (m)</i>	<i>D/T</i>	$u_g (10^2 .m/s)$	<i>Measured parameters</i>	<i>Measurement technique (G - global; L - local)</i>
Hassan et al., (41)	6-BT, 6-BP, 4-BP	-	3.3-16.7; 3.3-13.3; 0.83-3.3	0.29	0.33-0.67	0.49-2.21	$\varepsilon$	Visual method (G)
Yung et al., (42)	6-BT, 4-BP	-	3.33-23.3	0.4	0.225-0.45	0.971-2.16	$\varepsilon$	Inclined manometer (G)
Montante et al.,(14)	SRT	-	3.3–7.5	0.24	0.33	0.26	BSD	Digital image processing (L)
Lu et al., (43)	SRT	-	6.67-10	0.29	0.33	0.13-0.52	$\varepsilon$	Hot-film anemometry (L)
Wang et al., (44)	SRT	-	1.3-4.9	0.38	0.33	0.20-0.66	$\varepsilon$	Fibre optic probe (L)
Alves et al., (16)	SRT	-	5-7.5	0.29	0.33	0.25-0.50	BSD	Capillary suction method (L)
Sun et al., (45)	SRT	-	3.37-7.76	0.38	0.33-0.5		$\varepsilon$	Conductance probe (L)

Table-2.1 (continued)

<i>Author</i>	<i>Impeller</i>	$\theta$ ( $^{\circ}$ )	$N$ (rps)	$T$ (m)	$D/T$	$u_g$ ( $10^2$ .m/s)	<i>Measured parameters</i>	<i>Measurement technique</i> (G - global; L - local)
Laakkonen et al., (17)	FBT	-	6.66-8.33	0.26	0.33	0.07	$\varepsilon$ and BSD	PIV (G)
Khokpar et al., (11)	SRT	-	3.33	0.2	0.33	0.13-0.27	$\varepsilon$	CARPT (G)
Bombac et al., (46)	SRT	-	4.43-6.67	0.45	0.33	0.17	$\varepsilon$	Resistive probe (L)
Ford et al., (4)	SRT	-	3.33-11.66	0.21	0.36	0.43	$\varepsilon$	X-ray CT (G)
Machon et al., (47)	SRT	-	12.83	0.15	0.33	0.28	BSD	Stereo microscope (G)
Mueller et al., (48)	SRT	-	8.33-12.5	0.2	0.33	1.50	$\varepsilon$	Optical probe (L)
Hampel et al., (49)	SRT	-	13.3-20	0.08	0.44	0.0018	$\varepsilon$	Gamma ray CT (G)
Moucha et al., (50)	SRT, PBT-6	45 $^{\circ}$	4.16-14.16	0.29	0.33	0.0021-0.0084	$\varepsilon$	Visual inspection (G)

Table-2.1 (continued)

<i>Author</i>	<i>Impeller</i>	$\theta$ ( $^{\circ}$ )	$N$ (rps)	$T$ (m)	$D/T$	$u_g$ ( $10^2$ .m/s)	<i>Measured parameters</i>	<i>Measurement technique</i> (G - global; L - local)
Lee et al., (15)	SRT	-	2.1-13.83	0.2	0.33	1.50	$\varepsilon$	Optical probe (L)
Rewatkar et al., (51)	PBT- 6	45 $^{\circ}$	0.4-10.5	0.57	0.33	0.0015-0.03	$\varepsilon$	Visual inspection (G)
Yawalkar et al., (9)	SRT, PBT-6	45 $^{\circ}$	0.4-10.5	0.57	0.33	0.07	$\varepsilon$	Visual inspection (G)
Boden et al., (52)	SRT	-	16.6-20	0.08	0.44	0.0018	$\varepsilon$	X-ray cone beam CT (G)
Bouaifi et al., (53)	SRT, PBT-6, A 310	45 $^{\circ}$	1.66- 11.67	0.43	0.33-0.44	0.018	$\varepsilon$ and BSD	Visual inspection and photographic method (G)
Hristov et al., (54)	SRT	-	16.6-20	0.08	0.44	0.0018	$\varepsilon$	X-ray cone beam CT (G)
Kong et al., (55)	SRT	-	5.83-13.33	0.2	0.33	1.50	$\varepsilon$	Gamma ray CT (G)
Yang et al., (22)	PBT- 6	45 $^{\circ}$	7.5	0.38	0.33	0.22	$\varepsilon$	Sampling tubes (L)

Table-2.1 (continued)

<i>Author</i>	<i>Impeller</i>	$\theta$ ( $^{\circ}$ )	$N$ (rps)	$T$ (m)	$D/T$	$u_g$ ( $10^2$ .m/s)	<i>Measured parameters</i>	<i>Measurement technique (G - global; L - local)</i>
Thatte et al., (56)	SRT, PBT-6	45 $^{\circ}$	1.67-6.67	0.57	0.33	0.01	$\varepsilon$	Gamma ray attenuation technique (G)
Laakkonen et al., (57)	SRT	-	2.58-4.16	0.63	0.33	0.07	BSD	Capillary suction probe (L)
Saravanan et al., (58)	SRT, PBT-6	45 $^{\circ}$	0.30-15.45	0.57	0.33	0.0015-0.03	$\varepsilon$	Visual inspection (G)
Montante et al., (59)	SRT, PBT-U, A 310	45 $^{\circ}$ , 30 $^{\circ}$ , 60 $^{\circ}$	1.66-8.33	0.23	0.33	0.07	$\varepsilon$	ERT (G)
Lee et al., (60)	SRT, half circular blade disk	-	2.1-13.83	0.2	0.33	1.50	$\varepsilon$	Optical probe (L)

Table-2.1 (continued)

<i>Author</i>	<i>Impeller</i>	$\theta$ ( $^{\circ}$ )	$N$ (rps)	$T$ (m)	$D/T$	$u_g$ ( $10^2$ .m/s)	<i>Measured parameters</i>	<i>Measurement technique</i> ( <i>G</i> - global; <i>L</i> - local)
Bao et al., (26)	PDT+2CBY	22 $^{\circ}$ (at the tip)	8-10	0.48	0.4	2.34	$\varepsilon$	Visual inspection (G)
<p><i>Impeller:</i> A310 - axial impeller type ; BT - Blade turbine; BP - Blade paddle; 2CBY - axial impeller type ; SRT - Standard Rushton turbine; FBT - Flat blade turbine; PBT - Pitched blade turbine</p> <p><i>Measured parameter:</i> <math>\varepsilon</math> - gas holdup; BSD - bubble size distribution</p> <p><i>Measurement technique:</i> CT – computed tomography ; PIV – particle image velocimetry ; ERT- Electrical resistance tomography; CARPT – Computer aided radioactive particle tracking</p>								

Based on experiments, several empirical correlations have been proposed to predict overall gas holdup as shown in Table 2.2. However, these empirical correlations fail to provide an extensive information on the local bubble dynamics that is essential for design and scale up of stirred tanks. Consequently, researchers have explored local hydrodynamics in GL-STs with a focus on the measurements of liquid phase in presence of gas bubbles (10, 61, 62). The next section summarizes previous work on measurement of local bubble hydrodynamics.

Table-2.2: Empirical correlations to predict gas holdup

<i>Reference</i>	<i>Correlation</i>
Lee et al., (5)	$\epsilon_g = 4.2 \left( \frac{N}{N_{cd}} \right)^{1.33} vvm^{1.3}$
Greaves et al., (6)	$\epsilon_g = 4.07 N^{0.62} Q^{0.64} \left( \frac{D}{T} \right)^{1.39}$
	$\epsilon_g = 4.2 N^{0.79} Q^{0.54} \left( \frac{D}{T} \right)^{1.92}$
Smith, (7)	$\epsilon_g = 85 (\text{ReFrFl})^{0.35} \left( \frac{D}{T} \right)^{1.25}$
Hassan et al., (63)	$\epsilon_g = 0.209 \left( \frac{QN}{\sigma} \right)^{0.44}$
Rewatkar et al., (8)	$\epsilon_g = 3.54 \text{Fl}^{0.43} \text{Fr}^{0.51} \left( \frac{D}{T} \right)^{2.08}$
Yawalkar et al., (9)	$\epsilon_g = 0.122 \left( \frac{N}{N_{cd}} \right)^{0.64} vvm^{0.69} T^{0.32} \left( \frac{D}{T} \right)^{0.14}$

### 2.1.5 Local bubble hydrodynamics

#### Experimental studies

Several studies have reported bubble size distribution (BSD) in stirred tanks using experimental measurements. Kawecki et al., (64) were the first to provide BSD in

stirred tank fitted with SRT. A small square column was attached to stirred tank at the impeller plane. Most of the bubbles discharged radially from Rushton turbine was expected to travel towards the tank wall where the square section was connected. Bubbles trapped in the square section were photographed and their sizes were measured using the developed negatives from photo film. This method suffered from various drawbacks including disturbing the flow pattern by drawing liquid at impeller plane, increase in bubble velocity and size when it rises in square section.

Later, Barigou et al., (65) provided detailed measurements on BSD. They used capillary suction probe to measure bubble sizes in a 1.0 m diameter tank fitted with SRT. Measurements were taken at 50 positions across the tank for a range of gas superficial velocity and impeller speed. In addition, effect of electrolyte addition on spatial BSD was also investigated. It was reported that increasing impeller speed led to reduction in bubble size whereas increasing superficial gas velocity and electrolyte had an opposite effect. High gas flowrates and salt solution enhanced bubble coalescence resulting in increase in bubble size. They have also pointed out that reproducibility of the results using capillary technique was good with variations limited to 6%. However, due to the size of probe (0.39 mm I.D) finer bubbles could not be captured and also flow conditions were significantly affected due to its intrusive nature.

From the above studies it can be seen that BSD is also governed by bubble break up and coalescence effects apart from operating conditions. Thus, a better understanding of either break up or coalescence phenomena can aid in the estimating the spatial distribution and in turn mass transfer rate. Therefore, Parthasarathy et al., (66) investigated BSD in a non-coalescing 0.15 m stirred tank with SRT to study the bubble break up process. Methyl-isobutyl-carbinol solution was added to water to maintain the non-coalescing condition. Two set of controlled bubble size experiments were performed in which they injected either 300  $\mu\text{m}$  or 2.5 mm diameter bubbles through spargers. Gas superficial velocity was kept minimal at  $2.5 \cdot 10^{-4}$  such that gas flow rate does not alter the bubble size. Bubbles were drawn out from the tank and photographed as explained earlier to measure bubble size. It was observed that 300  $\mu\text{m}$  was already small enough to undergo bubble break up and thus the bubble size distribution was maintained. In case of 2.5 mm bubbles changed from unimodal to bimodal distribution



and again back to unimodal distribution towards the smaller bubble size with increase in impeller speed.

Schafer et al., (28) examined the effect of impeller geometry and flow patterns on BSD in GL-ST equipped with SRT and PBT using phase Doppler anemometry (PDA). It was observed that the flow pattern generated by radial (SRT) and axial (PBT) impeller had a significant effect on the size distribution. The average bubble diameter varied between 0.65 mm to 1.5 mm near impeller region. The study has also reported that larger bubbles were often encountered at impeller vicinity. It was observed that apart from impeller shear, bubbles entering impeller region through recirculation loops coalesce with bubbles emerging out of sparger that caused larger bubbles near impeller blades.

Spatially averaged local bubble size in GL-ST fitted with dual turbines was investigated by Alves et al., (16). They adopted the same measurement technique used by Barigou et al., (65). Detailed experiments were conducted by varying impeller type, number of impellers, liquid phase and diameter of the tank. It was observed that bubble size was smaller near the impeller and increased towards tank wall. The bubble sizes measured near tank wall represented the average bubble size found across the tank. Bubble size decreased when tap water was replaced with electrolyte or surfactant solution. Efforts to compare the experimental data with existing literature failed due to significant differences in measurement technique and post processing methods (with variation in average bubble size up to 35%) reported by previous researchers. Therefore, Laakkonen et al., (57) measured local BSD in 14 dm<sup>3</sup> stirred tank with SRT using three different measurement techniques. They employed capillary suction probe, PDA, and digital imaging to measure bubble size and to critically analyse the shortcomings of each technique. It was observed that all three techniques resulted in different results mainly due to limitations on the detectable bubble size for each technique. Capillary suction was unable to trap bubbles below 0.39 mm whereas bubble sizes above 1.4 mm could not be resolved by PDA post processing. Very fine bubbles, less than 0.1 mm, could not be accurately captured using digital imaging technique. In addition to this, the intrusive effects of capillary probe and optical errors from digital imaging and PDA techniques were pointed out in the study.

Laakkonen et al., (17) investigated gas holdup and BSD using particle image velocimetry (PIV) in the same 14 dm<sup>3</sup> tank. Air-water and CO<sub>2</sub> – butanol solutions

were used as gas and liquid phase in the experiments. The study founded that PIV technique generated more consistent experimental data which could be used to validate simulations and was free from any optical and intrusive errors compared to previous techniques. Following this, Montante et al., (14) investigated BSD in 0.24 m diameter GL-ST using PIV technique and image processing method. Turbulence properties and phase velocities were obtained using PIV method and bubble size was calculated using imaging technique based on thresholding method. The main motive behind carrying out the experiment was to provide reliable data for CFD simulations. However, gas holdup was limited to 1% which was much lower compared to lab scale and industrial scale stirred tanks.

The BSD data reported by the earlier studies suffered from serious measurement errors or was limited to low gas holdup conditions. Recently needle probes have been employed by researchers to overcome these limitations. Bao et al., (26, 67) have reported the influence of impeller diameter, operating conditions and temperature of the gas sparged on local gas holdup and BSD using conductivity probe measurements. A multi-impeller assembly was employed in the study, where the shaft was mounted with a parabolic blade disc turbine at bottom and two hydrofoils on top. It was observed that overall bubble diameter increased by 21% when the temperature of sparged gas was increased from ambient temperature (24 °C) to 81 °C. Moreover, they observed that in multi-impeller assembly system increasing impeller diameter did not impact axial BSD. However, in both studies, measurements were taken at various axial locations by placing the probe tip facing inwards at 35 mm from tank wall. Such probe orientation can impart significant errors in stirred tank measurements where the flow is not always unidirectional (48). The reported data was further limited to minimum bubble size of 3 mm due to size of the probe tip. Recently, Lee et al., (15) reported time averaged local gas holdup in GL-ST fitted with SRT. The potential of a single tip optical probe to successfully measure bubble frequency, local gas holdup and to identify flow regime has been reported in this study. However, no information on BSD and bubble velocity was presented.

Experimental data on local bubble hydrodynamics discussed so far clearly indicates that there is a wide variation in BSD results reported by researches due to limitations in measurement techniques. Data using needle probes were also limited to information on time averaged gas holdup and bubble size. In addition, errors imposed on the data

due to probe orientation was not quantified so as to generate a reliable experimental data set for CFD validation.

### **Numerical studies**

In addition to experimental studies in last two decades, researchers have carried out detailed CFD simulations and developed multi-phase models to predict bubble size and local gas holdup. Alves et al., (68) employed a simple compartmental modelling approach to predict spatial distribution of gas holdup and average bubble size. In their study, slip velocity was optimized to predict the bubble size close to experimental data. The study assumed bubbles to be spherical and of the same size. Average bubble size measured near impeller blades from experiments was used as an input for the simulations. A simple lumped parameter, which accounts for combined effects of bubble breakup and coalescence, was considered to characterize dispersed bubbles. However, it was anticipated that near impeller regions bubble break up was frequent and in the rest of the tank coalescence dominates bubble break up. Significant disagreement between simulation results and experimental data was observed due to the parameter lumping and uniform bubble size inputs. Especially, simulations failed to capture the smaller bubble sizes with small slip velocities away from impeller as the model was unable to distinguish between smaller and larger bubbles.

Laakkonen et al., (69) used a multi-block approach coupled with discretized population balance to characterize bubble break up and coalescence in a 194 dm<sup>3</sup> GL-ST fitted with SRT. In this approach, the tank was sub divided into 23 ideally mixed blocks and local BSD for each block was accounted. Parameters such as flow velocities, turbulent energy, and slip velocities that affected bubble break up, and coalescence that includes were simulated using single-phase simulations. It was hypothesized that effect of gas phase on the liquid phase was relatively small, and hence single phase simulations were adequate. Simulation results showed good agreement with experimental data at few operating conditions, but deviated for most other. They emphasized the need of accurate experimental data to further improve the CFD models to predict BSDs. Kerdouss et al., (70) carried out CFD simulations using Eulerian- Eulerian approach with dispersed k- $\epsilon$  turbulent model to predict spatial distribution of average bubble size and gas holdup in GL-ST fitted with dual turbine. Both bubble break up, and coalescence were accounted for using a bubble number density equation. They used experimental data of Alves et al., (68) to validate the

simulations. They proposed to use values of 0.3 for drag coefficient correlation; 0.075 for bubble break up and 0.05 for coalescence to predict the spatial distribution of gas phase close to experimental data.

It can be seen from the above mentioned CFD studies that it is critical to adjust the bubble break up and coalescence parameters to predict BSDs. Therefore, Laakkonen et al., (71) incorporated those parameters in a multi-block model using their experimental data. The parameters were adjusted for each operating condition using measured BSDs. Consequently, authors have reported that their model predicted BSD closer to experimental data compared to previous studies. This study suggested that CFD model to predict local bubble hydrodynamics need to be validated for every operating conditions and impeller geometry. Also Laakkonen et al., (71) emphasized that more experiments with dense gas flow rates and various impeller typed need to be carried out for CFD validation studies.

Numerical studies discussed so far simulated the spatial distribution of gas phase using Euler-Euler approach in which the BSD was obtained by solving population balance equations. However, to understand interaction between bubble to bubble, bubble to liquid, and bubble to wall Euler-Lagrange (EL) approach was found to be useful (72, 73). EL approach was adopted by Sungkorn et al., (72) to investigate the effect of superficial gas velocity on BSD in a 0.23 m stirred tank under dilute flow conditions. Preliminary simulations were carried out in a less turbulent bubble column and the results were validated using experimental data (74). Sungkorn et al., (72) observed that EL simulations results were in good match with experimental results at major section of the column but simulations under predicted BSD near sparger. They have reported that the difference in results near air inlet was due to lack of accuracy in experimental results.

Most of the numerical studies carried out earlier simulated lab scale stirred tank with low gas holdups. Recently, Nauha et al., (75) have simulated gas phase hydrodynamics in an industrial scale stirred tank bioreactor (100 m<sup>3</sup> working volume) with high gas holdups using method proposed by Laakkonen et al., (71). In addition, local conditions accounted for each compartment was compared with ideal mixing conditions to conclude that ideal mixing models failed to predict spatial distribution of gas phase at industrial scale tanks. Authors have also reported that due to inadequate experimental data at this scale, simulation results could not be verified.

## **Effect of solid loading on gas phase hydrodynamics**

Literature review discussed so far was mainly focused on the investigation of gas phase hydrodynamics in two phase GL-STs. Many applications of stirred tanks, e.g. in the mining industry, include solid phase. There in addition to gas dispersion the tank has also to suspend solids. Addition of solids in a GLS-ST significantly alters the gas phase hydrodynamics and flow pattern. So it is inevitable to examine the effect of solid loading on stirred tank hydrodynamics. However, only very few researchers have carried out experiments and simulations to understand hydrodynamics in GLS-STs (19, 22, 76-81) but mostly focused on measurement of power consumption, and analysis of liquid phase velocities. Murthy et al., and Conway et al., (79, 80) reported only global gas holdup measured by visual observations and did not provide any information on spatial distribution of gas phase in the stirred tank. Recently, Yang et al., (22) studied gas, and solid holdup distribution in a 0.38 m diameter GLS-ST using sample withdrawal method. The effect of operating conditions on solid suspension, time averaged gas holdup, and bubble size was reported. 6 mm I.D. sampling tube was used to measure gas phase by withdrawing the fluid at different radial and axial locations in the tank. For gas holdup predictions, better agreement between experiments and simulations were obtained by modifying drag force correlation. However, bubble size distribution or velocity was not measured. The sampling withdrawal method suffered from intrusive effects; while bubbles larger than 6 mm could not be captured due to limitation on the sampling tube I.D.

To summarize, available experimental and simulation data on gas phase hydrodynamics have improved the understanding of overall gas holdup in GL-STs fitted with SRT. However, systematic experimental data on spatial distribution of gas holdup and BSD have not been widely reported mostly owing to limitations on the measurement techniques. In addition, local bubble hydrodynamics on large sized tanks and for impellers used in industries are not available that further limits validation of CFD models for industrial applications. Also the effect of solid phase on local bubble hydrodynamics has not been reported so far.

## **2.2 UNBAFFLED STIRRED TANKS**

Baffled tanks are conventionally preferred for mixing applications as the presence of baffles disrupts liquid flow pattern, and promotes axial circulation resulting in a more

efficient mixing process. While unbaffled tanks are often seen as undesirable for standard mixing applications, there is increasing importance being placed on them in certain specialty fields. They are particularly beneficial for shear sensitive (bioreactors), low attrition (crystallizer), and deep-cleaning/sterilization (pharmaceutical) applications (82). In unbaffled stirred tanks, centrifugal forces increase the angular velocity of liquid, leading to a greater deformation of free liquid surface and generation of a vortex (Figure-2.5a). As impeller speed increases, both width and depth of vortex increases (82-84). At high impeller speeds, vortex comes in contact with impeller, leading to gas dispersion (Figure-2.5b). The gas dispersion governs the centrifugal flow field and alters the vortex shape. Moreover, The vortex shape dictates interface area between phases, and overall hydrodynamics.

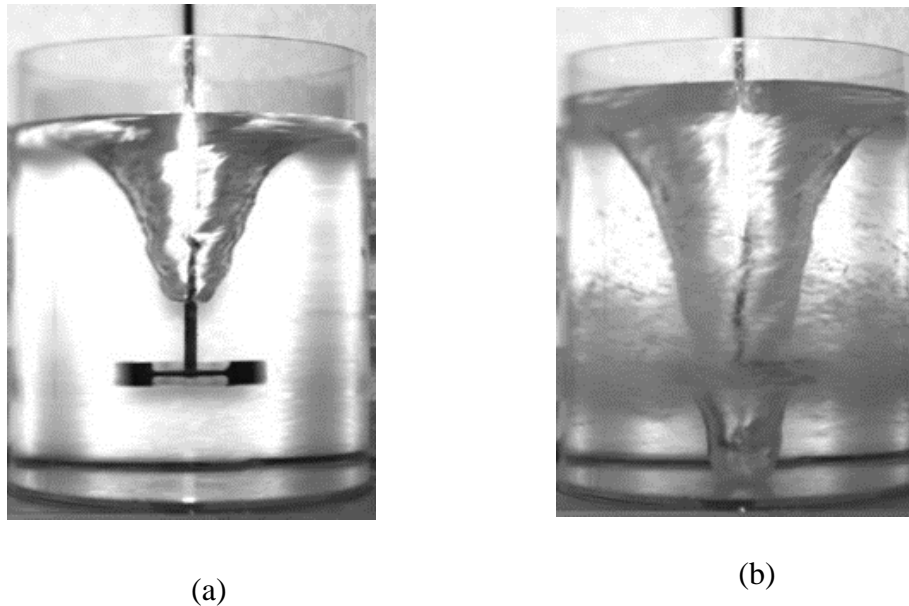


Figure-2.5 vortex shape (a) without vortex ingestion and (b) with vortex ingestion

Previous experimental and modelling studies on vortex shape and hydrodynamics of unbaffled stirred tank are listed in Table-2.3. These studies could be grouped in three different categories, namely, analytical models, CFD models, and experimental investigations. Nagata et al., (85) proposed an analytical model derived from experimental measurements on the effect of impeller speed, impeller clearance, and liquid loading on vortex shape. Although this model was able to predict the vortex shape above impeller, there were significant discrepancies observed with vortex ingestion (82). Busciglio et al., (82) introduced a velocity correction factor in Nagata et al model which could predict vortex shape with vortex ingestion. However, scaling

factors, and fluid viscosity were not accounted for in the model. Recently, Deshpande et al., (86) proposed a model to calculate only the vortex depth, without vortex ingestion by accounting for tank diameter, impeller diameter, and fluid viscosity. All these models were derived using imaging experiments which were limited to application in transparent columns. In addition, Busciglio's model (82) needs further investigation on gas holdup, and bubble size distribution to understand hydrodynamics associated with the vortex ingestion.

Most of the CFD models developed for unbaffled stirred tank have used Eulerian-Eulerian (EE) model coupled with volume of fluid (VOF) approach (86-90) to track the gas-liquid interface and to analyse hydrodynamics without vortex ingestion. High turbulence, rotational flow field, and variation of flow behaviour from highly turbulent to laminar nature from impeller blades to wall inside an unbaffled stirred tank make the prediction of vortex shape complex (88). Therefore, the effect of different turbulence models on vortex shape prediction was investigated by Mahmud et al., (87). It was found that simulations with Reynolds stress model (RSM), and shear stress turbulent (SST) models predicted axial, and tangential velocities that were more consistent with experimental data compared to that from the k- $\epsilon$ , and k- $\omega$  models.

Several experimental techniques were employed to characterise gas-liquid hydrodynamics in unbaffled stirred tanks. Tomography techniques were used to analyse the effect of impeller speed on gas holdup (49, 52, 54). These studies were conducted using small tank (0.08 m diameter) and primarily focused on improving the image reconstruction algorithms to measure the gas phase distribution. Owing to low spatial resolution ( $> 1$  cm) of tomography techniques, they failed to provide measurements of local bubble properties, or identify a third phase in the flow domain (91). Wang et al., (92) used a vision probe to investigate bubble size and particle size distribution in a three phase unbaffled tank which captured sharp images but resulted in high invasive errors due to its size. To summarize, it is evident that most of the studies on unbaffled tanks were focused on predicting vortex shape without gas dispersion. Recently Busciglio et al., (82) have provided data on shape with vortex ingestion. Nevertheless, data on vortex shape, and gas and liquid phase hydrodynamics with vortex ingestion are critical to design a self-ingesting unbaffled reactor.

Table-2.3: Previous experimental \* and CFD # studies on gas-liquid unbaffled tank

<i>Author</i>	<i>T (m)</i>	<i>Impeller type</i>	<i>N (rpm)</i>	<i>Clearance</i>	<i>Measurement technique</i>	<i>Parameter investigated</i>
Nagata et al., (85)	0.19	SRT	100 - 400	T/3	*High speed imaging	Vortex shape above impeller
Busciglio et al., (83)	0.19 0.48	SRT; PBTD; A310	100 - 1000	T/6 – T/2		
Galletti et al., (93)	0.29	SRT	200 - 300	T/3		
Galletti et al., (94)	0.29	SRT	200 - 300	T/3		
Busciglio et al., (82)	0.19	SRT; PBTD; A310	100 - 1000	T/6 – T/2		Vortex shape with air ingestion
Mahmus et al., (87)	0.15	Magnetic stirrer	150 - 400	N/A	*LDV #VOF-RST	Vortex depth above impeller
Rieger et al., (95)	0.15 0.64	SRT; FBT; PBT;Anchor agitator	100 - 400	T/3 T/9	*Visual observation	
Assirelli et al., (96)	0.29	SRT	525	T/4		
Wang et al., (92)	0.28	FBT	400	T/3	*Vision probe	Bubble size
Hampel et al., (49)	0.08	SRT	1000 - 1200	T/3	* $\gamma$ -T	Gas holdup
Hristov et al., (54)					*X-CT	
Boden et al., (52)					*CBCT	



Table-2.3 (Continued)

<i>Author</i>	<i>T (m)</i>	<i>Impeller type</i>	<i>N (rpm)</i>	<i>Clearance</i>	<i>Measurement technique</i>	<i>Parameter investigated</i>
Deshpande et al., (86)	0.45	SRT	39 – 306	T/3	*Laser pointer #VOF	Vortex depth above impeller;
Glover et al., (97)	0.29	Paddle agitator	72	T/3	VOF-SST	velocity
Haque et al., (88)	0.15	SRT	200	T/3	*LDV #VOF-RST	distribution and turbulence parameters
Montante et al., (98)	0.24	SRT	400	T/2	*PIV #RANS-RSM	Velocity distribution and
Lamarque et al., (99)	0.15	Magnetic stirrer	400	N/A	#LES *LDV	turbulence parameters
Gimbun et al., (100)	0.29	SRT	190	T/3	#DES, LES	

$\gamma$ -T -  $\gamma$ -ray tomography; X-CT – X-ray computed tomography; CBCT – Cone beam computed tomography; LDV – Laser doppler velocimetry; PIV – Particle image velocimetry; SRT – Standard Rushton turbine; PBTD – Pitched blade turbine down-pumping; PBTU - Pitched blade turbine up-pumping FBT – Flat blade turbine; VOF – Volume of Fluid; RSM – Reynolds stress model; SST – Shear stress turbulence; LES – Large eddy simulations; DES – Detached eddy simulations

### **2.3 SELECTION OF MULTIPHASE FLOW MEASUREMENT TECHNIQUE**

In order to measure bubble dynamics and particle velocities in stirred tanks, researchers have employed both non-intrusive (4, 9, 11, 22, 41, 42, 47, 49, 50, 52, 53, 58, 59) and intrusive (14, 15, 45, 46, 60, 69) techniques. To investigate liquid or solid phase velocity, particle tracking techniques such as particle image velocimetry, radioactive particle tracking, and positron emission particle tracking were used. For global gas holdup and bubble size measurements, high speed imaging and various tomography techniques were employed. Most of the abovementioned techniques were either limited to dilute flow conditions or to transparent columns. Furthermore, these techniques suffer from either spatial, or temporal resolution. In GLS-ST, due to high gas dispersion and turbulent nature of the flow, typically bubbles and particles of less than 1 mm are found which limits the application of non-invasive techniques for bubble or particle size distribution studies. Also, non-intrusive techniques are expensive and could not be readily deployed in industrial scale due to constraints on space required for data processing unit, radiation hazards, and transparent columns. Nevertheless, to improve the performance of GLS-ST and to develop a reliable computational fluid dynamics (CFD) model, it is essential to understand local bubble hydrodynamics. For instance, bubble size and velocity distribution are key parameters to evaluate the drag forces on bubbles and for bubble population balance in a CFD model. In order to study complex local hydrodynamics in a multiphase system, a simple and cost effective flow measurement technique should be used which can also be employed in a three phase system. Optical probes fulfil all these criteria. They are cheap to manufacture, robust, and can operate at elevated temperature and pressures. The post processing of data obtained from optical probes is also straightforward. They can be used to accurately detect the gas-liquid interface with low interference to the flow field. Hence, in this work an optical probes have been used to measure simultaneously local bubble dynamics, and particle velocities.

### **2.4 SUMMARY**

In this chapter, hydrodynamics of baffled and unbaffled stirred tanks, such as operating regimes, global and local bubble hydrodynamics, and measurement techniques is discussed. Exhaustive experimental and numerical investigations have been carried out for stirred tanks to understand the influence of operating conditions and impeller geometry on overall gas phase hydrodynamics. Yet, there is a significant knowledge

gap on local bubble hydrodynamics that governs mass transfer rate, and design and scale up of multiphase stirred tanks. It is also evident from the literature review that most of the reported studies are carried out in gas-liquid stirred tanks and focused on lab scale experiments with tank diameter less than 0.25 m. Information on the effect of solid loading on local bubble hydrodynamics is not available in open literature. Moreover, vital data on the impellers used in industries for gas dispersion applications such as HSPBT are not reported. There is also a lack of understanding on vortex shape that dictates local bubble hydrodynamics in unbaffled stirred tanks. As stated by many researchers the lack of reliable measurement technique limits the measurement of local bubble hydrodynamics in three phase stirred tanks. The next chapter investigates the potential of optical probes to measure local bubble hydrodynamics and particle velocities.

## **Chapter 3**

# **Simultaneous measurements of local bubble dynamics and particle velocities using optical probe**

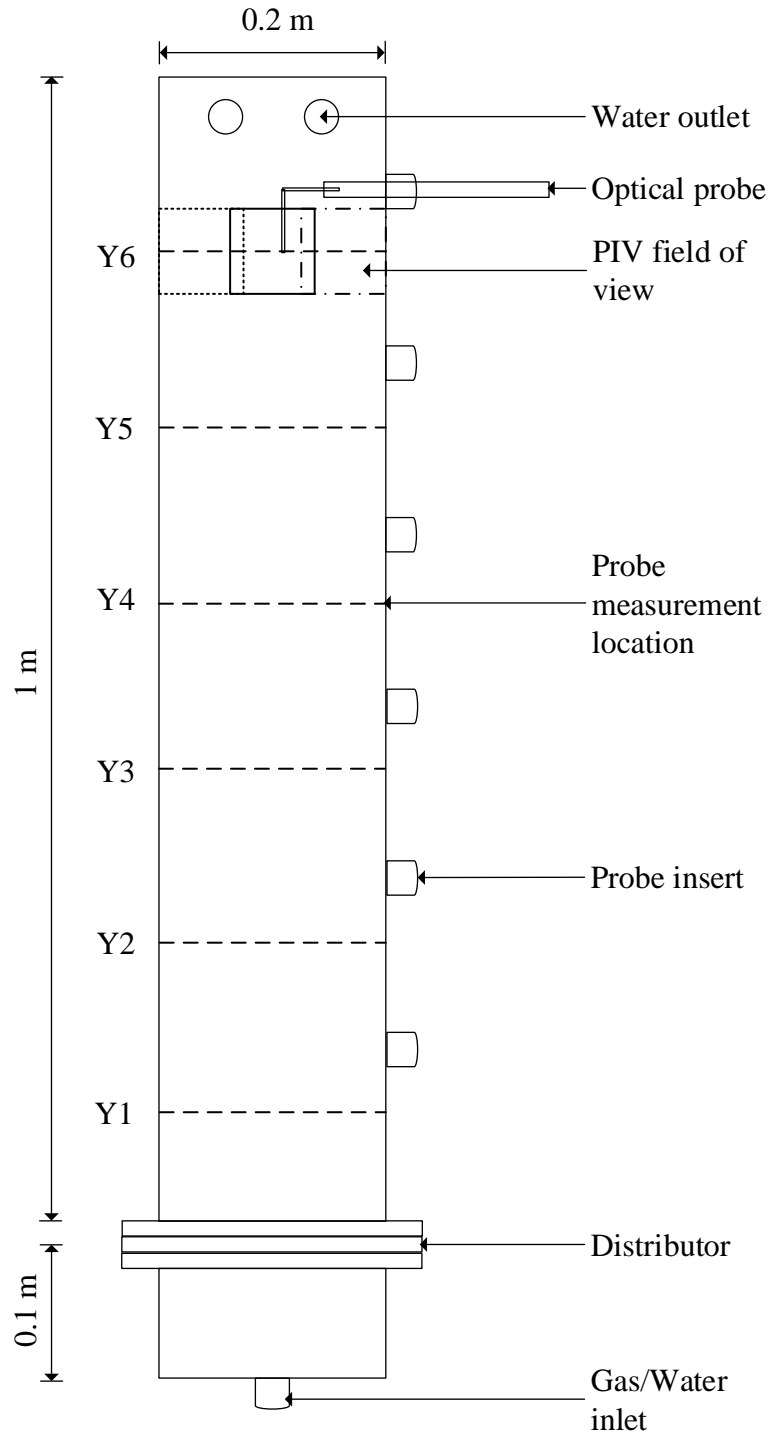
### **3.1 INTRODUCTION**

As discussed in Chapter 2, optical probes have been extensively used to study hydrodynamics in gas-liquid systems. The potential of these probes to accurately detect the gas-liquid interface and measure local bubble hydrodynamics were demonstrated by carrying out experiments in both cold flow studies and at elevated temperature and pressure conditions. Recently, researchers (118, 119) have used optical probes to measure bubble dynamics in slurry bubble columns and airlift bioreactors. Nevertheless, most of the work reported to date indicates that optical probes were capable of measuring gas phase in a multiphase system. To study the complex hydrodynamics in a multiphase system, a simple and cost effective flow measurement technique should be employed which can simultaneously measure data on all three phases (gas, liquid and solid) in a multiphase system. Recent developments in optical probe technology have made it possible to use a single probe for simultaneous measurement of local bubble hydrodynamics as well as particle velocities. In this chapter, first the data acquisition and analysis is described in detail using optical probes. The particle velocity and bubble chord length data obtained from optical probes is then validated using PIV and high speed imaging. Finally simultaneous measurements of both gas and liquid/solid phase properties is demonstrated using a slurry bubble column.

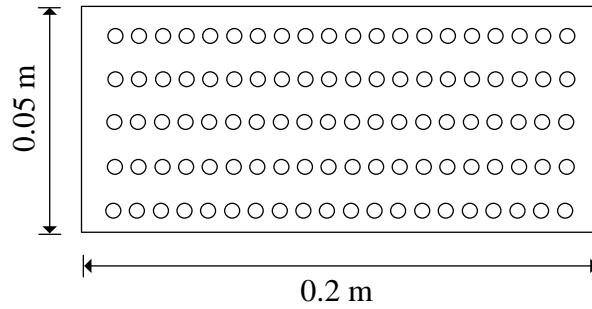
### **3.2 EXPERIMENTAL SETUP**

To enable unencumbered videography measurements a pseudo two dimensional rectangular column was used for the validation experiments. The schematic diagram of the experimented pseudo rectangular column with dimensions, and optical probe measurement locations is shown in Figure-3.1(a). Experiments were carried out in a 1.1 m tall rectangular acrylic column with an inside length and width of 0.2 m and 0.05 m respectively. Four set of experiments were performed in this study: (i) Liquid recirculation, (ii) Gas-Liquid bubble column (GL), (iii) Gas-Liquid-Solid (GLS) slurry

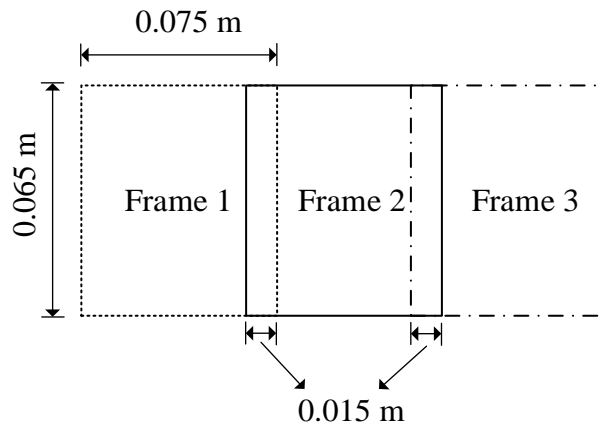
column with  $20\mu$  seeding particle (GLS- $20\mu$ ), and (iv) GLS with  $350\mu$  fine sand (GLS- $350\mu$ ). Tap water, compressed air, seeding particles and fine sand were used as liquid, gas, and solids respectively.



(a)



(b)



(c)

Figure-3.1: Schematic of (a) experimented pseudo rectangular column with optical probe measurement locations; (b) distributor plate and (c) PIV field of view

A submersible pump was used to recirculate liquid between a storage tank and the column. For the GL and GLS experiments, water, and sand particles (1% by weight) were introduced from the top of the column in a batch mode, and the initial liquid height was maintained at 0.55 m from distributor plate. Perforated plate distributor with 100 holes of 1 mm diameter (Figure-3.1b) located above 0.1 m from the inlet was used to provide uniform distribution of gas into the liquid phase. The field of view for the camera in PIV experiments was 0.075 m · 0.065 m as shown in Figure-3.1(c). At each axial location (Y), the camera position in PIV setup was traversed radially from Frame 1 to Frame 3 (X = 0 to 0.2 m). Overlap distance of 0.015 m was maintained between the consecutive frames to avoid the influence of bad vectors on resultant velocity. Operating conditions and optical probe measurement locations are listed in Table-3.1. The operating conditions were chosen in such a way to demonstrate the

ability of optical probe to measure gas phase in both low gas holdup and dense gas flow conditions. For instance superficial gas velocity of 0.13 m/s resulted in gas holdup values less than 10% whereas 0.25 m/s resulted in holdup values up to 50%. Similarly superficial liquid velocity was selected such that the probe encounters seeding particles at both laminar and turbulent flow conditions.

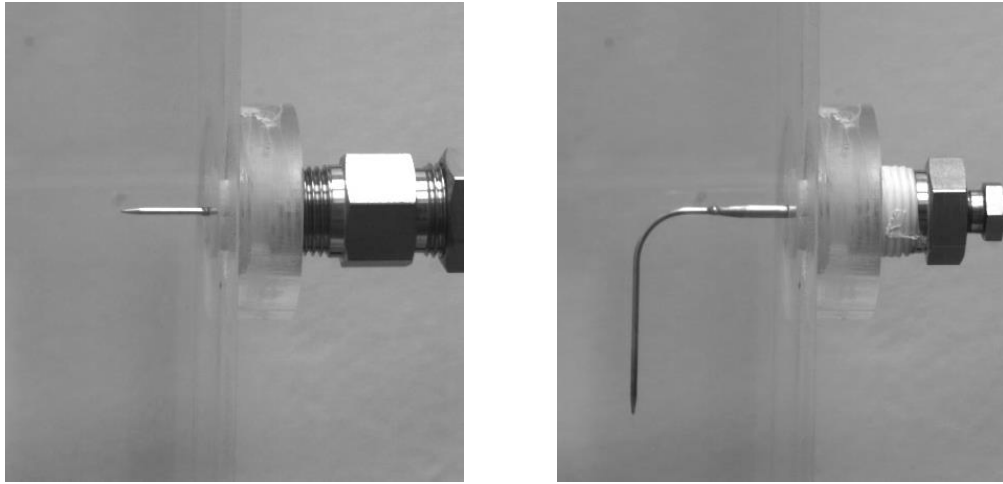
Table-3.1: Operating Parameters and measurement locations

Superficial liquid velocity, m/s	0.025, 0.033, 0.042
Superficial gas velocity, m/s	0.13, 0.17, 0.25
Seeding particle diameter, $\mu\text{m}$	20
Sand particle diameter, $\mu\text{m}$	350
Axial locations (Y1-Y6), m	0.10, 0.25, 0.40, 0.55, 0.70, 0.85
Radial locations (left to right), m	0.03, 0.06, 0.09, 0.12, 0.15, 0.18

### 3.3 MEASUREMENT TECHNIQUES

#### 3.3.1 Optical probe

Optical probe measurement system used in this work consisted of a custom-made single tip probe and an optoelectronic module (a laser diode, a beam splitter, a polarizer, a photomultiplier and A/D convertor) procured from A2 Photonics (120). Probes of two different geometry namely straight probe and bent probe were used in this work as shown in Figure-3.2.



(a) straight probe

(b) bent probe

Figure-3.2: Optical probes used in this study

Based on the gas flow direction in the experiments either a straight or bent probe was employed. The optical probes had a short sensing tip with a length of  $32\ \mu\text{m}$  which enabled measurement of small bubbles ( $< 500\ \mu\text{m}$ ) with an accuracy of  $\pm 5\%$ . The probe tip was connected to an optoelectronic module by two optical fibres, one supplied laser light to the tip, and other transmitted the reflected light back to data acquisition system. Optoelectronic module supplied  $1550\ \text{nm}$  wavelength laser pulses at  $15\ \text{MHz}$  frequency to the probe tip. The laser light sent to probe tip was emitted into medium if probe tip was surrounded by liquid (refractive index,  $n = 1.33$ ) or was reflected back if probe tip was surrounded by gas ( $n = 1$ ). The light intensity received back from probe tip was converted into a voltage signal in the data acquisition system. The detected voltage signal is shown in Figure-3.3(a). If probe tip encountered a gas bubble, a sharp rise in voltage was detected. Similarly, when a gas bubble left the probe tip, fall in output voltage was sensed. The rise and fall in voltage with a trapezoidal plateau was used to identify a bubble (Figure-3.3b). Similarly, when a particle approaches the probe vicinity, voltage signal exhibited series of oscillations with no plateau (Figure-3.3c) by which a solid phase (particle) could be distinguished from the gas phase (bubble). When the probe tip pierced the bubble interface at an angle close to normal, the output voltage signal featured a square or trapezoidal plateau as shown in Figure-3.3(d). In a highly turbulent flow field, often bubbles drift away from the probe tip causing improper piercing of the bubble resulting in partially developed



voltage peak as shown in Figure-3.3(e). Furthermore, bubbles which pierce probe tip closer to normal angle exhibit distinct oscillations/fringes (Figure-3.3f) at the time of entry and/or exit at probe tip due to the Doppler effect. Such oscillations in partially developed voltage peaks are very few and undistinctive (Figure-3.3g).

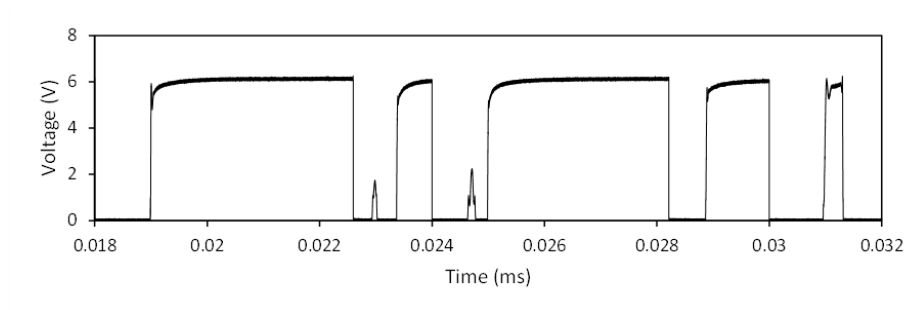
Identifying a valid bubble from the complex voltage signal could be challenging. Initially, the optical probes were calibrated by simultaneously measuring bubble chord length using high speed camera, and optical probe techniques. Bubbles which pierced the probe tip closer to normal angle were identified using high speed images, and corresponding exit oscillations obtained using optical probe were analyzed. It was found that properly pierced bubble exhibited a minimum of 10 oscillations/fringes when bubble leaves the probe tip (Figure-3.3f). Signal filter, and fast Fourier transform (FFT) were also used to detect a valid bubble. The raw signal was initially filtered using through a band pass filter which varied between 100 kHz – 9000 kHz based on the operating conditions and experimented system. FFT of the band passed signal was calculated to identify the Doppler frequency which varied between 400 kHz to 1300 kHz. For example, in gas-liquid bubble column experiments, 150 – 574 kHz band pass filter was used and the Doppler frequency varied between 300 – 380 kHz. A high pass filter with threshold frequency equal to 10% of the Doppler frequency was then used for obtaining filtered time varying signal. FFT of the filtered time varying signal was calculated to obtain inverse fringing period. A bubble was deemed as a valid bubble if the difference between the Doppler frequency and inverse fringing period was less than 10%.

The local gas holdup, bubble and particle velocity, and bubble chord length were calculated using following equations:

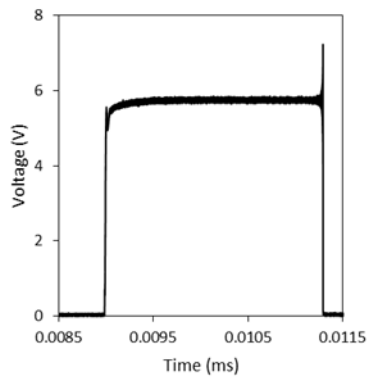
$$\varepsilon_g = \frac{\Sigma T_G}{T_T} ; V_p \text{ and } V_b = f \frac{\lambda}{2n} ; \phi = V_b * T_G$$

Here,  $\lambda/n$  is the laser wavelength in water,  $T_G$  is the time spent by probe tip inside a single gas bubble which is also referred as residence time,  $T_T$  is total measurement time,  $\varepsilon_g$  is the time-averaged local gas holdup,  $V_b$  is bubble velocity,  $V_p$  is particle velocity  $f$  is oscillation frequency, and  $\phi$  is chord length. As the particles could not be pierced by optical probe, size of the particles could not be inferred. For all the experimental data reported in this thesis, optical probe measurements were recorded

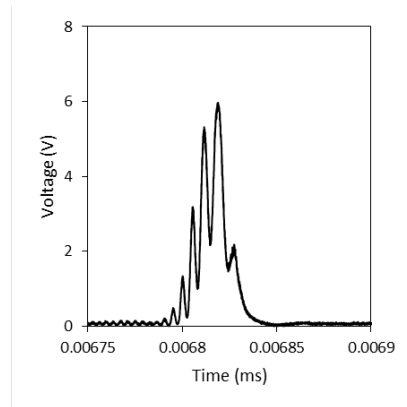
for 2 minutes duration, which ensured the detection of more than 1000 valid bubbles and particles.



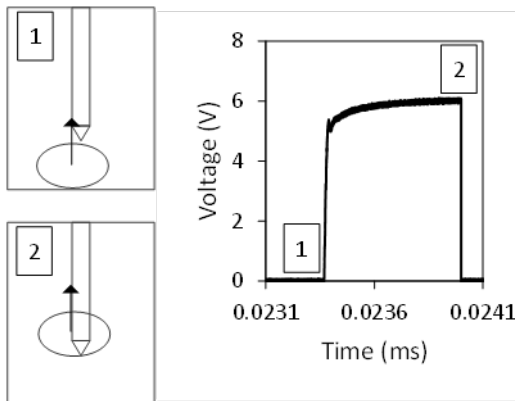
(a)



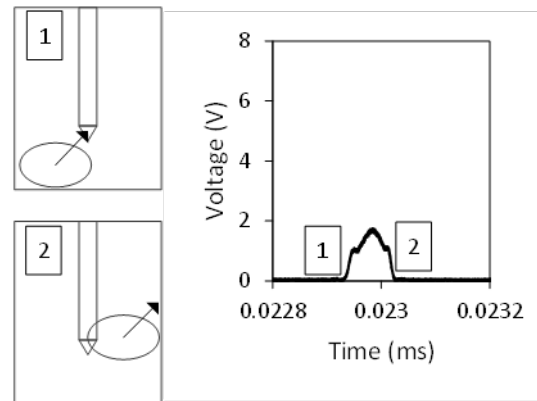
(b)



(c)



(d)



(e)

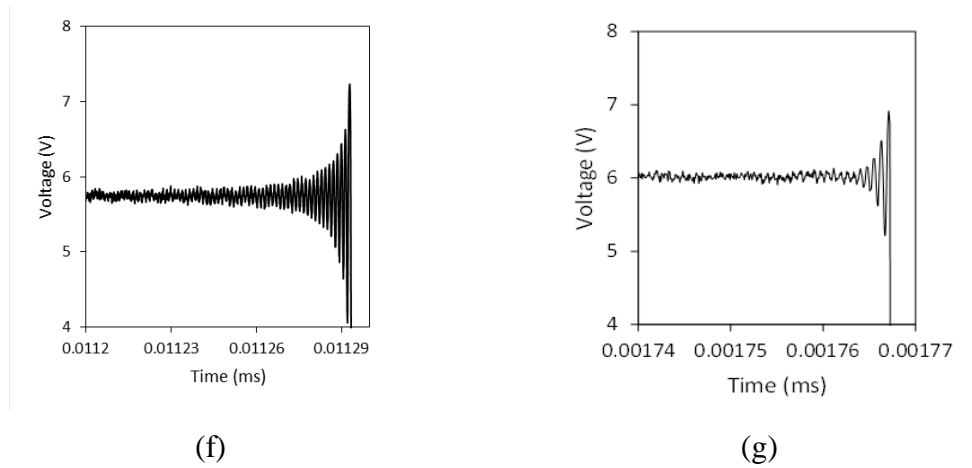


Figure-3.3: (a) Optical probe signal in a gas-liquid-solid system; (b) Signal for probe piercing a bubble; (c) Signal when probe encounters a particle; (d) Signal for probe piercing a bubble close to normal; (e) Partially developed voltage signal due to improper piercing; (f) Voltage fluctuation at exit for valid bubble (distinct oscillations with more than 10 fringes) and (g) Voltage fluctuation at exit for invalid bubble (distinct oscillations with less than 10 fringes)

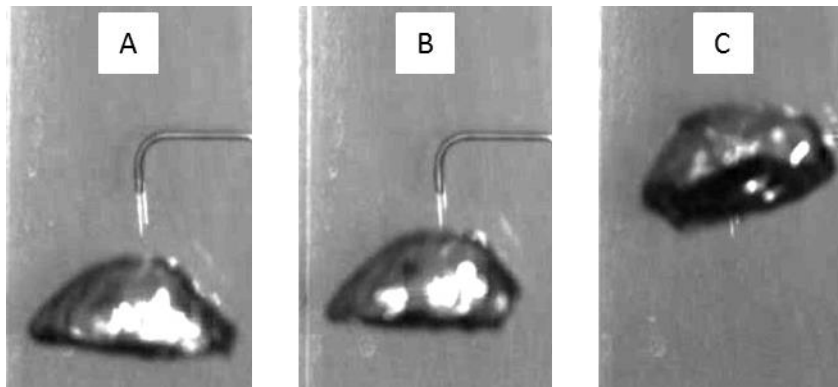
$$[U_L = 0.013 \text{ m/s}; U_G = 0.25 \text{ m/s}]$$

It was further confirmed that the statistical average of calculated phase velocities remained invariant with further increase in measurement duration. Measurements were carried out in triplicates to verify the reproducibility of data. To maximize the number of bubbles captured by probe tip, the probe needs to be oriented opposite to prevalent flow direction. In a bubble column, this can be readily ensured. However, for stirred tanks, the flow is not always unidirectional. This can pose difficulties in maintaining probe orientation opposite to flow direction. Therefore, it is critical to account for errors caused by probe orientation. As per Mueller et al., (48) suggestion, measurements were taken with two probe orientations (probe tip facing upward and downward), and only higher bubble frequency values were reported as they represent a higher number of valid bubbles. The effect of probe orientation is discussed in detail in Chapter-5, Section-5.3.3 (121).

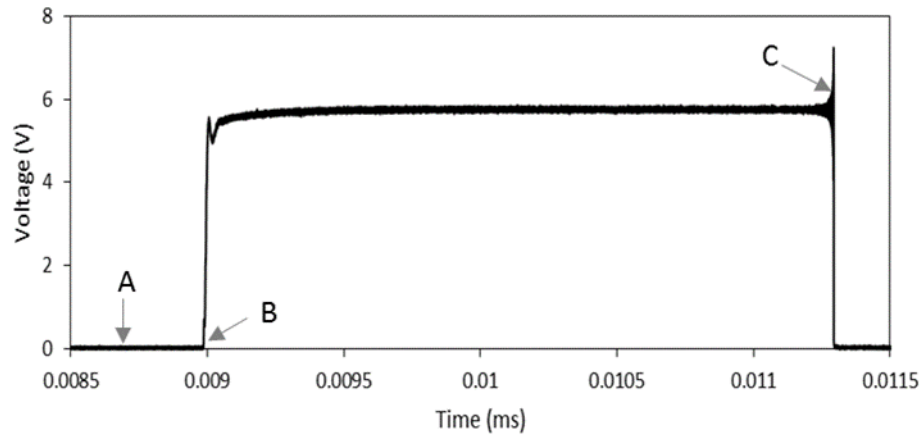
### 3.3.2 High speed imaging

High speed imaging (HSI) experiments were carried out to verify bubble chord length obtained from optical probe measurements. Nikon AF Nikkor 50 mm f/1.8D lens attached to Photron FASTCAM was used to record gas bubbles at 1000 frames per

second. Experiments were performed in triplicate and it was ensured that each experiment captured at least 500 bubbles. The bubbles were injected using a syringe into the column filled with tap water. LED array light source was kept perpendicular to the pseudo rectangular column to illuminate the measurement plane. High speed images of the probe tip piercing a single gas bubble are shown in Figure-3.4(a), and the corresponding voltage signal exhibited by optical probe technique is shown in Figure-3.4(b). The voltage signal can be characterized using 3 points (A-C) illustrated in both Figures. Point A indicates when the probe tip is in contact with the liquid phase. Point B represents the time at which tip starts penetrating a bubble and voltage starts varying from liquid to gas phase. Point C represents the time when a gas bubble leaves probe tip, and the voltage drops from gas to the liquid phase. Gas bubbles collected from high speed images were processed using open source software, ImageJ. Image processing involved background noise removal, thresholding, binarization, and outline tracking to calculate bubble chord length as shown in Figure-3.4(c).



(a)



(b)



(c)

Figure-3.4: (a) Snapshots of an optical probe tip piercing a single bubble; (b) voltage signal of a bubble exhibiting three characteristic points (A-C) and (c) post-processing of the pierced bubble using ImageJ software

### 3.3.3 Particle image velocimetry

Table-3.2: PIV Parameters

Data acquisition frequency	15 Hz
Laser type	Nd: YAG laser
Wavelength	550 nm
Pulse delay	60 to 200 $\mu$ s (based on $U_L$ and $U_G$ )
Pulse energy	15 mJ/pulse
Recording method	Dual frame/double exposure
Recording medium	Full frame interline transfer CCD

Lens focal length	135 mm
Lens aperture number	16
Interrogation area	32 × 32 pixels
Observation distance	0.95 m
Seeding material	Hollow glass beads (20 μm)

A time-resolved, two-dimensional PIV system was used in this study. PIV experimental setup was a combination of several subsystems, i.e. laser light source, high speed camera, optical lenses and a synchronizer. Parameters for PIV used in this study are given in Table-3.2. A set of spherical (to control sheet thickness), and cylindrical lenses (to control sheet height) were used to form a light sheet from the laser beam. Laser light sheet was aligned to coincide with the centre of the optical probe inserts. It was ensured that minimum eight seeding particles were present per interrogation area for cross-correlation analysis. Optimal aperture f16 was chosen, such that depth of field was greater than the laser light thickness. 1000 images were acquired in each experiment to minimize the uncertainties in velocity measurements.

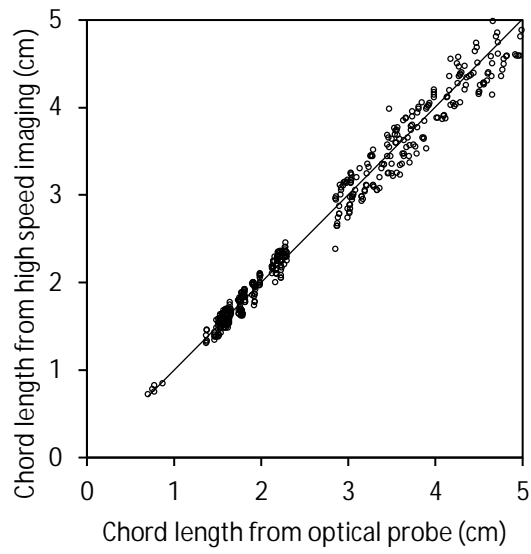
### **3.4 RESULTS AND DISCUSSION**

#### **3.4.1 Validation of optical probe measurements**

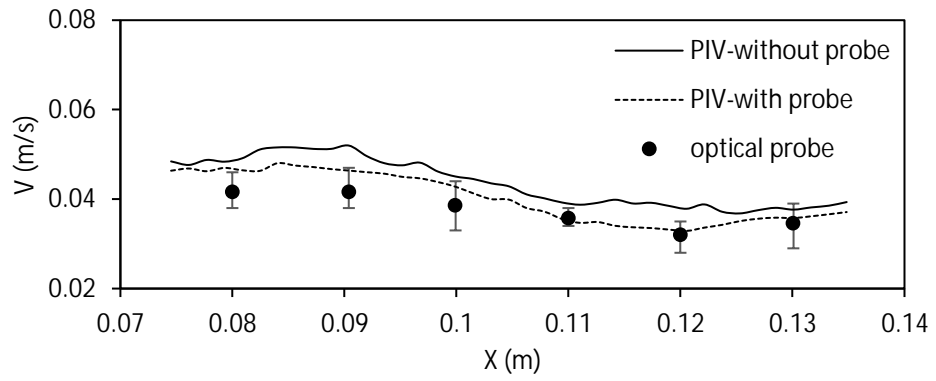
The important aspect to be accounted while employing a new measurement technique is to evaluate its accuracy. Therefore, preliminary studies were carried out to validate the optical probe measurements. High speed imaging (HSI) technique was used to validate the bubble chord length measurements by many researchers in the past (122-127) and same methodology was adopted in this study. In the entire thesis, bubble size is represented in terms of bubble chord length (should not be confused with bubble diameter). Bubble chord length from high speed imaging was calculated by measuring the major axis of each bubble when the probe tip starts piercing a bubble (Point B in Figure-3.4). Since ImageJ could not recognize bubbles in a group or coalescing bubbles, controlled experiments were carried out by sparging gas at very low gas velocity. In addition, instead of sparging gas through a distributor plate (Figure-3.1b),

gas was sparged through a gas nozzle located at the centre ( $X = 0.1$  m). The optical probe was placed at axial location of Y3 and aligned collinear to the centre of the hole such that it encounters most of the bubbles. Three sets of 500 valid bubbles were simultaneously captured using both techniques, and the comparison of chord length is shown in Figure-3.5(a). It was found that the variation between chord lengths confined within  $\pm 8\%$ .

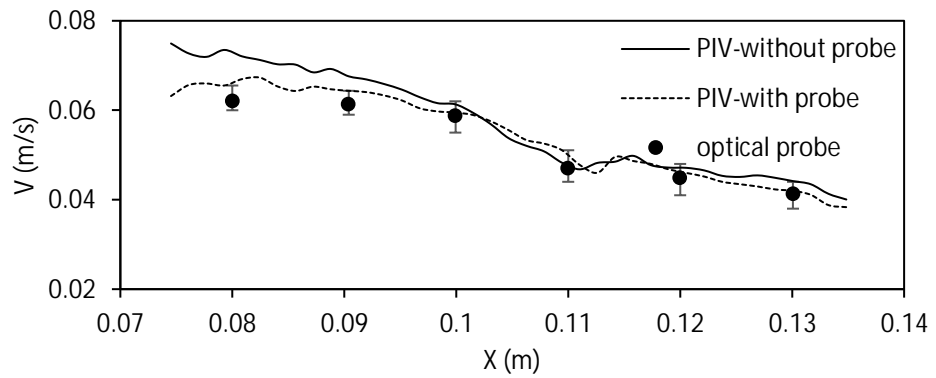
PIV is a well-established tool for single phase flow measurements, and has been used to validate other experimental techniques (128-131). In PIV measurements, liquid velocity is calculated based on tracking the micron sized seeding particles. It is proven that the seeding particles do not affect flow field, and follow fluid motion (132). Therefore, the 2D-PIV system was used to validate seeding particle velocity obtained from optical probe measurements. All PIV data were collected for 66.66 s which consisted of 1000 image pairs. Optical probe measurements were also conducted for 67 s for time-averaged velocity comparison. Only difference in the comparison studies was that the data acquisition frequency for PIV system was 15 Hz while it was 15 MHz for optical probe. Optical probe calibration experiments indicated that to detect a very fine particle (20  $\mu\text{m}$  seeding particle), data acquisition frequency should be above 13 MHz. Due to this significant variation in acquisition frequency, turbulence characteristics could not be compared between PIV and optical probe data. However, resultant velocity magnitude ( $V$ ) of the seeding particles was compared with PIV experiments. In order to determine the effect of intrusive nature of probe on flow field, initially three sets of experiments were carried out: (1) PIV measurement without probe, (2) PIV measurement with an optical probe in the flow domain, and (3) optical probe measurement. Measurements were carried out at two different superficial liquid velocity ( $U_L$ ) at 0.55 m above the distributor plate (Y4). Frame-2 (see Figure-3.1c) was selected as a field of view for PIV measurements. From Figure-3.5(b&c), it is evident that with the probe in the flow domain, the velocity magnitude was marginally reduced. However, a good agreement between the optical probe and PIV-with probe was observed in all measurements. At low liquid velocities ( $U_L = 0.025$  m/s), variation in resultant velocity magnitude was 20% whereas, higher liquid velocities ( $U_L = 0.042$  m/s), the difference reduced up to 13%.



(a)



(b)  $U_L = 0.025$  m/s

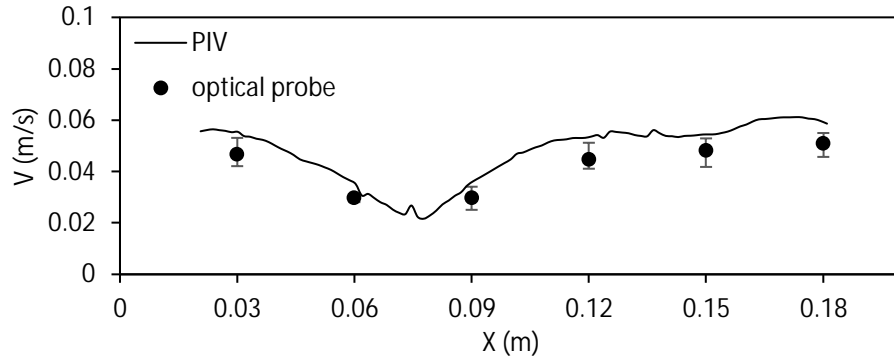


(c)  $U_L = 0.042$  m/s

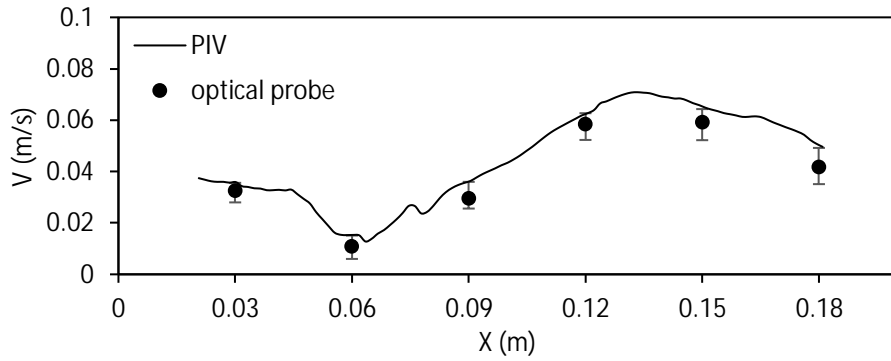


Figure-3.5: (a) Comparison of chord lengths calculated using high speed imaging and optical probe techniques and (b) & (c) Comparison of velocity magnitudes with and without probe (Y3 & Frame-2) at different superficial liquid velocity

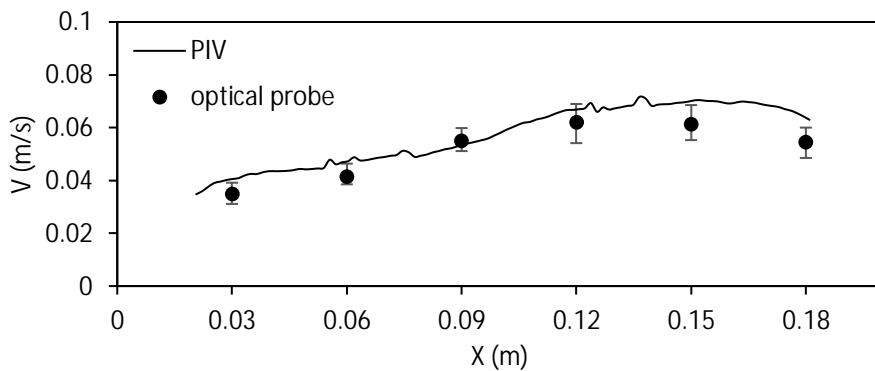
### 3.4.2 Liquid velocity profiles



Y2 = 0.25 m

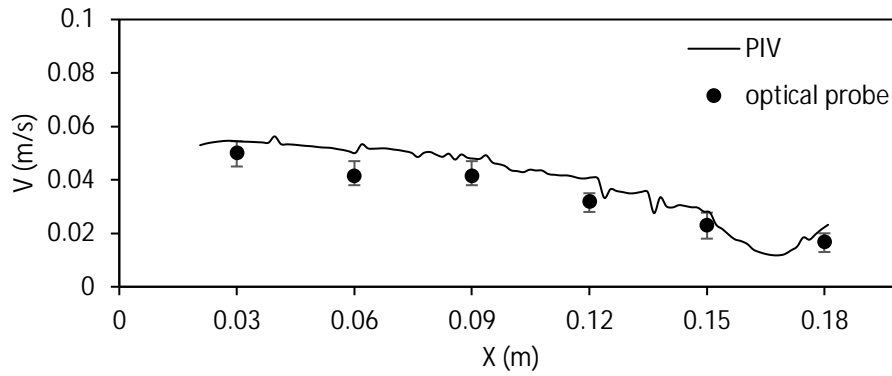


Y4 = 0.55 m

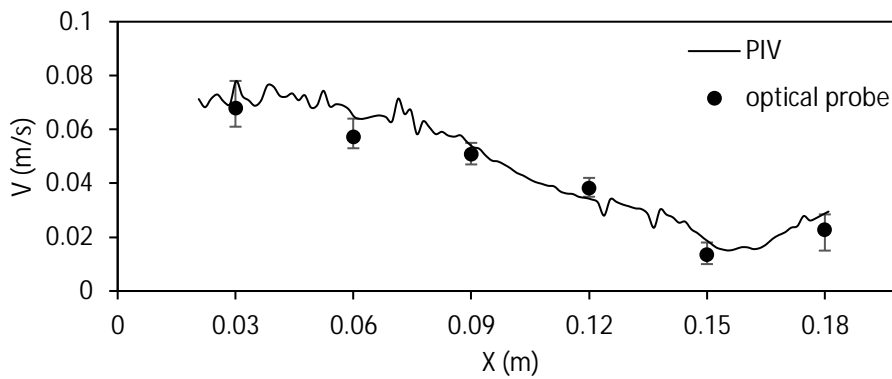


Y6 = 0.85 m

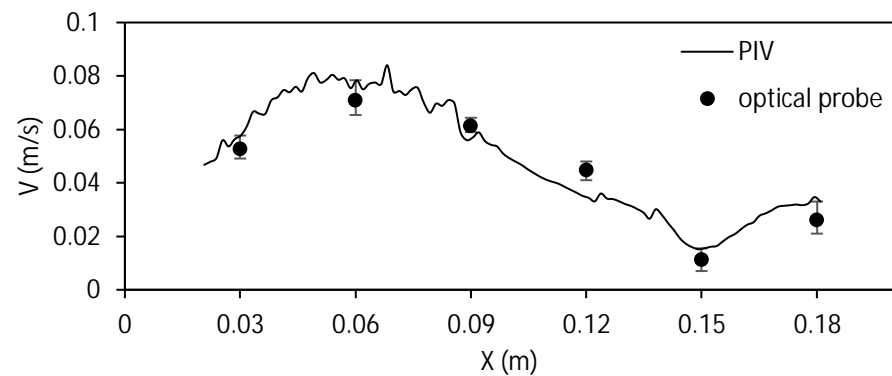
(a)



$U_L = 0.025$  m/s



$U_L = 0.033$  m/s



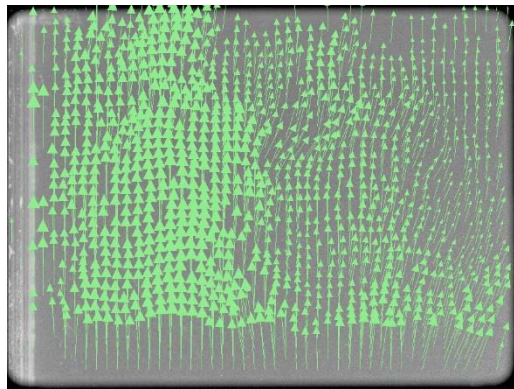
$U_L = 0.042$  m/s

(b)

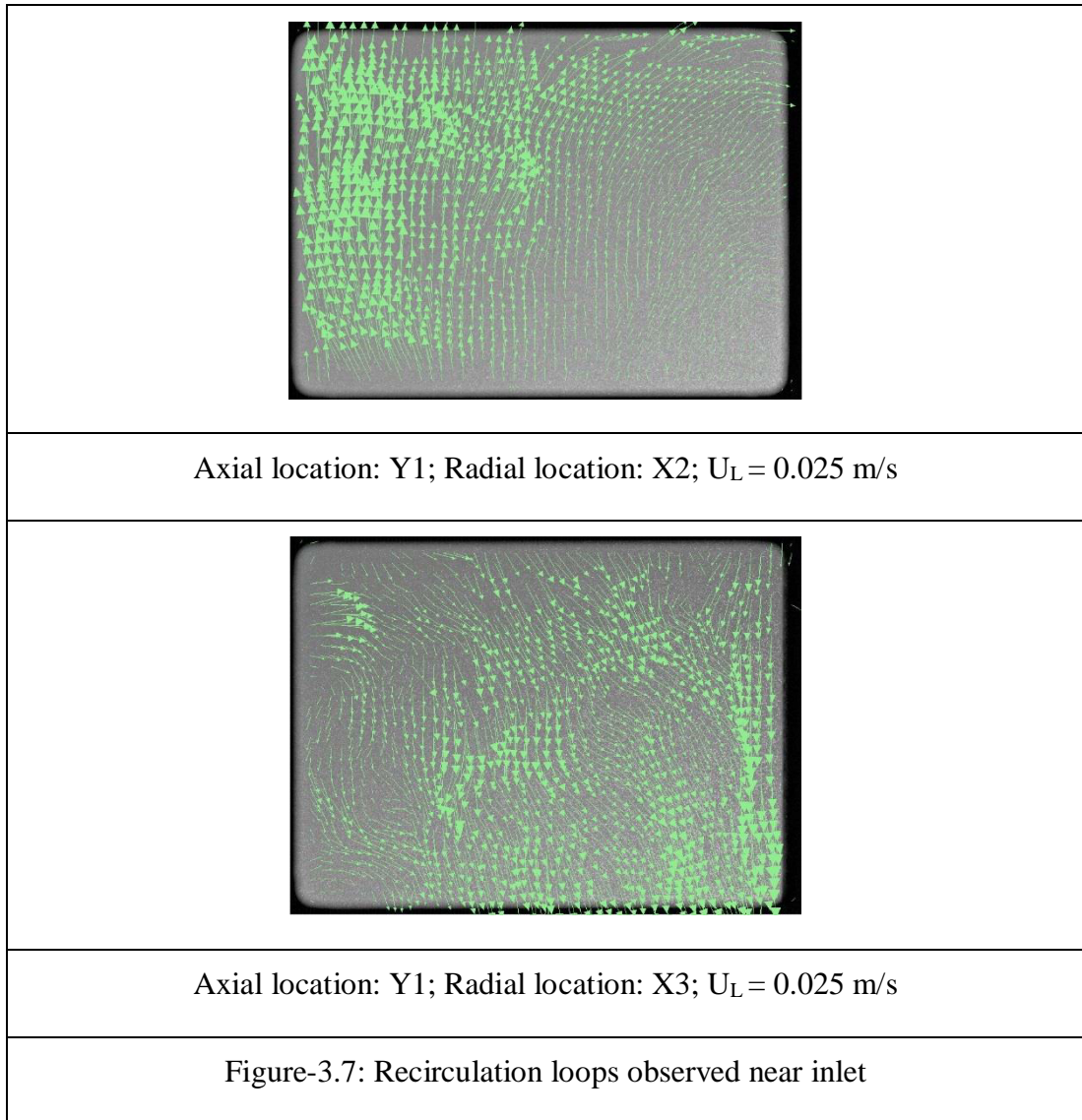
Figure-3.6: Variation of seeding particle velocity magnitudes with (a) axial locations (fixed  $U_L = 0.033$  m/s) and (b)  $U_L$  on (fixed  $Y = 0.40$  m)

Figure-3.6(a) shows the time-averaged liquid ( $20\mu$  seeding particle) velocities obtained from the two techniques at various axial and radial locations at a fixed  $U_L$  of  $0.033$  m/s. Variations in the velocity magnitude between optical probe and PIV were found to be very small. The optical probe measurements were reproducible with a

variance limited to +/- 15%. At bottom section of the column (Y2 and Y4), liquid velocity initially increased from radial positions of  $X = 0$  to 0.03 m; drops back and increased again from 0.07 to 0.15 m. Reason for such rise and dip pattern in radial liquid velocity profile is that the liquid recirculation experiments were conducted in turbulent flow regime where the flow was not fully developed at axial locations close to liquid distributor. Due to this, recirculation loops were observed (from PIV images as shown in Figure-3.7). However, same profile was not observed at the top section of the column (Y6). Here, liquid velocity steadily increased from 0.02 m/s to 0.06 m/s (from  $X = 0$  to  $X = 0.16$  m) and then decreased as it approached wall. Such velocity profile could be attributed to a strong upward liquid flow in the centre and down flow near the walls. In order to evaluate the impact of superficial liquid velocity on optical probe measurements, data obtained at three varying  $U_L$  was analysed (Figure-3.6b). The optical probe measurements were not affected by variation in  $U_L$ . At all liquid superficial velocities, radial velocity profile looked qualitatively similar. Liquid velocity gradually increased near the left corner ( $X = 0$  to 0.05 m) of the column and dropped down as we move from  $X = 0.05$  towards wall. Furthermore, with the increase in  $U_L$  from 0.025 to 0.042 m/s, the peak liquid velocity shifted from wall ( $X = 0.03$  m) to centre ( $X = 0.06$  m).

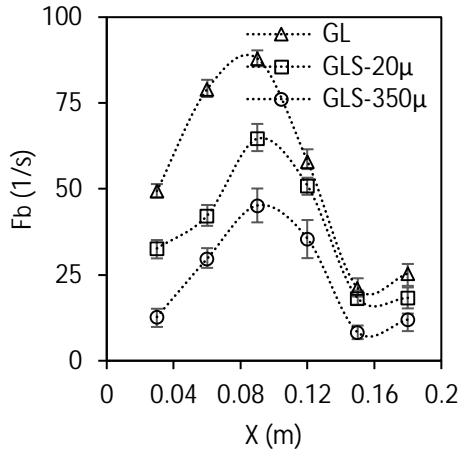


Axial location: Y1; Radial location: X1;  $U_L = 0.025$  m/s

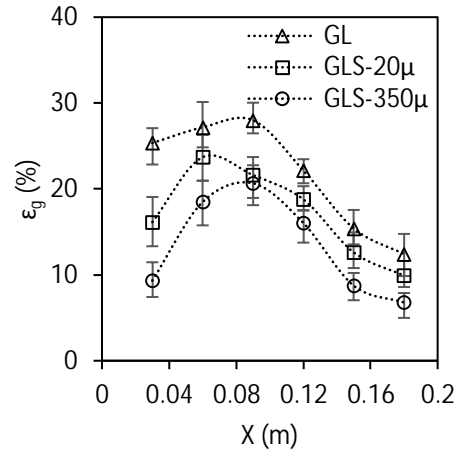


### 3.4.3 Simultaneous measurements of local bubble dynamics and particle velocities

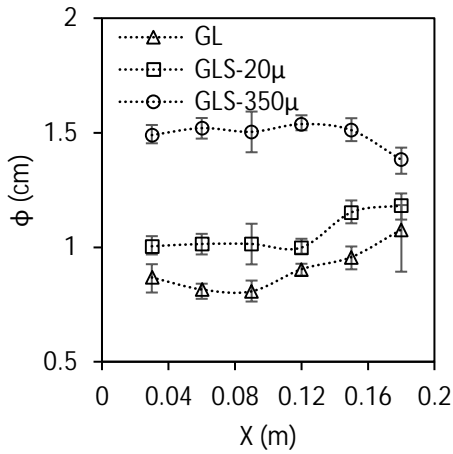
The ability of the new optical probe to simultaneously measure local bubble dynamics and particle velocity was examined by carrying out two sets of slurry bubble column experiments (GLS-20 $\mu$  and GLS-350 $\mu$ ) at a fixed  $u_g$  of 0.13 m/s. Here, GLS-20 $\mu$  and GLS-350 $\mu$  stands for gas-liquid-solid system with either seeding particles (20 $\mu$  size) or fine sand (350 $\mu$  size) as solid phase respectively. 1% by weight slurry concentration was fed in batch mode for both experiments. Figure-3.8(a-d) shows the effect of addition of solids and particle size on radial profiles of bubble frequency, gas holdup, chord length, and bubble velocity respectively.



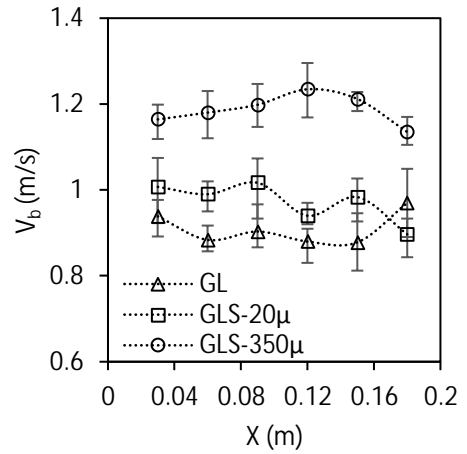
(a) bubble frequency



(b) gas holdup



(c) bubble chord length



(d) bubble velocity

Figure-3.8: Effect of addition of solids and particle size on local bubble hydrodynamics in slurry bubble column

In the plots, GL data represents the results from gas-liquid bubble column experiments as discussed in the previous section. Addition of solids reduced bubble frequency, and promoted bubble coalescence, which led to formation of larger bubbles. Eventually bubble rise velocity increased, and gas holdup reduced significantly. Especially, at centre ( $X = 0.09$  m), bubble frequency reduced by 47%, and 95% with addition of  $20\mu$ , and  $350\mu$  particles respectively. However, variation in bubble frequency was minimal near the wall ( $X = 0.15$ , and  $0.18$  m). Bubble chord length increased from approximately 1 cm to 1.5 cm with solid loading. It should be noted that apart from particle size, porosity and density also varied between  $20\mu$  seeding particles, and  $350\mu$

fine sand. Therefore, from current experiments we can only conclude that addition of solids affects local bubble dynamics significantly but a detailed work needs to be done to understand the factors responsible for this variation.

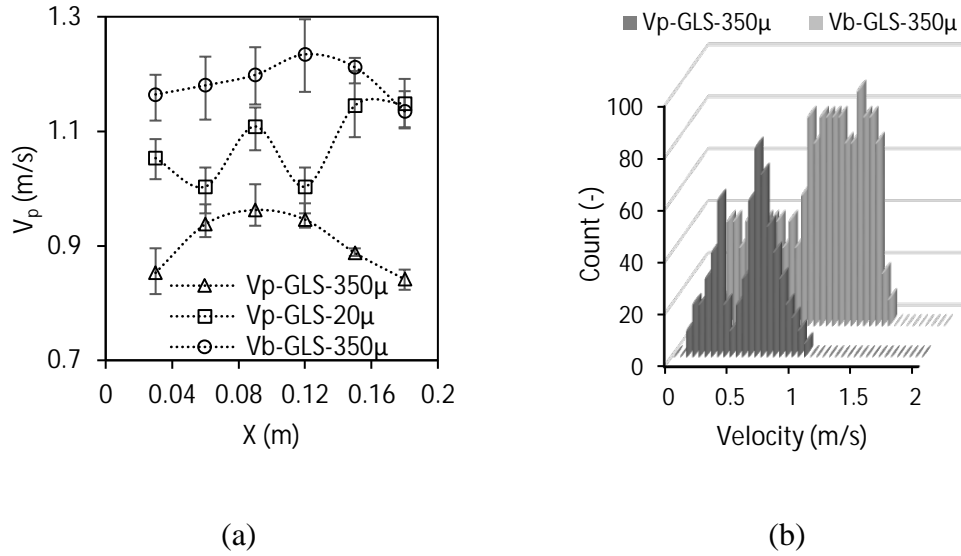


Figure-3.9: Effect of particle size on bubble & particle velocity and (b) bubble and particle velocity distribution

Time-averaged bubble, and particle velocity using the optical probe is shown in Figure-3.9(a). At all radial positions, bubble velocity was found to be higher than that of the particle velocity. For GLS-20 $\mu$ , particle velocities fluctuated between 0.97, and 1.2 m/s and rise and dip pattern was observed in the radial velocity profile. Particle velocity increased from radial positions of 0.03 to 0.09 m then reduced at 0.12 m and increased again at 0.15 m. On the other hand, particle velocity for GLS-350 $\mu$  showed a concave profile with peak velocity at centre and low velocities near wall. Such variation in velocity profiles could be attributed to the reduction in liquid velocity fluctuations with addition of dense solid particles. Figure-3.9(b) shows the variation in velocity distribution between gas bubbles, and 350 $\mu$  particles obtained from GLS-350 $\mu$  experiments. It was found that, addition of solids resulted in wide distribution of gas bubble velocities compared to GL system (compare Figure-3.9b and 3.8d). The reason could be due to the change in liquid flow pattern, and increase in bubble coalescence with solid loading. Particle velocities were found to be approximately 50% lower than bubble velocities with a distribution range between 0 to 1 m/s.

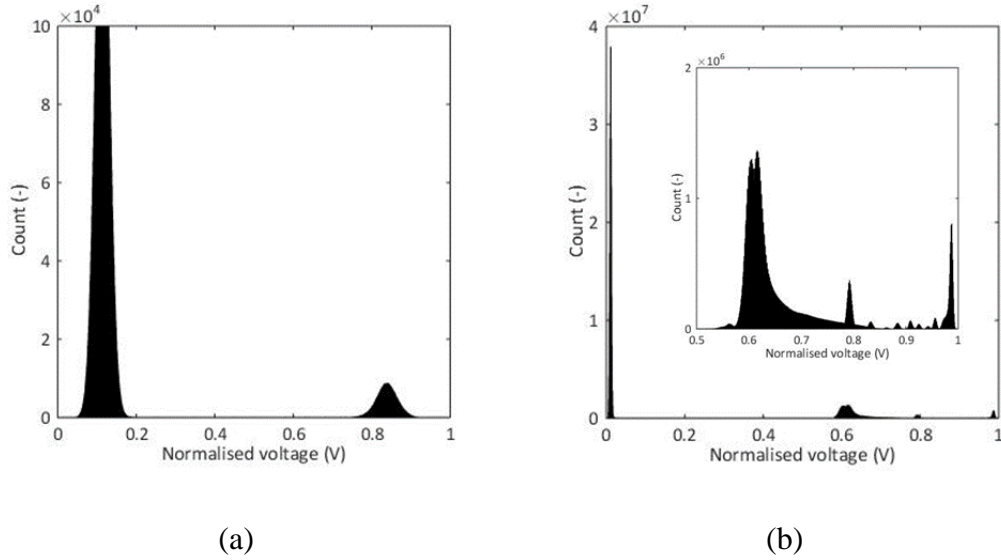


Figure-3.10: Normalized voltage distribution for Case-1 and Case-2

While the results so far demonstrated the capacity of the optical probe to measure gas, and solid phase simultaneously, efforts have also been made to investigate whether the probe was capable of measuring all three phase velocities instantaneously. Two cases were considered for this analysis. In Case-1 (GL), gas bubbles were sparged into the column at 0.13 m/s. For Case-2 (GLS), both 20 $\mu$  and 350 $\mu$  seeding particle with 1% slurry concentration were introduced into the column in batch mode and gas was sparged at 0.13 m/s. For both cases, tap water was filled till 0.55 m from the distributor plate. Figure-3.10(a) and (b) shows the histograms of the normalized voltage obtained from Case-1 and Case-2 respectively. The raw voltage was converted into normalized voltage using following equation,

$$\text{Normalized voltage} = \frac{\text{measured voltage} - \text{minimum voltage}}{\text{maximum voltage} - \text{minimum voltage}}$$

Two distinct peaks can be observed for Case-1 (Figure-3.9a), with voltage values from 0 to 0.2 V representing liquid phase and 0.7 to 0.9 V denoting gas phase. Difference in voltage values corresponds to the amount of laser light received back by data acquisition system. For Case-2 (Figure-3.9b), voltage values for liquid phase shifted close to 0 V and for gas phase it shifted close to 1. It was expected that voltage peaks between liquid phase and gas phase should correspond to hollow glass beads (20 $\mu$  seeding particle) and fine sand (350 $\mu$ ). Since the refractive index (n) of both particles was in a similar range (n = 1.2 to 1.44), it was difficult to identify a specific voltage peak corresponding to the size of particle. In addition, from 0.8 to 0.9 V couple of

small peaks were observed (see inset Figure-3.9b) which could be due to particle clusters hitting the probe tip or increase in noise due to solid loading. It was also found from the analysis that, optical probe frequently detected large sized particle ( $350\mu$ ) in comparison with finer particles ( $20\mu$ ). This could be attributed to the variation in dominant frequency generated by different sized particles. By Doppler effect, time taken for the waves (frequency) generated by larger particles to reach probe tip will be less compared to those from smaller particles. Therefore, when both  $350\mu$  and  $20\mu$  particles approached probe tip with same velocity, optical probe could only capture frequency generated by  $350\mu$  particle. Abovementioned results suggested that in order to detect all three phases simultaneously, either controlled experiments (with few particles) need to be carried out or a robust signal processing method needs to be developed.

### **3.5 SUMMARY**

Simultaneous measurements of local bubble hydrodynamics and particle velocities in gas-liquid-solid system using a single-tip optical probe which works on principle of light reflection in conjunction with Doppler effect was demonstrated in this chapter. The probe was capable of detecting bubbles as small as  $500\mu\text{m}$  and particles in the size range of 15 to  $450\mu\text{m}$ . Preliminary validation experiments were carried out to evaluate the accuracy of optical probe measurements. PIV and high speed imaging techniques were used to verify seeding particle velocity and bubble chord length respectively. It was found that the discrepancies in seeding particle velocity was 20% at low superficial liquid velocity ( $U_L = 0.025\text{ m/s}$ ), whereas the difference reduced up to 13% when  $U_L$  was increased to  $0.042\text{ m/s}$ . On the other hand, variation in bubble chord length between probe and HSI was confined to  $\pm 8\%$ . Validation experiments were followed by dense gas flow experiments ( $u_g = 0.13, 0.17$  and  $0.25\text{ m/s}$ ) to verify the potential of new optical probe to measure high gas fractions. Maximum gas holdup of 43% was recorded at  $u_g = 0.25\text{ m/s}$  at the centre of column ( $X = 0.09\text{ m}$ ;  $Y = 0.40\text{ m}$ ). Furthermore, the ability of probe to simultaneously measure local bubble dynamics and particle velocity was demonstrated by carrying out two sets of slurry bubble column experiments (GLS- $20\mu$  and GLS- $350\mu$ ) at a fixed  $u_g$  of  $0.13\text{ m/s}$ . Addition of solids, reduced the bubble frequency at  $X = 0.09\text{ m}$  by 47% and 95% with addition of  $20\mu$  and  $350\mu$  particles respectively. Solid loading promoted bubble coalescence which led to increase in chord length from approximately 1 cm to 1.5 cm. At all radial



positions, bubble velocity was found to be higher than the particle velocity. Particle velocities were found to be approximately 50% lower than bubble velocities with a distribution range between 0 to 1 m/s. Efforts have also been made to examine whether the new probe could measure all three phase velocities instantaneously. It was found that optical probe mostly detected large sized particle (350 $\mu$ ) in comparison with finer particles (20 $\mu$ ). When both 350 $\mu$  and 20 $\mu$  particles approached probe tip at same instant, optical probe was able to detect only the frequency generated by 350 $\mu$  particle. The analysis presented in this chapter suggests that the optical probe is a reliable flow measurement tool which can be employed for dense flow multiphase systems to measure local bubble hydrodynamics.

## **Chapter 4**

# **Vortex shape and gas-liquid dynamics in unbaffled stirred tank**

### **4.1 INTRODUCTION**

In the previous chapter, ability of optical probe to measure local bubble hydrodynamics in dense flow conditions was demonstrated using a bubble column. The flow in stirred tank is highly turbulent compared to bubble column. Moreover, due to impeller rotation it also exhibits comparable radial and axial flows. Therefore, further experimental verification is necessary before employing the probe in highly turbulent baffled stirred tanks. One of the ways to explore the capability of probe to investigate stirred tank hydrodynamics is to carry out experiments in unbaffled tank. Therefore, objective of this study is to describe the local hydrodynamics and vortex shape in unbaffled tank using optical probe technique. Slow mixing times, relatively small gas transfer rates and less power consumption are the key advantages of an unbaffled stirred tank (31, 32). For the above mentioned reasons, self-ingesting unbaffled stirred tanks are identified as a possible alternative to sparged baffled tanks for specific applications such as bio-reactors, crystallizers, etc.,. Previous experimental and modelling studies on unbaffled stirred tank listed in Chapter-2 (Table-2.3) indicated that most of research were focused on predicting vortex shape without vortex ingestion. Recently, Busciglio et al., (82) provided analytical model to predict vortex shape with ingestion. In addition to vortex shape, data on gas and liquid phase hydrodynamics with vortex ingestion are critical to design a self-ingesting unbaffled stirred tank. To understand the impact of vortex on gas-liquid velocity distribution, CFD simulations were carried out (86, 87, 137). Therefore, effect of vortex ingestion on vortex shape in a 0.24 m tank equipped with four bladed disc turbine was investigated using optical probe measurement and volume of fluid (VOF) simulations.

## 4.2 MATERIALS AND METHODS

### 4.2.1 Experimental setup

A schematic diagram of the experimented un baffled tank with dimensions is shown in Figure-4.1(a). The tank was a flat-bottomed acrylic tank, which was filled with water up to 0.24 m ( $H_L = T$ ) height. Impeller assembly consisted of a disc turbine with four blades (0.025 m wide and 0.012 m tall), mounted onto a shaft. Impeller speed was controlled by a variable speed drive and experiments were carried out at six impeller speeds from 300 to 800 rpm. Optical probe was mounted on the tank wall through probe inserts located at six axial positions of  $z = 0.04, 0.08, 0.12, 0.16, 0.20,$  and 0.24 m from the bottom. Figure-4.1(b) shows a top view of the tank with straight and bent probes mounted on the tank. The straight probe was traversed radially from wall to gas-liquid interface at each axial position to measure vortex co-ordinates, whereas bent probe was used to measure gas holdup, and bubble size.

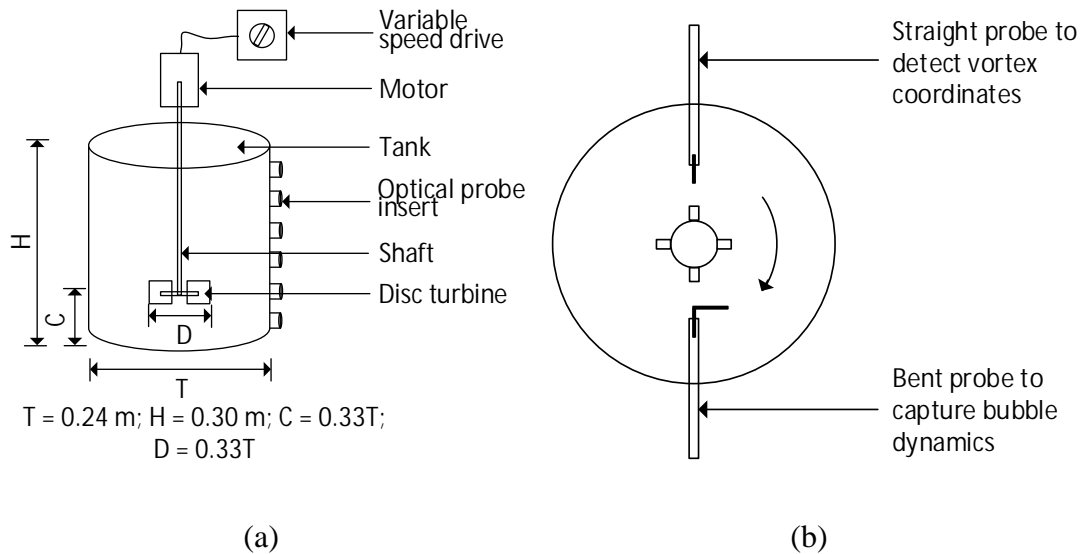


Figure-4.1: Schematic diagram and geometrical configuration of the experimental setup and (b) Illustration of straight and bent probe configurations

### 4.2.2 CFD model and simulation setup

For CFD simulations, VOF model (87, 88, 138) was employed to track vortex shape and study gas-liquid dynamics. In this model, two immiscible fluids (air and water) were modeled by solving a single set of momentum equation. The two fluids, air, and water shared same velocity and turbulence fields in the computational domain. The

volume fraction of each fluid was calculated by solving a continuity equation for one of the phases. The scalar variable  $\epsilon_g$  was assigned in each computational cell to represent volume fraction of the gas phase. In a given computational cell,  $\epsilon_g = 1$ , represented pure air and  $\epsilon_g = 0$ , represented pure water. The air-water interface was determined by identifying the cells where the volume fraction was  $0 < \epsilon_g < 1$ . Density and viscosity of fluid were calculated at each cell based on the value of  $\epsilon_g$ . The governing equations for VOF model are listed in Table-4.1.

Table-4.1: Governing equations for VOF and turbulence models
Volume fraction equation for gas phase
$\frac{\partial \epsilon_G}{\partial t} + \nabla \cdot (\vec{u} \epsilon_G) = \frac{m_G}{\rho_G}$
Volume fraction equation for liquid phase
$\frac{\partial \epsilon_L}{\partial t} + \nabla \cdot (\vec{u} \epsilon_L) = \frac{m_L}{\rho_L}$
Where
$m_G = -m_L$
Momentum equation
$\frac{\partial}{\partial t} (\rho \vec{u}) + \nabla \cdot (\rho \vec{u} \vec{u}) = -\nabla p + \nabla \cdot [\mu (\nabla \vec{u} + \nabla \vec{u}^T)] + \rho \vec{g} + F_V$
Where
$\rho = \rho_G \epsilon_G + \rho_L \epsilon_L$
$\mu = \mu_G \epsilon_G + \mu_L \epsilon_L$
Volume force
$F_V = \sigma \frac{\epsilon_G \rho_G \rho k_G \nabla \epsilon_G + \epsilon_L \rho_L \rho k_L \nabla \epsilon_L}{0.5(\rho_G + \rho_L)}$
Where, $\sigma$ = surface tension coefficient; $k$ = interface curvature
$k_G = -k_L = -\nabla \cdot \left[ \frac{\nabla \epsilon_G}{ \nabla \epsilon_G } \right]$
Courant number

$$C_o = v \cdot \left[ \frac{\Delta t}{\Delta x} \right]$$

Where,

t = time step; Δx = mesh width; v = characteristic velocity in the system

Turbulence models

Standard k-ε model

$$\frac{\partial}{\partial t} (\rho k) + \frac{\partial}{\partial x_i} (\rho k u_i) = \frac{\partial}{\partial x_j} \left[ \mu + \frac{\mu_t}{\sigma_k} + \frac{\partial k}{\partial x_j} \right] + G_k + G_b - \rho \epsilon - y_M + S_k$$

$$\frac{\partial}{\partial t} (\rho \epsilon) + \frac{\partial}{\partial x_i} (\rho \epsilon u_i) = \frac{\partial}{\partial x_j} \left[ \mu + \frac{\mu_t}{\sigma_\epsilon} + \frac{\partial \epsilon}{\partial x_j} \right] + C_{1\epsilon} \frac{\epsilon}{k} (G_k + C_{3\epsilon} G_b) - C_{2\epsilon} \frac{\rho \epsilon^2}{k} + S_\epsilon$$

Where

$$C_{1\epsilon}=1.44; C_{2\epsilon}=1.92; C_\mu=0.09; \sigma_k=1.0; \sigma_\epsilon=1.3$$

Standard k-ω model

$$\frac{\partial}{\partial t} (\rho k) + \frac{\partial}{\partial x_i} (\rho k u_i) = \frac{\partial}{\partial x_j} \left( \Gamma_k \frac{\partial k}{\partial x_j} \right) + G_k - y_k + S_k$$

$$\frac{\partial}{\partial t} (\rho \omega) + \frac{\partial}{\partial x_i} (\rho \omega u_i) = \frac{\partial}{\partial x_j} \left( \Gamma_\omega \frac{\partial \omega}{\partial x_j} \right) + G_\omega - y_\omega + S_\omega$$

Reynolds stress model

$$\begin{aligned} \frac{\partial}{\partial t} (\rho \overline{u'_i u'_j}) + \frac{\partial}{\partial x_k} (\rho u_k \overline{u'_i u'_j}) = & - \frac{\partial}{\partial x_k} \left[ \rho \overline{u'_i u'_j u'_k} + \overline{\rho (\delta_{kj} u'_i + \delta_{ik} u'_j)} \right] + \\ \frac{\partial}{\partial x_k} \left( \mu \frac{\partial}{\partial x_k} \rho \overline{u'_i u'_j} \right) - \rho \left( \overline{u'_i u'_k} \frac{\partial u_j}{\partial x_k} + \overline{u'_j u'_k} \frac{\partial u_i}{\partial x_k} \right) - \rho \beta (g_i \overline{u'_j \theta} + g_j \overline{u'_i \theta})] + \\ \rho \left( \frac{\partial \overline{u'_i u'_j}}{\partial x_j} + \frac{\partial \overline{u'_j u'_i}}{\partial x_i} \right) - 2 \mu \frac{\partial \overline{u'_i u'_j}}{\partial x_k \partial x_k} \end{aligned}$$

(i)
(ii)
(iii)

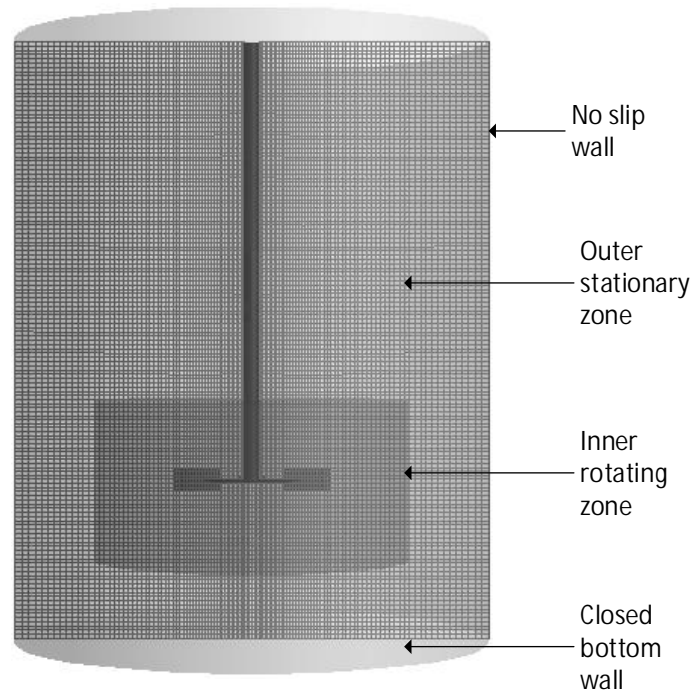


Figure-4.2: Computational domain and grid distribution

Three-dimensional transient simulations were carried out using Fluent 18 (Ansys inc). Hexahedral mesh (with aspect ratio  $\sim 1$ ) was used to discretise the flow domain (Figure-4.2). Rotating disc turbine was modelled using multiple reference frame (MRF) approach where a region comprising of impeller and shaft was assigned as an inner rotating zone (Figure-4.2). This zone was rotated with an angular velocity equal to impeller speed. Dimensions of this zone were 0.08 m radius, and 0.08 m height covering the axial distance between 0.04 and 0.12 m from the bottom. A portion of shaft outside the rotating zone was considered as a moving wall rotating at speed equal to impeller speed. Apart from inner rotating zone and shaft, rest of the flow domain was considered as a stationary zone. All the walls were assigned with no-slip condition. Each simulation was started with the initial liquid holdup of 0.24 m from tank bottom ( $H_L = T$ ), and remaining height was filled with air. A constant surface tension coefficient of 0.072 N/m was used. The QUICK scheme was employed to discretise volume fraction equation, whereas second-order upwind scheme was used for momentum equation. It was observed that there was no change in vortex depth for the tested impeller speeds after 15 seconds simulation time. Therefore, all simulations were carried out for 15 seconds using variable time step method ensuring the global courant number of 0.25.

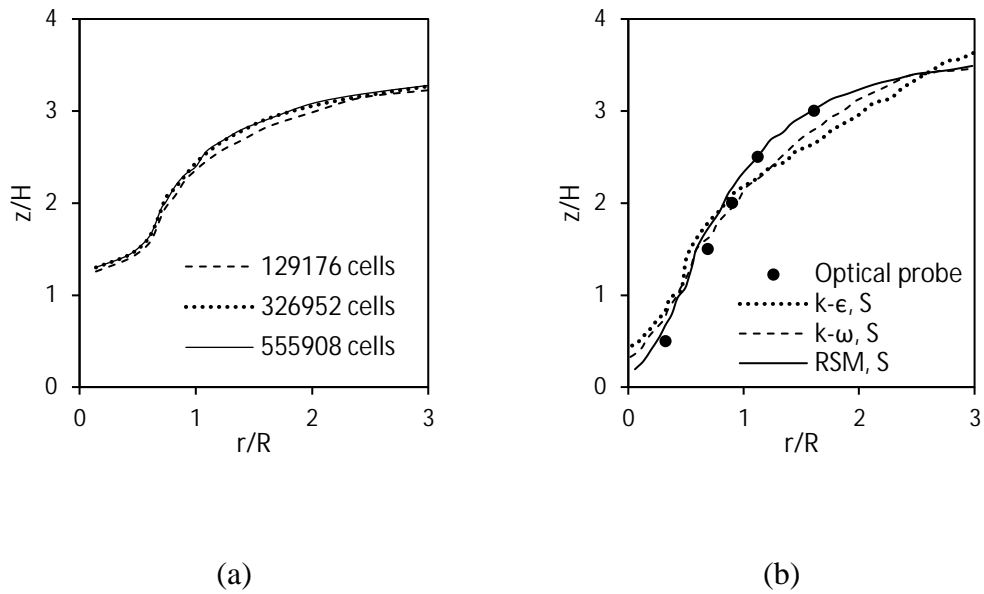


Figure-4.3: (a) Grid independency test ( $N = 500$  rpm) and (b) comparison of turbulence models ( $N = 800$  rpm) with optical probe measurements

Grid independency was tested by performing simulations with coarse (129176), fine (326952) and very fine (555908) mesh (Figure-4.3a). Quantitative predictions of vortex coordinates from the fine and very fine mesh were close; therefore, the fine mesh was employed for all subsequent simulations. Researchers have compared various turbulence models earlier to predict the vortex shape but only without vortex ingestion. Mahmud et al., (87) reported that predictions from Reynolds Stress Model (RSM) captured vortex shape more accurately compared to other turbulence models. The present study investigates the effect of vortex shape with ingestion and hence preliminary simulations were performed to verify the effect of vortex ingestion on turbulence models. Three turbulence models (k- $\epsilon$ , k- $\omega$ , and Reynolds Stress Model – Table-4.1) were used in simulations and the results were compared with optical probe measurements (Figure-4.3b). Investigation of turbulence models revealed that k- $\epsilon$  and k- $\omega$  models provided similar results, with their predictions deviating from experimental results in the majority of the tank. Better predictions were obtained using RSM where the simulation results were consistent with optical probe measurements from  $r/R = 1.2$ , while the predictions near impeller blades shown minor discrepancies. The reason for improved predictions by RSM can be attributed to its ability to solve transport equations for Reynolds stress directly. Therefore, experimentally verified

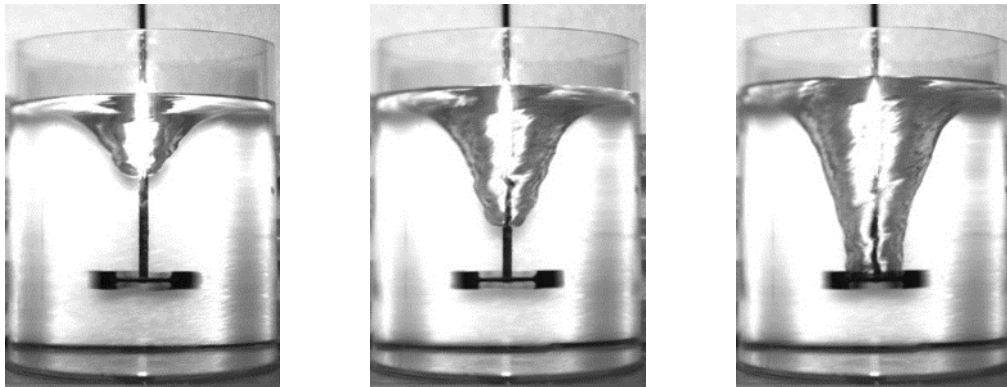


RSM model was used to simulate the flow and to track interface and the results were discussed in the following sections.

### 4.3 RESULTS AND DISCUSSION

#### 4.3.1 Vortex shape

The effect of impeller speed on vortex shape is qualitatively shown in Figure-4 using instantaneous photographs. Up to 500 rpm (Figure-4.4a), vortex depth remained above impeller. At 600 rpm (Figure-4.4b), the vortex came in contact with impeller leading to gas dispersion inside the tank. The dispersed gas bubbles were initially thrown towards tank wall, and seen circulating in vortex core. Further increase in impeller speed increased the vortex depth, and higher gas dispersion was observed. The increase in speed intensified blade to bubble contact followed by increased bubble shredding which caused high bubble density around impeller region. At 800 rpm, the vortex made contact with tank bottom resulting in deformation of the liquid surface below impeller and thus causing torque instability.



300 rpm

400 rpm

500 rpm

(a)

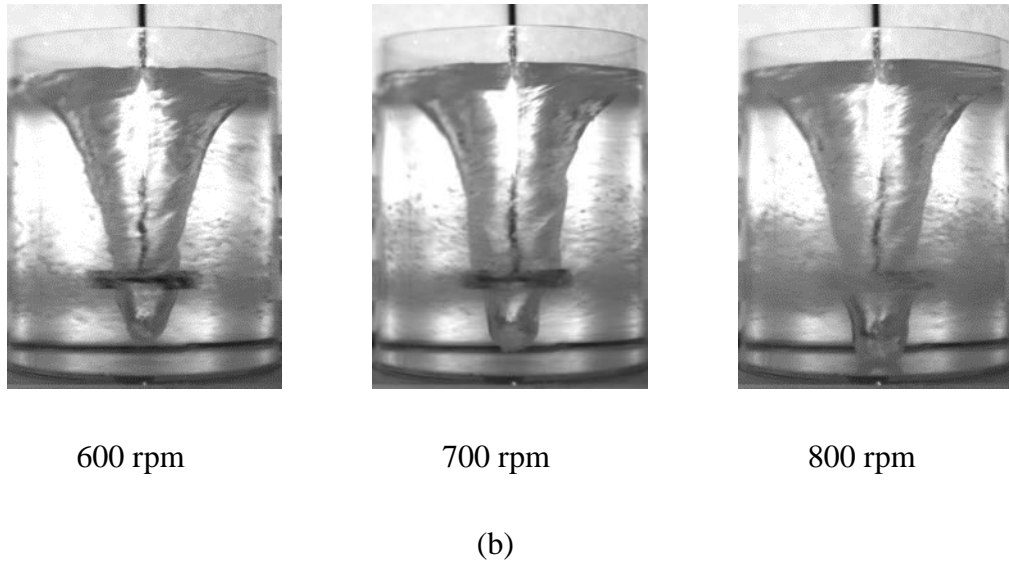
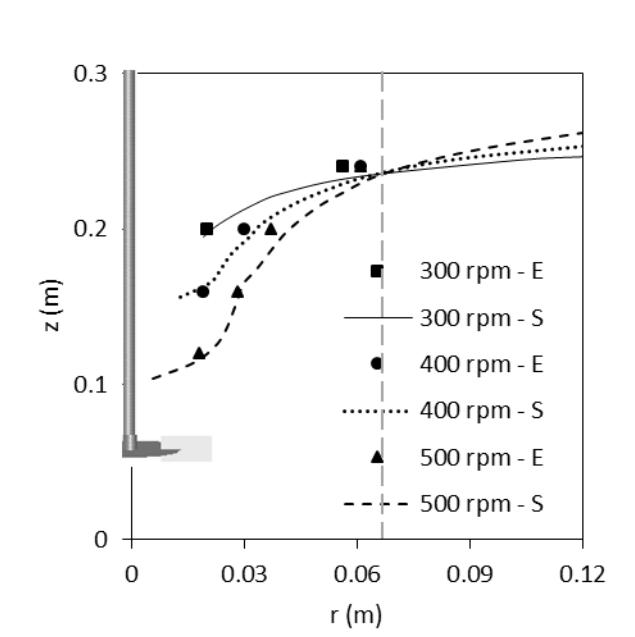
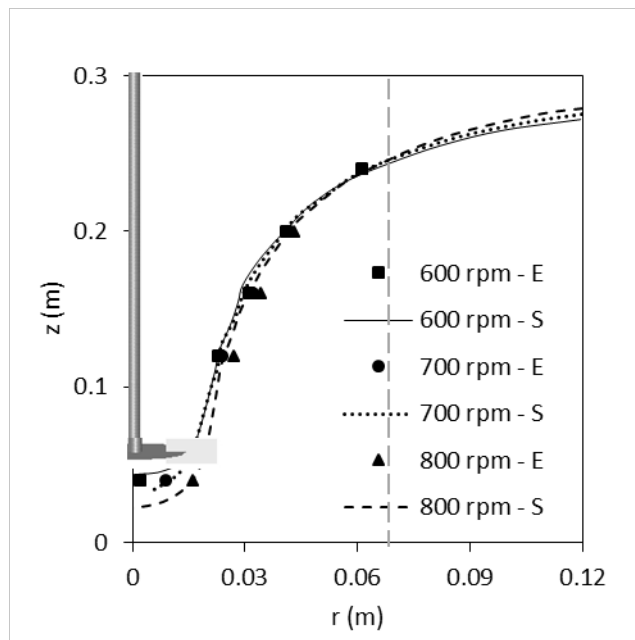


Figure-4.4: Instantaneous photographs of vortex shape (a) without vortex ingestion and (b) with vortex ingestion

Quantitative data on vortex shape at varying impeller speed is shown in Figure-4.5, which consists of both experimental data, and simulation results. Figure 4.5(a) indicates, prior to vortex ingestion, the vortex shape was strongly influenced by impeller speed. The change in vortex shape was more pronounced near the shaft as compared with the wall. As the distance between the free surface and impeller increased, the oscillatory motion of gas-liquid interface reduced. The vertical line at  $r = 0.07$  m in Figure-4.5(a) indicates that the vortex shape can be distinguished into two zones based on the variation in the interface. With an increase in impeller speed, for zone-1 ( $r = 0$  to  $0.07$  m), water level decreased while the water level increased for zone-2 ( $r > 0.07$  m). Especially when impeller speed was increased from 300 to 500 rpm water level near the shaft dropped down by 0.1 m, whereas it increased by 0.015 m near the wall. On the contrary, with vortex ingestion, the influence of impeller speed on vortex shape was less pronounced (Figure-4.5b). When the vortex came in contact with the rotating internals, most of the energy dissipated from the impeller blades was consumed for dispersing gas rather than deformation of the vortex structure. In this case, above the impeller, variation in vortex shape with speed was negligible ( $r = 0.03$  to  $0.09$  m) whereas a minimal variation in vortex depth was observed below the impeller.



(a)



(b)

Figure-4.5: Effect of impeller speed on vortex shape (a) without vortex ingestion; (b) with vortex ingestion

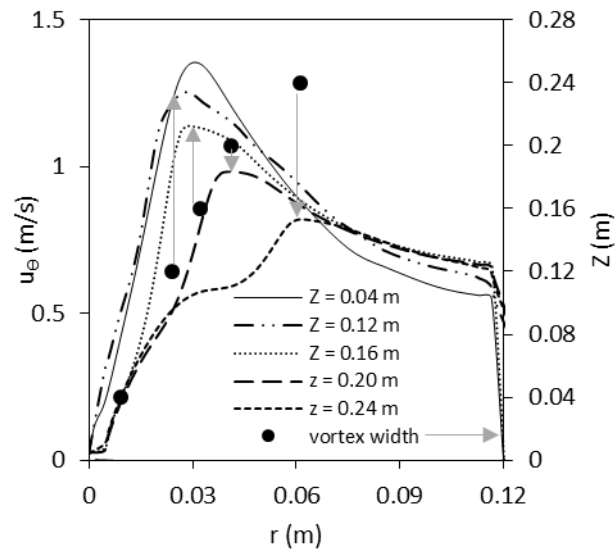
Good agreement was observed between experimental and simulations results in middle section of the tank. However, near tank bottom, a small discrepancy of 2% was observed. Particularly, instantaneous photograph at 800 rpm (Figure-4.5b) indicated

that vortex depth reached tank bottom whereas simulation results showed the depth was 0.02 m above tank bottom.

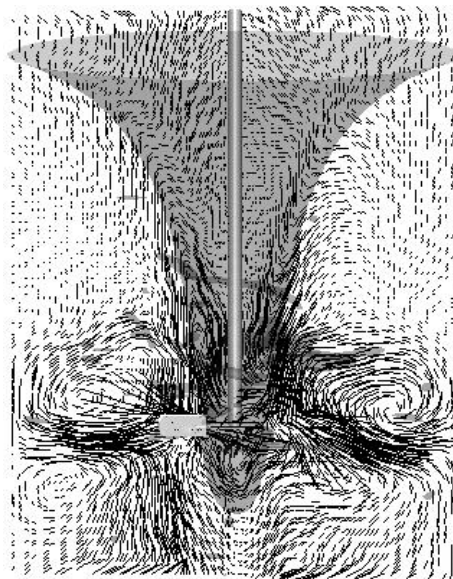
#### **4.3.2 Gas-liquid velocity distribution**

Simulation results at 700 rpm were analyzed to understand velocity field along the vortex. Time-averaged tangential velocity profiles (primary y-axis) and vortex width (secondary y-axis) at five axial locations along the vortex depth and 700 rpm are shown in Figure-4.6(a). In the Figure, solid black markers represents the vortex width obtained from optical probe measurements and the gray arrows indicates the peak of tangential velocity profile at different axial locations corresponding to vortex width. The velocity profiles clearly indicates that, except for one below the impeller ( $z = 0.04$  m) are highly conformal to the vortex width. This indicates that above impeller, tangential velocity distribution governed the shape of the vortex and its free surface movement. At all axial locations, the tangential velocity increased linearly to reach a maximum value at vortex interface, and then gradually decreased towards tank wall. The variation in the tangential velocity values corresponded to the differences in gas and liquid phase velocity. The tangential velocity peak was higher at  $z = 0.04$  m (below impeller) followed by  $z = 0.12$  m (above impeller) indicating that the vortex was subjected to greater tangential forces around the impeller. The reason for high tangential forces could be attributed to the existence of recirculation zones around the impeller as shown in Figure-4.6(b). It must be noted that the differences in the velocity patterns in these two zones strongly influenced the vortex shape near impeller. Deshpande et al., (86) observed that the tangential velocity was independent of axial distance when the vortex was above impeller (without vortex ingestion). But the present study demonstrated that with vortex ingestion the tangential velocity reduced with an increase in axial height from the impeller. Axial and radial velocity profiles at the different axial positions are shown in Figure-4.6(c) and (d). It is anticipated that the axial and radial components of velocity are significantly lower than that of the tangential component (82, 86, 139), and simulation results of the axial and radial velocity distributions also confirm the hypothesis. However, it could be seen that the impeller generated significantly higher axial and radial flow at  $z = 0.12$  m (above impeller) followed by  $Z = 0.04$  m (below impeller). This was in contrary to tangential velocity profiles where maximum tangential velocity was observed below impeller. Especially, the radial component at  $z = 0.12$  m was close to 30% of the peak tangential

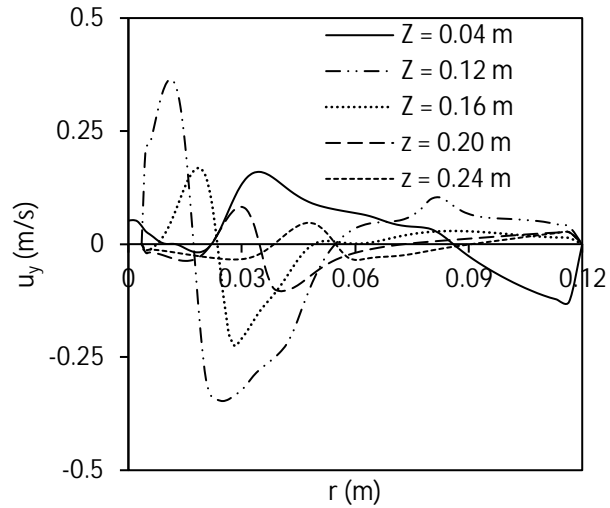
velocity component. This could be attributed to the variation in the size of recirculation zones above and below impeller as shown in Figure-4.6(b).



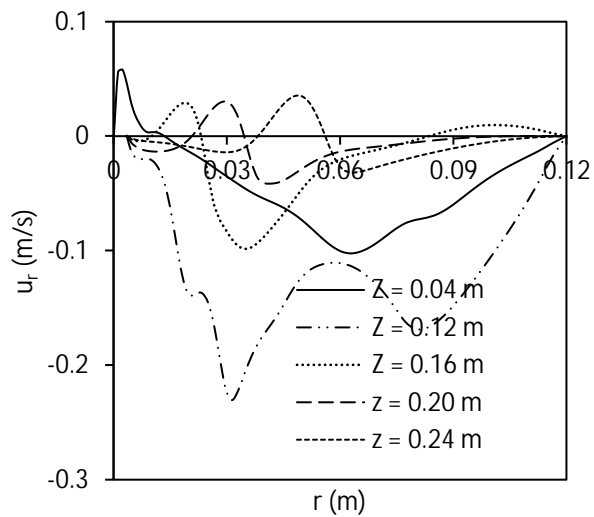
(a) Tangential velocity distribution



(b) Velocity magnitude vectors



(c) Axial velocity distribution



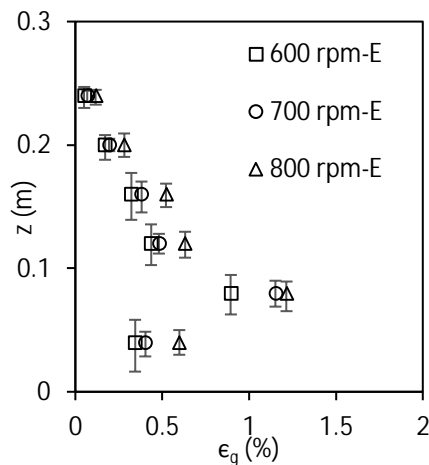
(d) Radial velocity distribution

Figure-4.6: Velocity profiles at different axial heights (N = 700 rpm)

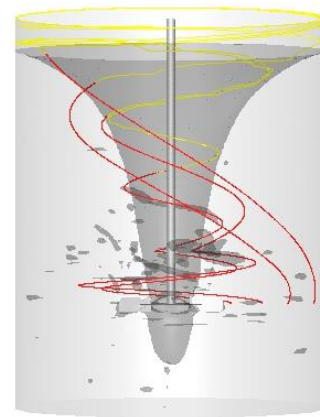
### 4.3.3 Local gas holdup and bubble chord length distribution

The influence of impeller speed on cross-sectional gas holdup  $\left( \epsilon_g = \frac{\int_0^R 2\pi r \epsilon_g dr}{\int_0^R 2\pi r} \right)$  (56), at six axial locations is shown in Figure-4.7(a). The gas holdup profiles resembled a convex shape with a peak value at impeller plane ( $z = 0.08$  m). At all the three impeller speeds studied, the gas induced due to vortex ingestion concentrated around the

impeller (See Figure-4.4b). The maximum gas holdup of 1.2% was recorded at  $z = 0.08\text{m}$ , and 800 rpm. It was observed that gas holdup calculated from optical probe measurements were almost 40% underpredicted by simulations and hence the CFD results were not shown here. The discrepancy between experimental data and simulation results can be attributed to two factors, (i) as shown in Figure-4.7(b), the gas bubbles were generated around the impeller region where the optical probe could not be placed, and (ii) the CFD model was unable to capture bubble breakup or coalescence that governed gas holdup throughout the tank. It was observed that the gas holdup was lower at top axial locations ( $z = 0.24$  and  $0.20\text{ m}$ ) as most of the bubbles escaped out of vortex core even before reaching the top liquid free surface. This observation was supported by demonstrating the path lines (coloured by phases) for a single bubble of 1.75 mm released from four radial locations at impeller plane ( $z = 0.08\text{ m}$ ) at  $t = 15\text{ s}$  and  $N = 700\text{ rpm}$  (Figure-4.7b). The trajectory of the bubbles indicated where the gas bubbles entrained into the free surface. It can be seen from Figure-4.7(b) that the bubbles near impeller blades ( $r = 0.04$  and  $0.07\text{ m}$ ) initially spun around the interface and rose following the vortex structure. These bubbles entrained into the vortex core before reaching the top surface of the tank. On the other hand, the bubbles released near tank wall ( $r = 0.09$  and  $0.11\text{ m}$ ) reached the top surface without escaping through the vortex.



(a)



(b)

Figure-4.7: (a) Axial profiles of gas holdup and (b) path lines (coloured by phases: red-water; yellow-air) of bubbles released from impeller plane

The time-average chord length of bubbles at three impeller speeds as measured by the optical probe is shown in Figure-4.8(a). It is expected that an increase in impeller speed reduces the bubble size in baffled stirred tanks (14, 16). It was found that, this phenomenon held good only at impeller plane ( $z = 0.08$  m) and below impeller plane ( $z = 0.04$  m) for the unbaffled tank. The absence of baffles in the unbaffled tank promoted bubble coalescence resulting in larger bubbles above the impeller plane. Figure-4.8(b) shows the chord length distribution at impeller plane ( $Z = 0.08$  m) as a function of bubble count. At all impeller speeds, approximately 50% of the total bubble population (3000) had a chord length less than 0.5 mm. A wide distribution of chord length was observed at 600 rpm. At this impeller speed, a significant number of large bubbles had chord length varying from 0.5 to 5 mm. At 700 rpm, the distribution became narrower with values varying between 0 to 3 mm. At 800 rpm, unimodal distribution with a peak bubble count at  $\sim 0.5$  mm was found. At this impeller speed, no bubble had a chord length above 2.2 mm. The bubble count of the smaller bubbles ( $< 0.5$  mm) was increased by twofold when the speed was increased from 600 to 800 rpm. This could be attributed to the increase in shear with impeller speed that led to enhanced bubble break up and generation of the finer bubbles.

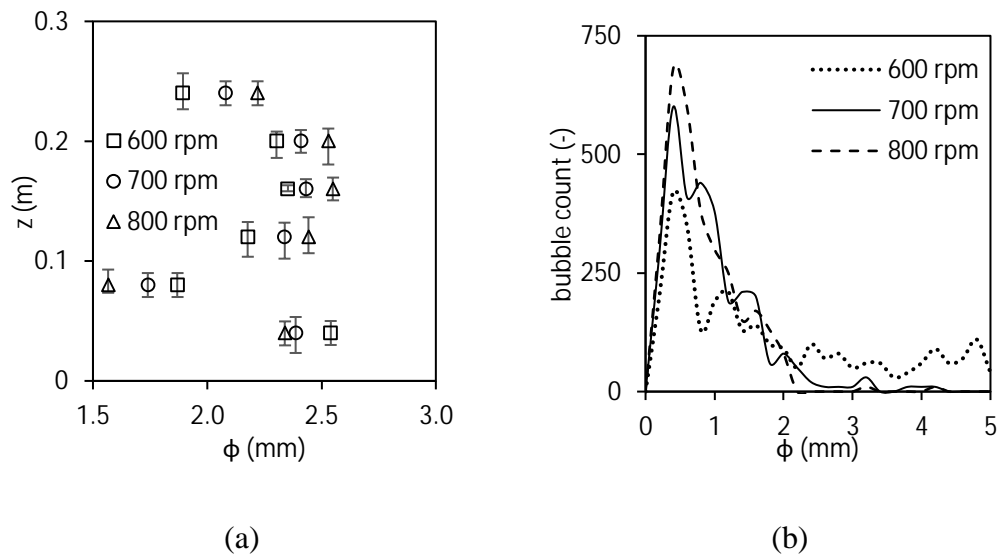


Figure-4.8: (a) Axial profiles of chord length and (b) chord length distribution at impeller plane ( $z = 0.08$  m)



#### 4.4 SUMMARY

In this chapter, the performance of optical probe to measure local bubble hydrodynamics in stirred tanks was evaluated by investigation of vortex ingestion in a 0.24 m unbaffled stirred tank equipped with four bladed disc turbine. In addition, VOF simulations were conducted to gain more insights on the effect of vortex ingestion on gas-liquid velocity distribution. For experiments, straight, and bent optical probes were employed to measure local gas holdup and chord length distribution of the bubbles. In simulations, VOF model in conjunction with multiple reference frame model and Reynolds stress turbulence model was used. It was observed that with vortex ingestion the influence of impeller speed on vortex shape was less pronounced. Tangential velocity profiles at all axial locations, except for one below the impeller ( $z = 0.04$  m) were highly conformal to vortex width indicating above impeller, tangential velocity distribution governs the shape of vortex and its free surface movement. It was found that, impeller generated significantly higher axial and radial flow at  $Z = 0.12$  m (above impeller) followed by  $z = 0.04$  m (below impeller). Especially, radial component at  $z = 0.12$  m was close to 30% of peak tangential velocity component due to the presence of recirculation loops above and below impeller. Gas holdup calculated from optical probe measurements were almost 40% under predicted by simulations. Such under-predictions were owing to the limitations such as placing an optical probe near rotating impeller was not feasible and VOF model was unable to capture bubble breakup or coalescence that governed gas holdup throughout the tank. At 800 rpm, maximum gas holdup of 1.2% was recorded at  $z = 0.08$  m. It was found that most of the bubbles escaped out of vortex core even before reaching the top free surface that led to lower gas holdup at top axial locations ( $z = 0.24$  and  $0.20$  m). The absence of baffles in the unbaffled tank promoted bubble coalescence that resulted in larger bubbles with increase in impeller speed. At all impeller speeds, approximately 50% of the total bubble population (3000) had a chord length less than 0.5 mm. The data presented in this chapter will help to improve the level of information on hydrodynamics of self-ingesting unbaffled tanks, allowing a better assessment and their application potential.

## Chapter 5

### Local bubble hydrodynamics in baffled stirred tanks

#### 5.1 INTRODUCTION

In previous chapters, it was established that the optical probe could be successfully employed in bubble column, and unbaffled stirred tank to capture the local bubble hydrodynamics, particle velocities, and vortex shape. These systems are less commonly encountered in industries for gas dispersion applications mostly due to unidirectional flow pattern and less turbulence compared to baffled stirred tanks. Therefore, the local bubble hydrodynamics in baffled tanks was investigated. Such study could provide a better understanding of the effect of operating conditions, impeller geometry and solid loading on gas phase hydrodynamics in industrial reactors. In this chapter, two gas dispersion impellers namely SRT and HSPBT are experimentally studied by optical probe and strain gauge measurements.

Extensive experiments have been carried out over the years in either gas-liquid stirred tanks (GL-ST), or solid-liquid stirred tanks (SL-ST) fitted with SRTs in both lab and industrial scale (4, 11, 15, 60). These studies were mostly focused on global or local bubble dynamics in GL-STs, or solid/liquid phase velocities in case of SL-STs (10, 12, 61, 62, 140, 141). Due to limitations on the measurement techniques (57), simultaneous measurements of two or more phases in a gas-liquid-solid stirred tank (GLS-ST) were not reported. In addition to solid loading, impeller size also influences the gas phase hydrodynamics to a great extent. Rushton turbines (RTs) with different impeller size apart from the conventionally used 0.33 D/T (impeller diameter/tank diameter) are of greater usefulness in different applications. Normally, the D/T of RT for a given application is selected based on viscosity of the liquid phase, gas handling capacity, pumping efficiency and power consumption. For instance, impellers with D/T of 0.25 to 0.3 with high rotational speed are preferred in bioreactors; whereas larger D/T of 0.4-0.7 are used to increase the pumping efficiency in highly viscous systems. Local bubble hydrodynamics of such impellers cannot be quantified by using widely published data for the standard D/T (0.33) SRTs. Moreover, power consumption cost, manufacturing and operational cost of gear box assembly and motor

depends on the selection of impeller diameter. Thus, investigation on the effect of RT's D/T on local bubble hydrodynamics is important. There exist only limited studies focussing on the influence of D/T on hydrodynamics.

Kumaresan et al., (142) have reported the effect of different impeller designs, including the effect of D/T on flow pattern and power number but not on gas dispersion. Saravanan et al., (58) have showed the impact of D/T on gas holdup for different impeller combinations with pitched blade turbines (PBT) and gas-inducing impellers. Saravanan et al., (58) have observed the gas holdup by the change in the initial height of liquid due to gas sparging. Such visual measurements lack precision compared to the advanced measurement techniques, and it does not provide any information on bubble size and velocity. Recently, Bao et al., (26, 67) have reported the influence of the D/T on global and local gas holdup and bubble size using conductivity probe. They used a multi-impeller assembly, where the shaft is mounted with a parabolic blade disc turbine at the bottom and two hydrofoils on top. The reported data is further limited to the minimum bubble size of 3 mm due to the size of the probe tip. Literature review shows that most of the previous studies focused on the impact of D/T in gas-liquid stirred tanks have been carried out using the PBT or multi-impeller assembly whose flow pattern and hydrodynamics are different from the RT.

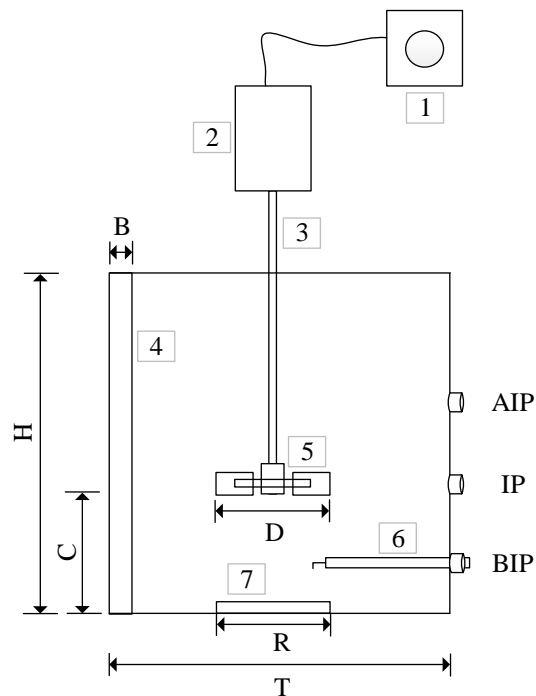
For gas dispersion and solid suspension in mineral processing applications, axial down pumping impellers such as pitched blade turbines (PBT) are commonly used. Standard PBT is suitable for handling low gas volumes. At high gas dispersion, it suffers from low down pumping efficiencies and high torque instability. To improve gas handling capacity of PBT, high solidity pitched blade turbine (HSPBT) has been developed (39, 40). Review of the experimental studies on GL-ST presented in chapter-2: Table-2.2 revealed that majority of the studies had been conducted using either SRTs or low solidity PBTs. Also, most of the previous studies using PBTs have been conducted with a fixed blade angle of 45°. Vital data on HSPBT and the effect of blade angle is not available in open literature.

To summarize, the effect of solid loading and impeller diameter of SRT on local hydrodynamics is yet to be reported. Also information on effect of HSPBT's blade angle is not available in open literature. Therefore, the current chapter reports findings on the SRT, RT and HSPBT using optical probe and strain gauge measurements. Since the operating conditions were selected based on completely dispersed flow regime,

experimented conditions varied between SRT, RT, and HSPBT. Therefore, for the ease of understanding the experimental setup and results & discussion sections of this chapter are organized in three parts. 1. Effect of solid loading on hydrodynamics in GLS-ST fitted with SRT; 2. Effect of impeller diameter and operating conditions on bubble hydrodynamics and power consumption in GL-ST with RT and 3. Effect of blade angle on gas phase hydrodynamics and power consumption in GL-ST equipped with HSPBT.

## 5.2 EXPERIMENTAL SETUP & OPERATING CONDITIONS

### 5.2.1 GLS-ST with SRT



$$H = T; C = 0.33T; D = R = 0.36T; B = 0.12T$$

- 1.Variable speed drive; 2.Motor; 3.Shaft; 4.Baffle;  
5.Rushton turbine; 6.Optical probe; 7.Ring sparger

Figure-5.1: Schematic diagram and geometrical configuration of the experimental setup

A schematic of the experimented tank with dimensions and measurement positions are shown in Figure-5.1. The stirred tank was a flat-bottomed acrylic tank ( $T = 0.45$  m) with three baffles located at  $120^\circ$  from one another. Impeller assembly consisted of

0.16 m diameter, six bladed (0.003 m thick) SRT mounted to a shaft. Tap water was used as liquid phase, while compressed air was used as gas phase. Slurry consisted of 1% of fine weight sand with an average particle diameter of 350  $\mu\text{m}$  was considered as a solid phase. For injection of compressed air, a ring sparger made up of a copper tube with 18 holes of 2 mm diameter was placed at the bottom of the tank. Impeller speed was controlled by a variable speed drive while gas flowrate was adjusted using an inlet valve and rotameter. Experiments were carried out at completely dispersed regime with Flow numbers (Fl) in the range of 0.07 to 0.09 and Froude numbers (Fr) from 0.57 to 0.83 that corresponds to the gas flow rate (Q) of 0.0021  $\text{m}^3/\text{s}$  and impeller speed (N) of 5.9 to 7.15 rps respectively. Optical probe was mounted on the tank wall through a probe provision at three different axial heights (Y) of 0.05 (below impeller plane: BIP), 0.15 (impeller plane: IP) and 0.25 m (above impeller plane: AIP) from the bottom. Radial measurements were taken at five radial positions (r) at AIP and BIP at  $r = 0.03, 0.07, 0.11, 0.15,$  and  $0.19$  and 3 radial positions of  $r = 0.11, 0.15$  and  $0.19$  m at IP as shown in the Figure-5.1.

### 5.2.2 GL-ST with RT

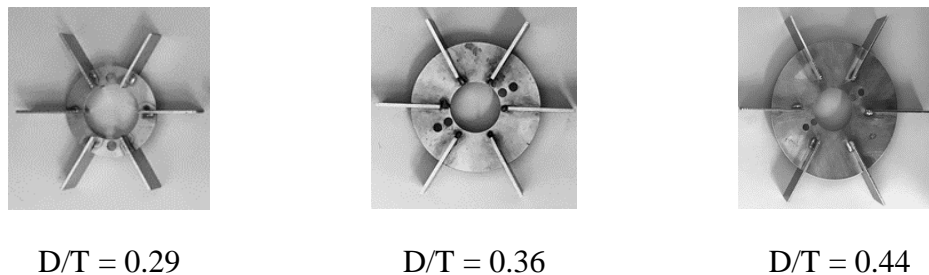
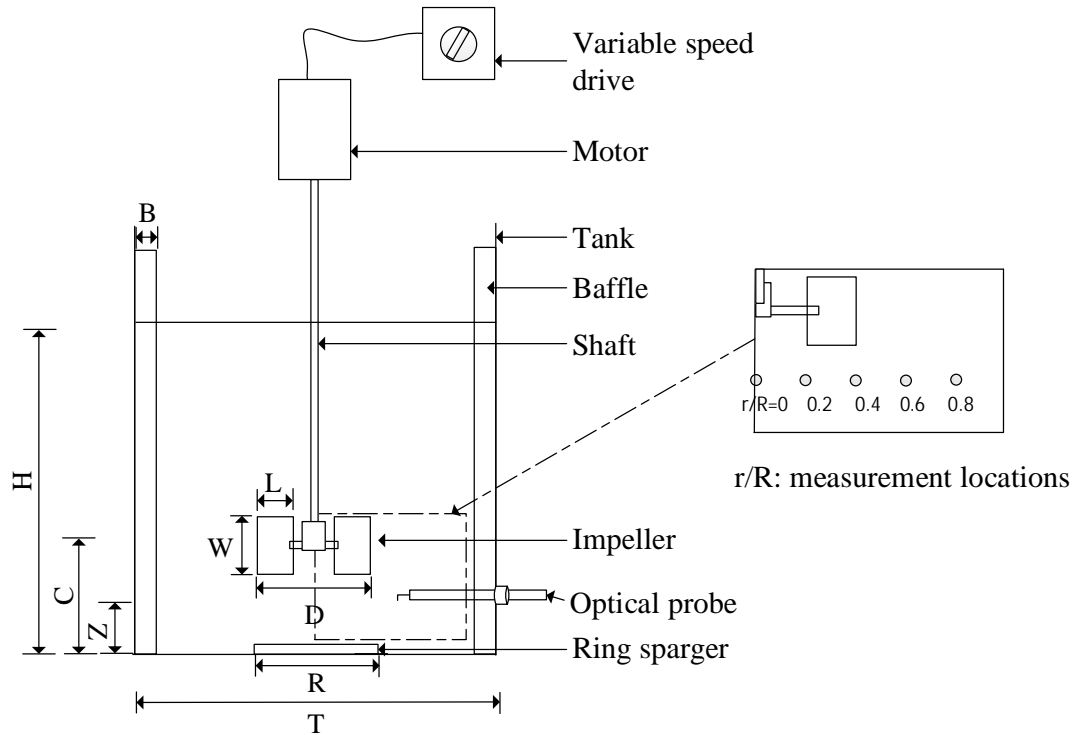


Figure-5.2: RTs used in this study

Effect of impeller diameter and operating conditions on gas dispersion and power consumption were investigated in GL-ST experiments. For these experiments, RTs (blade dimensions:  $w = D/6$  and  $l_b = D/3$ ) with three different D/T's were used in this work as shown in Figure-5.2. Tank dimensions, baffles, variable speed drive, ring sparger, liquid, and gas phase remained same as discussed in Section 5.2.1. Experiments were performed by varying impeller speed from 0.8 m/s to 4.8 m/s, and superficial gas velocity ranges from 0.0078 to 0.0210 m/s at completely dispersed flow regime (15). It was suggested by Lee et al., and Mueller et al., (15, 143), to study bubble dynamics in a stirred tank fitted with radial impellers, positioning the probe at

impeller discharge plane with the probe tip facing inward was sufficient to characterize the gas dispersion phenomena for the entire tank. Thus, measurements were taken at impeller discharge plane at the mid-point (half of the distance between the tank wall and impeller blade tip) for all experiments.

### 5.2.3 GL-ST with HSPBT



$$T = 0.45 \text{ m}; H = T; C = 0.33T; D = 0.36T; R = 0.36T;$$

$$B = 0.12T; L = 0.32D; W = 0.5D; Z = 0.5C$$

Figure-5.3 (a): Schematic diagram and geometrical configuration



HSPBT 30°



HSPBT 45°



HSPBT 60°

Figure-5.3 (b): HSPBTs used in this study

A schematic of the experimented tank with dimensions and measurement positions is shown in Figure-5.3. Impeller assembly consisted of HSPBT with four blades (0.003 m thick and 0.08 m wide) bolted to an impeller hub which was mounted to a shaft. Experiments were carried out at five superficial gas velocities from 0.008 to 0.018 m/s; five impeller speeds from 425 to 525 rpm; and three blade angles of 30°, 45°, and 60°. Power dissipation and overall gas holdup in the tank were measured using a strain gauge mounted on the shaft and using stand still level measurement tube. Optical probe measurements for the three different blade angles were taken only at a fixed superficial gas velocity of 0.013 m/s and an impeller speed of 425 rpm. The optical probe was mounted on the tank wall through a probe provision at axial height of 0.5C from the bottom. The measurements were taken at five radial positions denoted by  $r/R = 0, 0.2, 0.4, 0.6,$  and  $0.8$  as shown in the inset of Figure-5.3.

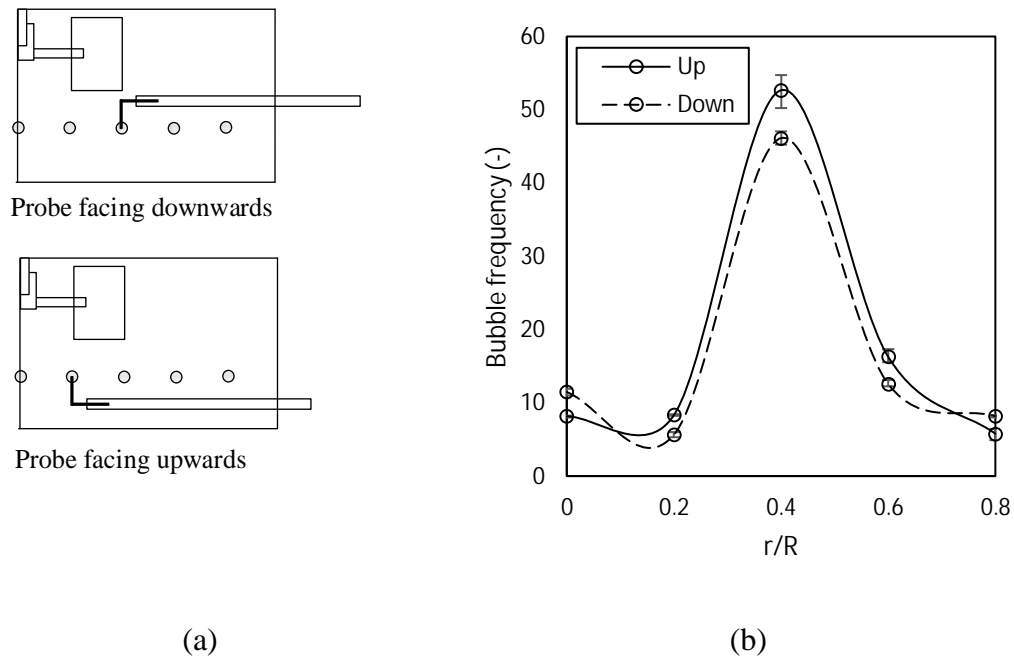


Figure-5.4: (a) Probe tip facing upwards and downwards and (b) Effect of probe orientation on local gas holdup [HSPBT30°;  $N = 425$  rpm ;  $u_g = 0.013$  m/s ]

The flow in stirred tanks is not unidirectional which could pose difficulties in maintaining probe orientation opposite to flow direction. Therefore, it is critical to account for errors caused by probe orientation. Mueller et al., (48) have suggested the use of minimum two probe orientations facing upwards and downwards as shown in Figure-5.4(a) to minimize probe orientation errors. For HSPBT30° at 425 rpm, the influence of probe orientation positions on bubble count is shown in Figure-5.4(b).

Near the impeller region ( $r/R = 0.2, 0.4$  and  $0.6$ ) probe encountered more bubbles when the tip was facing upwards, whereas near the tank wall ( $r/R = 0.8$ ) and tank centre ( $r/R = 0$ ), high bubble frequency was recorded by facing the probe tip downwards. Similarly, for all SRT and HSPBT experiments, measurements were taken with two probe orientations, and only higher bubble frequency values were reported as they represent a higher number of valid bubbles.

## **5.3 RESULTS AND DISCUSSIONS**

### **5.3.1 GLS-ST with SRT**

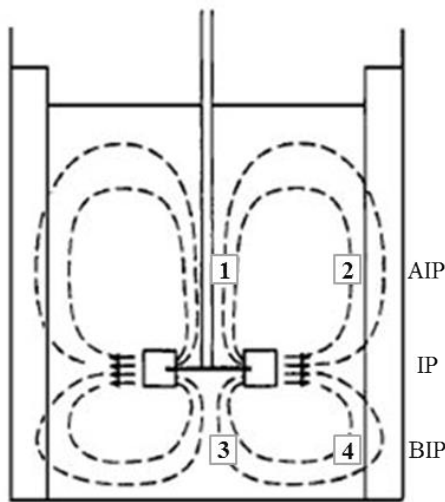
Preliminary studies were carried out in GL-ST fitted with SRT where the effect of impeller speed on local bubble dynamics was analysed. GL-ST experiments were followed by GLS-ST experiments were simultaneous measurements on gas holdup, bubble size distribution, and particle and bubble velocity distribution were carried out to understand the impact of solid loading.

#### **Local bubble hydrodynamics in GL-ST**

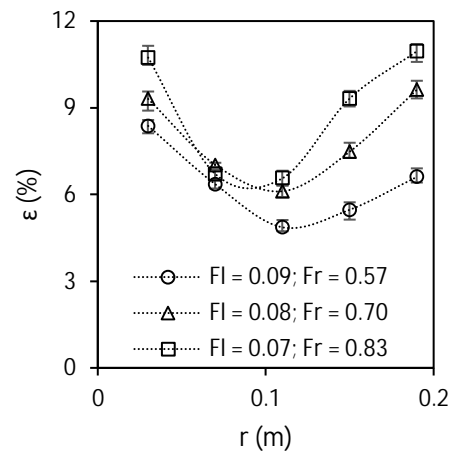
The flow pattern of gas bubble inside a stirred tank is predominantly dictated by liquid recirculation loop generated by an impeller (Figure-5.5a). In case of SRT, liquid discharged from impeller along with gas bubbles were thrown radially outward towards tank wall at the impeller plane (IP). When fluid came in contact with tank wall, it formed two recirculation loops: one above impeller plane (AIP) and one below impeller plane (BIP). The highlighted points 1, 2 (AIP) and 3, 4 (BIP) in Figure-5.5(a) represents the optical probe measurement locations ( $r$ ) of  $0.03$  m and  $0.19$  m respectively. Radial variation of a time-averaged gas holdup at AIP is shown in Figure-5.5(b). It was evident from the figure that gas holdup is high at two extreme radial locations at all operating conditions ( $Fr$  and  $Fl$  numbers). The reason could be attributed to the presence of recirculation loops (Figure-5.5a) which carried back more gas bubbles to the impeller along the shaft wall ( $r = 0.03$  m) and carried bubbles axially upward near tank wall ( $r = 0.19$  m). Due to the same reason, variation in radial gas holdup exhibited a U-shaped profile, where holdup decreased from shaft to centre of the tank and increased back towards the wall. Gas holdup values at IP were found to be higher than those in AIP and BIP (Figure-5.5c). Since the shear applied to gas bubbles was relatively higher at regions close to the impeller, the higher gas holdup was observed at IP. The observation of high holdup near impeller and the reduction in



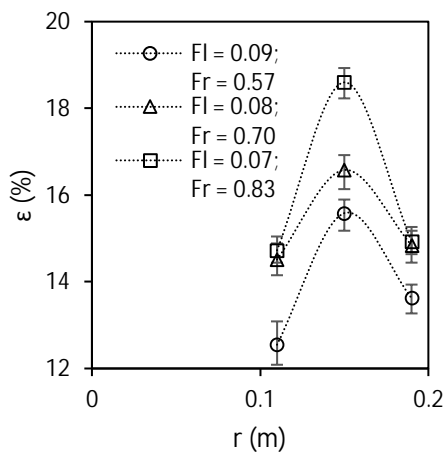
holdup away from impeller was reported by several researchers (1, 4, 49, 56, 59). Maximum gas holdup of 19% was observed at  $r = 0.15$  m at  $Fr = 0.83$ . Almost no variation in holdup was found near impeller blades and tank wall when  $Fr$  was increased from 0.70 to 0.83. Figure-5.5(d) illustrates, near sparger (r = 0.07 and 0.11 m), the gas holdup was lower (below 4%), and there is no appreciable change in gas holdup values with respect to  $Fr$ . The reason could be attributed to the fast rising gas bubbles emerging out of ring sparger positioned below these radial locations.



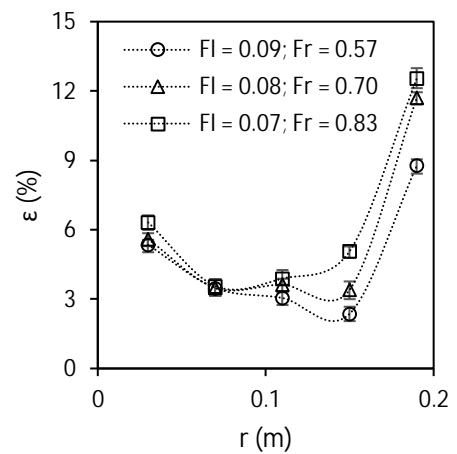
(a)



(b) AIP (Y = 0.25 m)



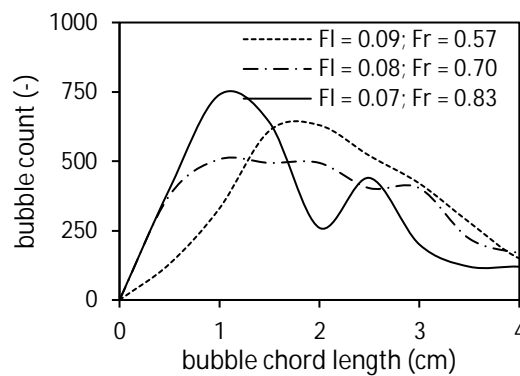
(c) IP (Y = 0.15 m)



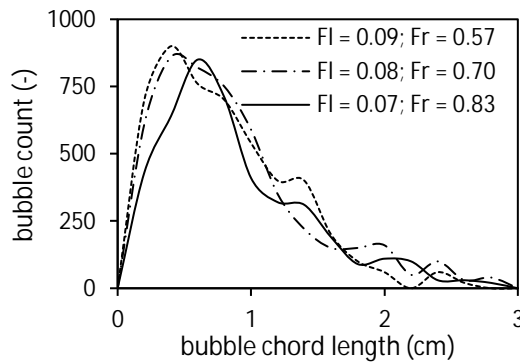
(d) BIP (Y = 0.05 m)

Figure-5.5: (a) Flow pattern in stirred tank equipped with SRT and (b-d) radial profiles of time-averaged gas holdup

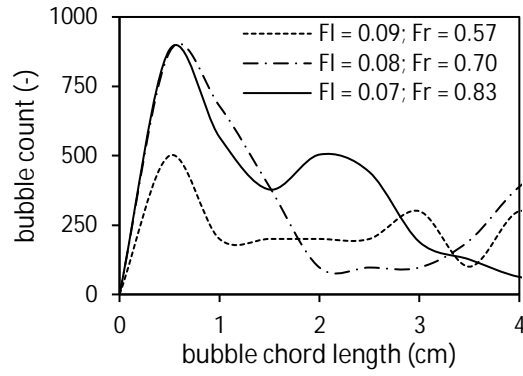
SRT used in present study was a radial impeller which discharged gas bubbles towards tank wall (IP) rather than pumping it down. Consequently, gas velocity from sparger dominated the liquid velocity generated by SRT at BIP. Hence, fast rising gas bubbles from sparger spent less time on the probe tip which led to a reduction in bubble residence time causing lower gas holdup. However, near tank wall, gas holdup increased to 13%.



(a) AIP ( $Y = 0.25$  m)

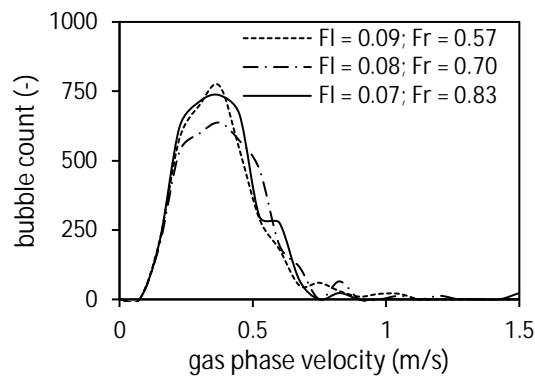


(b) IP ( $Y = 0.15$  m)

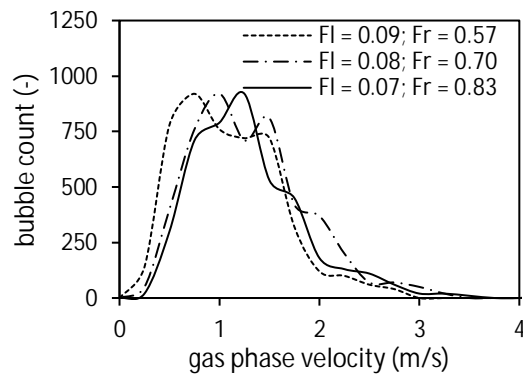


(c) BIP ( $Y = 0.05$  m)

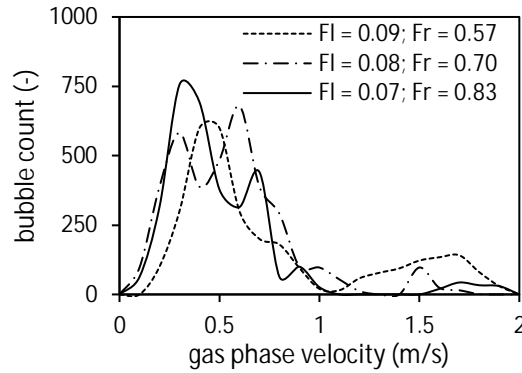
Figure-5.6: Distribution of bubble chord length at various axial locations



(a) AIP ( $Y = 0.25$  m)



(b) IP ( $Y = 0.15$  m)



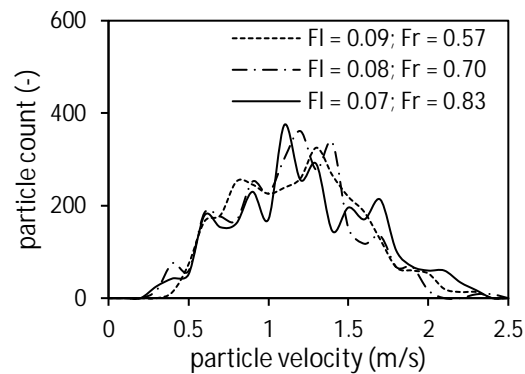
(c) BIP ( $Y = 0.05$  m)

Figure-5.7: Distribution of gas phase velocity at various axial locations

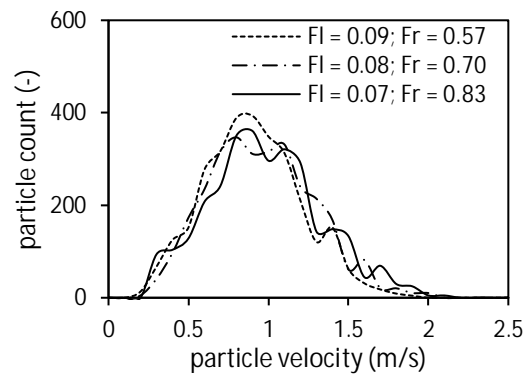
All valid bubbles detected by optical probe at 5 radial positions at AIP and BIP and 3 radial positions at IP were accounted for calculating bubble chord length and velocity distribution. Bubble chord length distribution presented in Figure-5.6 demonstrates the effect of impeller speed on bubble size at three different axial locations. It was observed that at AIP (Figure-5.6a) and BIP (Figure-5.6c), bubbles with a chord length of 0 to 8 cm were recorded and chord length distribution became narrower with increase in Fr. At IP (Figure-5.6b), significant reduction in bubble size was found. Chord length values reduced by more than half in comparison to AIP and BIP. More than 50% of entire bubble population had a chord length less than 0.5 cm. This could be the result of shearing through impeller blades which promoted fine bubble generation and prevented bubble coalescence at IP. It was also observed that the impact of Fr on the chord length distribution profile was minor at IP in comparison to other axial locations. Figure-5.6(c) shows that at low impeller speed ( $Fr = 0.57$  and  $Fl = 0.09$ ), entire bubble population was well distributed with chord lengths in the size range of 0 to 4 cm. At the radial locations of  $r = 0.03$  to  $0.11$  m, gas bubbles emerging axially upwards from the ring sparger undergo interactions with bubbles in the recirculation loop (Figure-5.5a) causing bubble coalescence. On the other hand, bubble break up increased due to strong liquid recirculation near wall where the influence of sparger was less bubble break up increased due to strong liquid recirculation. Therefore, chord length distribution at BIP was mainly determined by the balance between coalescence and break up phenomena. However, with an increase in Fr to 0.70, distribution became narrow with a peak value at approximately 0.5 cm.

In stirred tanks, the velocity of bubbles is influenced by both buoyancy effect and liquid circulation. Therefore, the velocity reported in this chapter represents gas phase velocity rather than bubble rise velocity. Figure-5.7(a) demonstrates that Fr does not alter the gas phase velocity distribution profiles to a significant extent at AIP. Here, most of the bubble population travelled at a velocity less than 0.7 m/s. At IP (Figure-5.7b), gas phase velocity distribution was in accordance with impeller speed with the velocity peak value shifted right from 0.75 to 1.25 m/s with increase in Fr number from 0.57 to 0.83. In addition, at IP, large number of bubbles travelled at above 1 m/s which was approximately twice as high as gas velocities observed at AIP and BIP. Mostly unimodal distribution of gas velocities was observed at AIP and IP; whereas no such pattern was observed at BIP. The rise and dip pattern in velocity profiles was due to the difference in velocities of gas bubbles coming out of sparger and from the gas bubbles carried by recirculation loop as explained earlier.

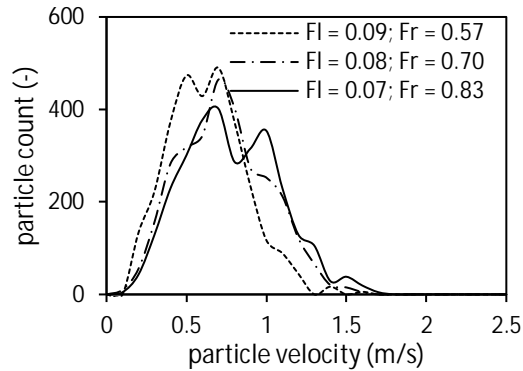
#### Particle velocity distribution in GLS-ST



(a)  $r = 0.11$  m



(b)  $r = 0.15$  m



(c)  $r = 0.19$  m

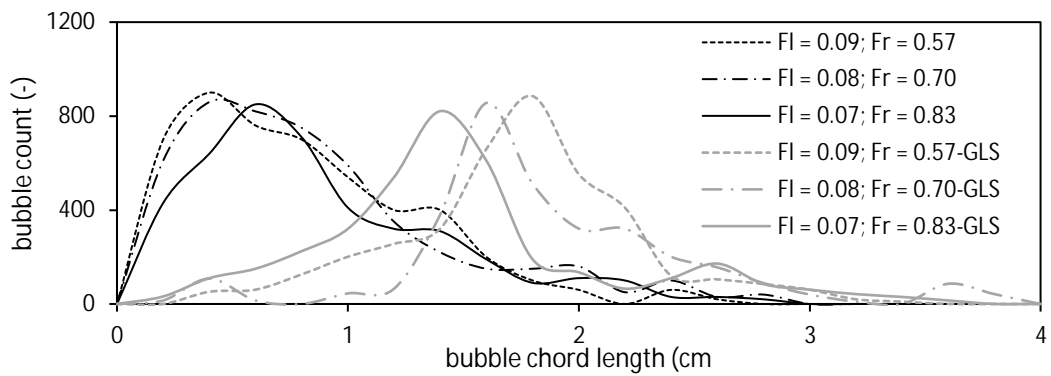
Figure-5.8: Effect of impeller speed on particle velocity distribution at IP ( $Y = 0.15$  m)

Experiments in GL-ST were followed by simultaneous measurements of particle velocities, and local bubble dynamics at IP in GLS-ST. The operating conditions were kept same and the tap water from GL-ST experiments was replaced by a slurry which consisted of 1% by weight fine sand with an average particle diameter of  $350 \mu\text{m}$ . It was also ensured that all particles were in complete suspension (144) during experiments. Particle velocity distribution at each radial location in IP, at three different operating conditions, are shown in Figure-5.8. It should be noted that the velocity values for solid phase presented here represent the resultant velocity magnitude. It could be seen that particle velocities were higher near impeller blades ( $r = 0.11$  m) and gradually decreased towards the wall ( $r = 0.19$  m) at all operating conditions. Particularly, the difference in peak velocity was 47% between blade and tank wall at  $Fr = 0.83$ . Moreover, the spread for velocity distribution near blade was in the range of 0 to 2.5 m/s; which reduced to 2 m/s at centre ( $r = 0.15$  m) and reduced further to 1.7 m/s near the wall. Such radial variation in velocity values indicated the particle velocities near the wall was mainly influenced by liquid flow pattern rather than impeller propelling force. It was also observed that at a given radial location, increasing  $Fr$  does not produce any significant effect on the particle velocities for the experimented conditions (low solid loading: 1%).

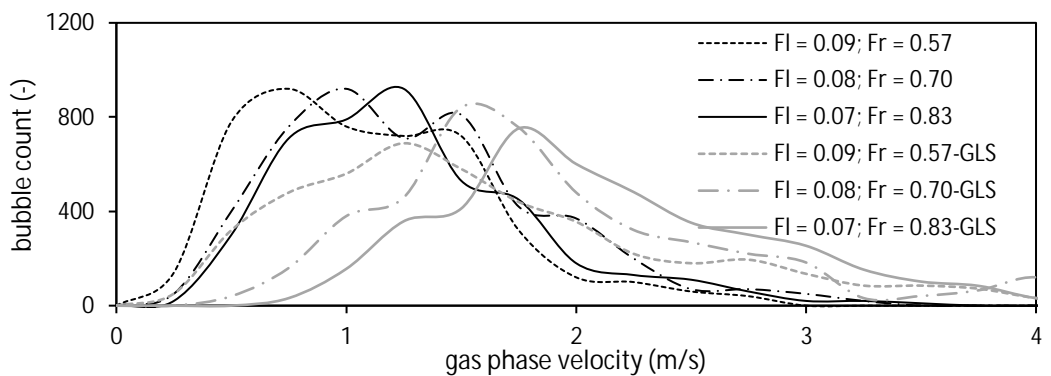
#### **Local bubble dynamics in GLS-ST**

Effect of solid loading on bubble chord length distribution is shown in Figure-5.9(a). In the plots, black lines represent distribution profiles obtained from GL-ST

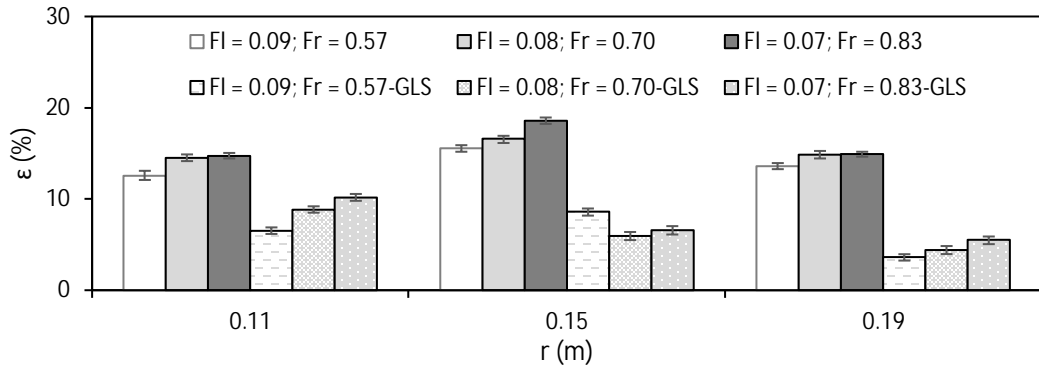
experiments and grey lines stands for profiles acquired from GLS-ST measurements. It was evident from the figure that addition of solids resulted in larger bubbles. Especially, peak value for bubble chord length increased by approximately 5 times with solid loading at low impeller speed ( $Fl = 0.09$ ;  $Fr = 0.57$ ). At this speed, most of the power dissipated from impeller was utilized for suspending solids rather than bubble breakup. Also, apparent viscosity of slurry was higher in comparison to tap water due to the presence of fine sand. The higher liquid viscosity promoted bubble coalescence which led to larger bubble formation. Nevertheless, with increase in  $Fr$ , bubble chord length reduced to 1.4 cm. Impact of solid loading on the gas phase velocity distribution is shown in Figure-5.9(b).



(a) Bubble chord length distribution



(b) Gas phase velocity distribution



(c) Gas holdup

Figure-5.9: Effect of solid loading on local bubble dynamics at IP ( $Y = 0.15$  m)

It could be seen that the gas phase velocities increased in GLS-ST in comparison with GL-ST. Velocity distribution also became broader with increase in velocity range from 0 to 3 m/s in GL-ST to 0.2 to 4.25 m/s in GLS-ST. For instance, the peak gas phase velocity increased from 0.08 m/s to 1.5 m/s with addition of solids at  $FI = 0.08$ . However, in GLS-ST, increase in gas phase velocities with increase in impeller speed was found to be consistent with GL-ST. The influence of solids on radial variation of gas hold-up is shown in Figure-5.9(c). Gas holdup reduced drastically with addition of solids at all radial locations. The reduction in gas holdup was found to be maximum near tank wall where holdup reduced from 13.6 to 3.6% at  $FI = 0.09$ . Significant reduction in holdup could be attributed to several factors which includes increase in gas phase velocity that reduced bubble residence time; lower bubble frequency due to bubble coalescence and change in liquid recirculation pattern with addition of solids. Effect of impeller speed on gas holdup in GLS-ST could not be identified near tank wall due to overlapping error bars. However, notable increase in holdup with speed was observed near impeller blades ( $r = 0.11$  m) with the values increasing from 6.5 to 10.18% when  $Fr$  was increase from 0.57 to 0.83.

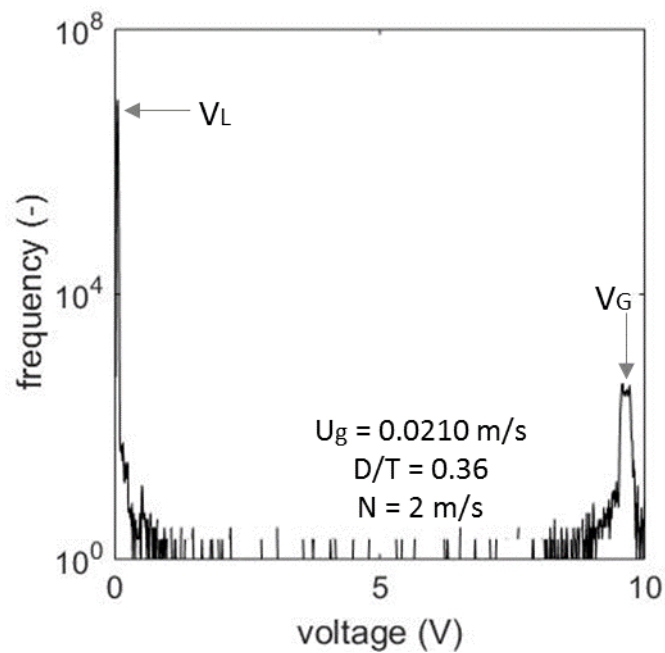
### 5.3.2 GL-ST with RT

#### Flow regime identification

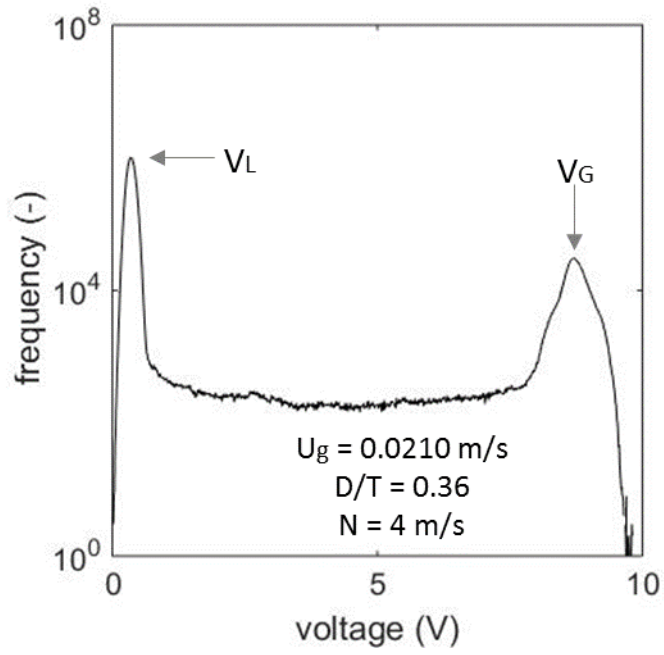
Ability of optical probe to detect operating regimes was tested in GL-ST experiments discussed in this section. Flow regime map was constructed based on the optical probe signal, and the same was verified by visual observation. For each experiment, a



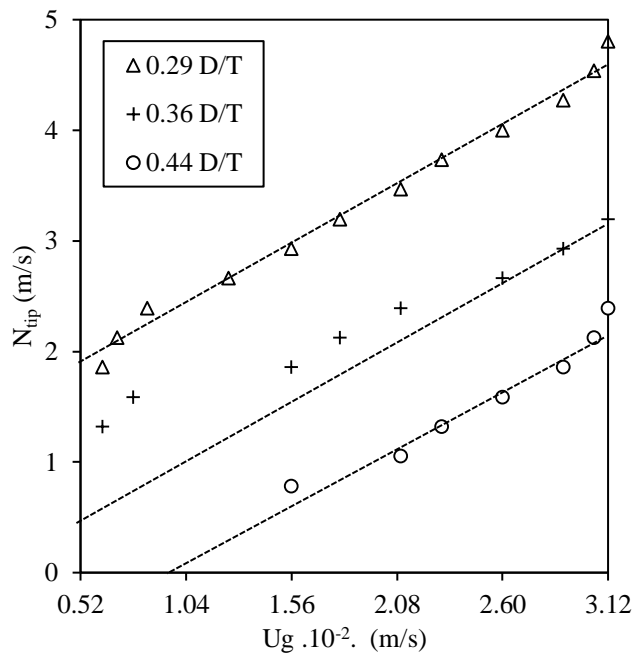
histogram of the time-voltage series was plotted that resulted in two separate peaks. Characteristic histograms are obtained for flooded (Figure-5.10a) and dispersed flow regime (Figure -5.10b). At flooded flow condition, less gas was dispersed and so does the number of rise in voltage signals. At dispersed flow regime, more bubbles were encountered by the probe tip, and hence two distinct peak appeared representing liquid phase at low voltage side and gas phase at high voltage side. Flow regime map developed for the experimented impellers based on the histogram method is shown in Figure-5.10(c). The dotted lines in the plot represent operating lines for three different impeller diameters. The region above the dotted line for a given D/T indicates dispersed flow in the tank, whereas the region below represents flooded flow condition. Operating lines indicate that the increase in impeller diameter leads to high gas dispersion. For example, at a gas superficial velocity of 0.0312 m/s, to disperse the gas, SRT with 0.29 D/T should be operated at 4.8 m/s whereas the SRT with 0.44 D/T achieves dispersed flow at the impeller speed of 2.1 m/s.



(a) Flooded



(b) Dispersed

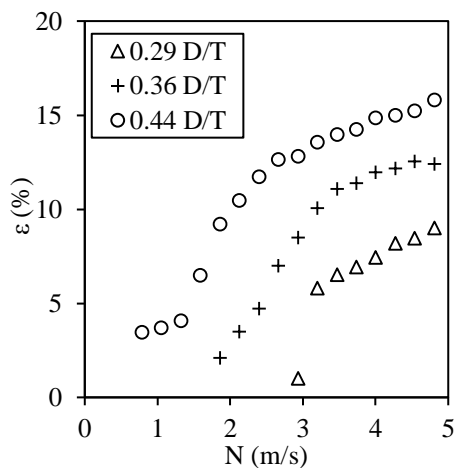


(c) Operating regime map for the tested impellers

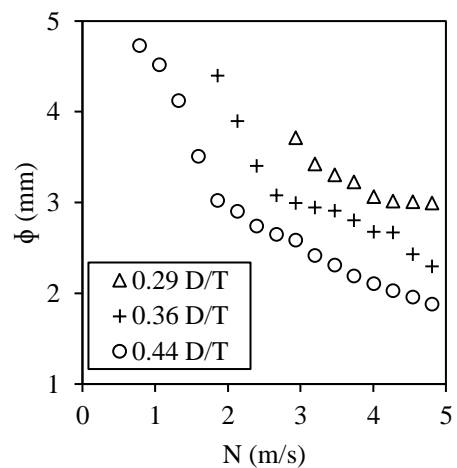
Figure-5.10: Identification of operating regimes using optical probe

## Effect of impeller speed and D/T

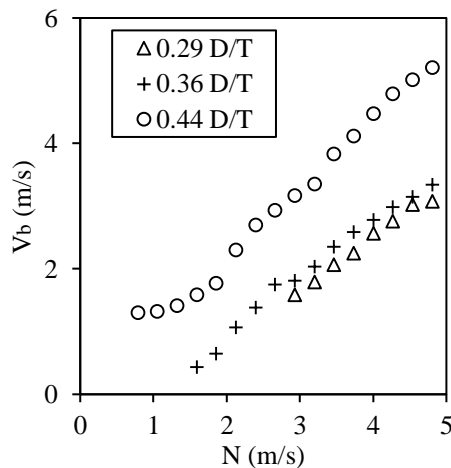
Effect of impeller diameter and speed on time-averaged local gas holdup at a fixed superficial gas velocity of 0.0156 m/s is shown in Figure-5.11(a). The gas holdup increases with an increase in impeller diameter. At a fixed impeller speed of 4 m/s, gas holdup increased twofold with an increase in D/T from 0.29 to 0.44. The reason is as follows: when impeller diameter increased, length and width of blades increase resulting in larger contact area between blades and gas phase. The increase in contact area break the gas bubbles accumulated behind the blades, leading to high gas holdup. On contrary, for smaller D/T (0.29) it is difficult to pump the gas till the impeller speed of 2.9 m/s resulting in the poor gas dispersion. For all the tested D/Ts, increase in impeller speed also led to increase in holdup. Similar observations were reported by several researchers earlier (4, 15, 49).



(a) gas holdup



(b) bubble chord length



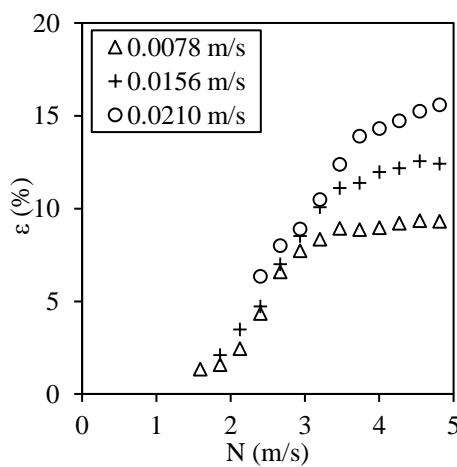
(c) gas phase velocity

Figure-5.11: Effect of impeller diameter and speed on gas dispersion ( $U_g = 0.0156$  m/s) [ $Y = 0.15$  m;  $r = 0.15$  m]

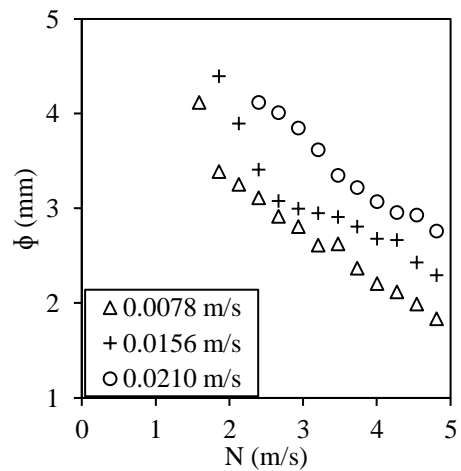
Increase in speed intensified blade to bubble contact and hence, frequency of bubble shredding increased resulting in higher gas holdup and uniform gas dispersion throughout tank. Specifically, for RT with 0.44 D/T operated at a maximum speed of 4.8 m/s recorded highest holdup of 16% whereas at 0.8 m/s resulted in only 3%.

Figure-5.11(b) represents effect of impeller diameter and speed on bubble chord length. Different sized bubbles ranging between 2 to 5 mm were recorded. Increase in impeller diameter reduced chord length as it caused high bubble shredding as reported by Laakkonen et al., (57). At impeller speed of 4.8 m/s, the bubble size reduced by 76% with an increase in the impeller diameter ratio from 0.29 to 0.44; however, the reduction of less than 20 % was found when D/T was increased from 0.36 to 0.44. At low impeller speeds, gas velocity coming out of sparger dominated impeller propelling force, leading to higher coalescence and increase in bubble diameter. At high impeller speeds, for 0.44 D/T, bubble chord length reduced by the factor of 1.5 when the speed was increased from 2.9 to 4.8 m/s. Figure-5.11(c) indicates that gas phase velocity increases with respect to D/T and impeller speed. This could be due to the strong recirculation liquid velocity with increasing D/T and impeller speed (142).

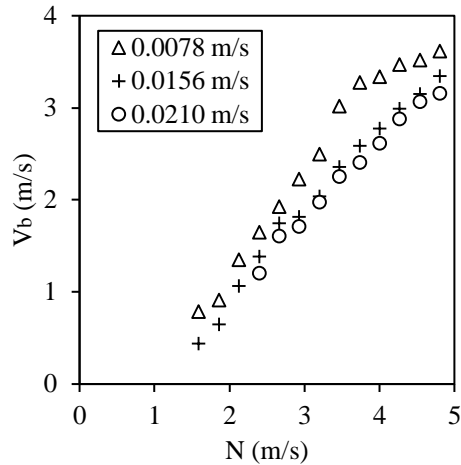
**Effect of superficial gas velocity**



(a) gas holdup



(b) bubble chord length



(c) gas phase velocity

Figure-5.12: Effect of gas superficial velocity and impeller speed on gas dispersion

Effect of superficial gas velocity ( $u_g$ ) on the gas holdup at fixed  $D/T$  of 0.36 is shown in Figure-5.12(a). As expected, gas holdup boosts with an increase in  $u_g$ . At higher gas flow rates, time spent by the gas bubbles inside the stirred tank increases in comparison to low gas flow rates. The bubble residence time ( $T_M$ ) and bubble count values recorded from these measurement locations were also high compared to low gas flow rates. Increase in  $u_g$  increased the bubble chord length by few mm as shown in Figure-5.12(b). Increase in  $u_g$  promoted bubble coalescence and in turn generation of larger bubbles. Gas phase velocity velocity decreased with increase in  $u_g$  as shown in Figure-5.11(c). This could be owing to the radial positioning of optical probe where the tip is facing inward towards the impeller blade which captured only the radial velocity of the bubbles. Hence the effect of  $u_g$  on bubble velocity was not accurately captured. However, with respect to impeller speed, gas phase velocity increased and the profile looks similar to Figure-5.11(c).

## Power consumption

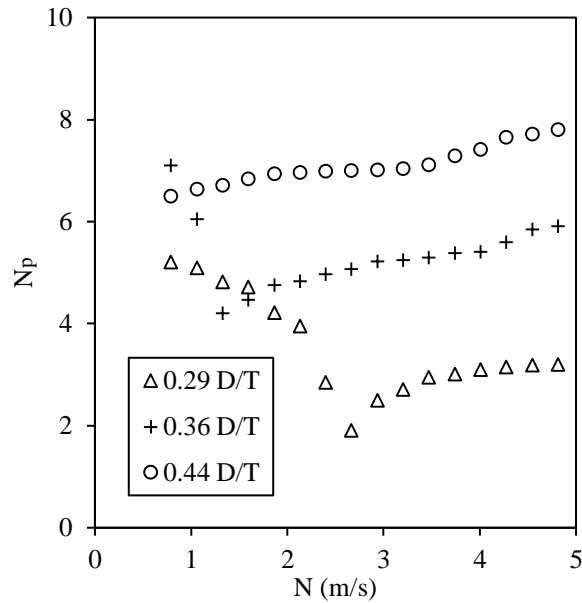


Figure-5.13: Effect of impeller diameter and speed on power consumption

$$(U_g = 0.0156 \text{ m/s})$$

Effect of impeller diameter and speed on power number at a fixed superficial gas velocity of 0.0156 m/s is shown in Figure-5.13. From previous sections, gas holdup and bubble size values indicated that 0.44 D/T was preferable as it resulted in the highest holdup of 76% and smaller bubble size. But, performance of SRT with a specific impeller diameter requires further analysis with respect to its power consumption. Regarding power dissipated to the system, power number increased with increasing impeller diameter. For example, at maximum impeller speed of 4.8 m/s, gas holdup value obtained from 0.44 D/T was 75% higher than from 0.29 D/T, but with 1.5 times increase in power consumption. Regarding impeller speed, power number ( $N_p$ ) value decreased till impeller speed of 2.9 and 1.4 m/s for 0.29 and 0.36 D/T impellers respectively because of flooded condition. The cavity formation behind blades and bubbles escaping through impeller blades reduced the power dissipation at low impeller speeds. For dispersed flow regime, (high impeller speeds) the power required to break the cavities increased with increasing  $N_p$  values.

### 5.3.3 GL-ST with HSPBT

(Results presented in the following section are published in Chemical Engineering Research and Design Journal (121) )

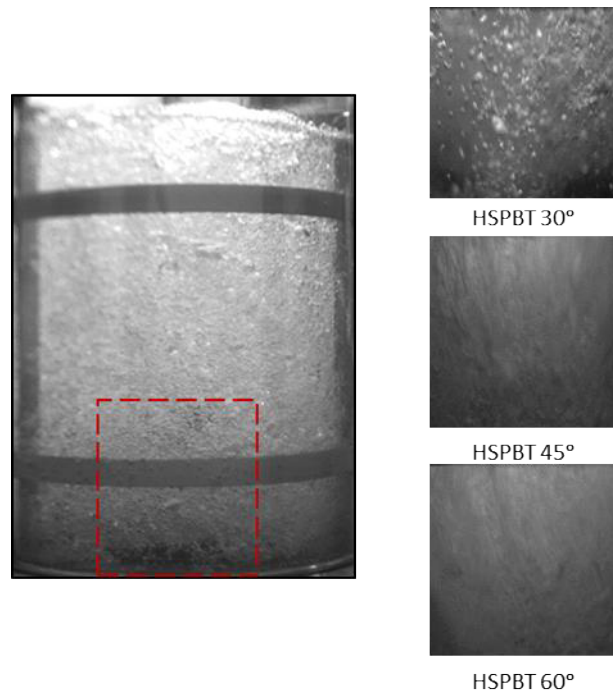


Figure-5.14: Instantaneous photographs for three blade angles [ $N = 425$  rpm;  $u_g = 0.013$  m/s;  $N_p(30^\circ) = 1.2$ ;  $N_p(45^\circ) = 2.5$  and  $N_p(60^\circ) = 3.2$ ]

Instantaneous photographs covering only one-third of the tank, the i.e. region between two baffles ( $120^\circ$ ) are shown in Figure-5.14. These photographs were taken for the three blade angles of  $30^\circ$ ,  $45^\circ$ , and  $60^\circ$  at an impeller speed of 425 rpm and superficial gas velocity of 0.013 m/s. In all the three photographs, large bubbles were observed in the top section whereas fine bubbles could be seen in the region below the impeller. This observation could be result of higher influence of shear on the gas phase in impeller region. The influence of shear decreases with increase in the axial distance from the impeller. Since HSPBT was mainly used to hold down gas phase in the region below the impeller, gas phase dispersion in this region was shown by a close-up views. For HSPBT $30^\circ$ , bubbles were large and visible; whereas for HSPBT $45^\circ$  and  $60^\circ$ , finer bubbles or dense flow conditions were observed. From the images, it was difficult to observe the effect of  $45^\circ$  and  $60^\circ$  blade angle on bubble density. Generation of finer bubbles with an increase in the blade angle was due to increase in impeller swept volume. Impeller swept volumes for HSPBT $30^\circ$ ,  $45^\circ$  and  $60^\circ$  are 8.03, 11.03 and 13.92

( $\times 10^{-4} \text{ m}^3$ ) respectively. Higher the angle of the blade, higher the swept volume and contact area between blades and gas phase. Higher swept volume imparts higher shear causing bubble breakup resulting in finer bubbles. It should also be noted that the increase in shear with blade angle comes with an increase in power consumption. For instance, at 425 rpm and 0.013 m/s, power number ( $N_p$ ) of HSPBT30° was 1.2 whereas  $N_p$  of HSPBT60° was 3.2.

### Overall gas holdup

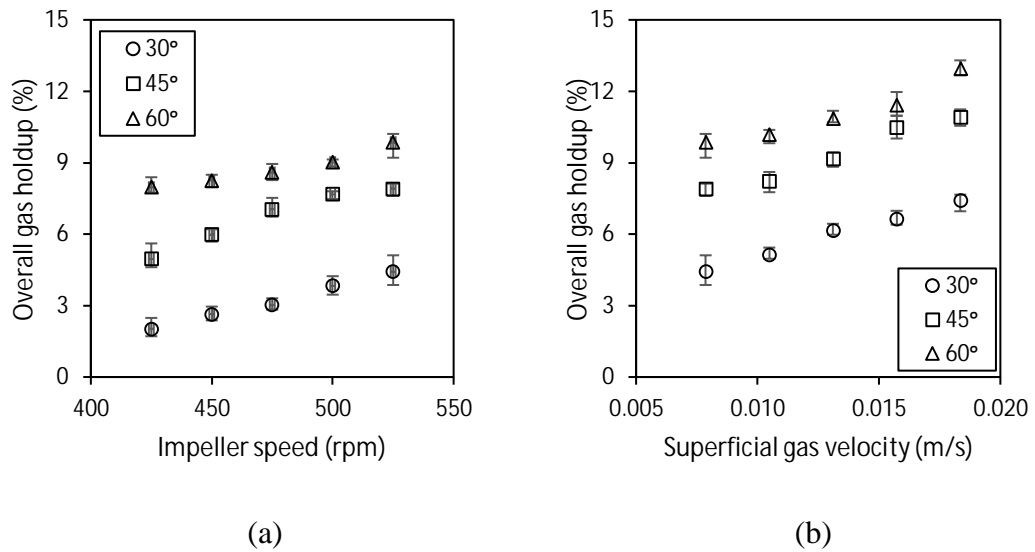


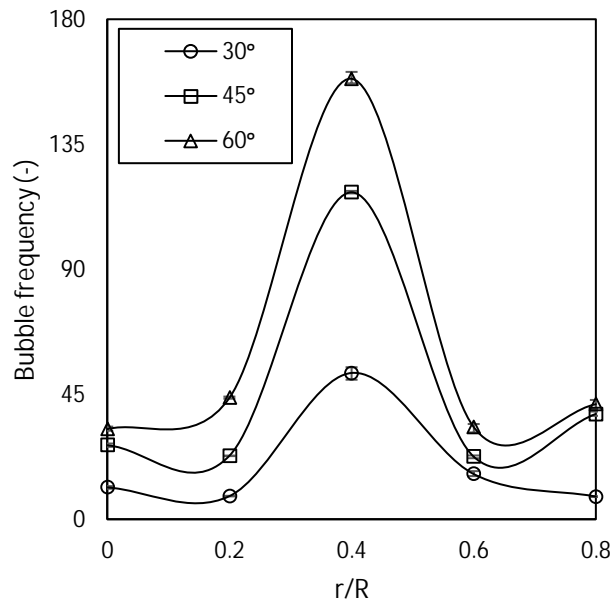
Figure-5.15: Effect of (a) Impeller speed ( $u_g = 0.013 \text{ m/s}$ ) and (b) Superficial gas velocity ( $N = 525 \text{ rpm}$ ) on overall gas holdup [ $N_p(30^\circ) = 1.2$ ;  $N_p(45^\circ) = 2.5$  and  $N_p(60^\circ) = 3.2$ ]

The influence of blade angle at different impeller speed and gas superficial velocity on overall gas holdup is shown in Figure-5.15. Overall gas holdup ( $\epsilon_G$ ) was measured by recording the change in liquid level with aeration ( $h_g$ ) and without aeration ( $h$ ) as  $\epsilon_G = (h_g - h)/h_g$ . Gas holdup increased with impeller speed, blade angle, and superficial gas velocity. The increase in impeller speed intensified blade to bubble contact, and bubble shredding leading to the higher gas holdup. The gas holdup increased as much as 50% when the impeller speed was increased from 425 to 525 rpm for HSPBT30°. Superficial gas velocity ( $u_g$ ) also had a similar effect on overall gas holdup. This increase in a gas holdup with  $u_g$  was attributed to increasing in the volume of gas. Specifically, at a maximum gas superficial velocity of 0.018 m/s, the gas holdup increased three times with an increase in blade angle from 30° to 60°.

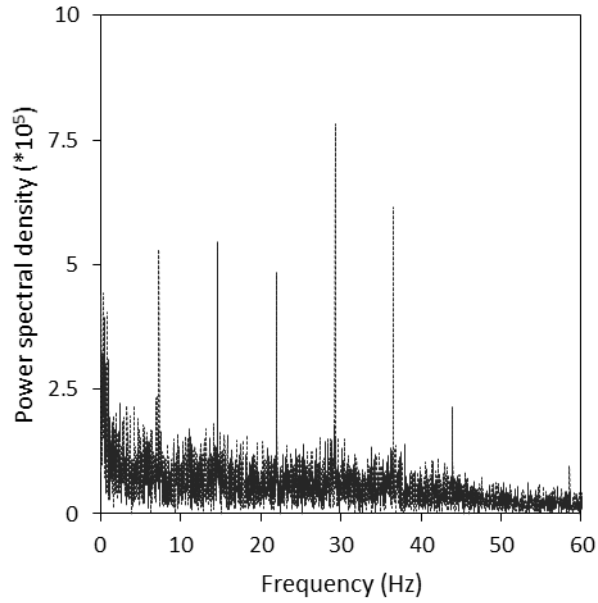


### Power spectra analysis

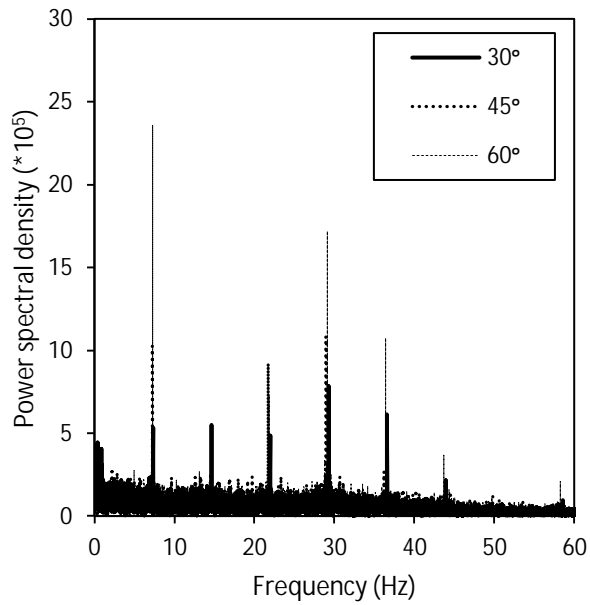
The effect of blade angle on local bubble dynamics was studied by analysing optical probe voltage signals obtained at five radial positions ( $r/R = 0, 0.2, 0.4, 0.6$  and  $0.8$ ) at  $Z$  of  $0.5C$  for the three blade angles. Figure-5.16(a) shows a variation of bubble frequency with respect to blade angle and radial position. Bubble frequency was calculated as the total number of bubbles encountered per second including both valid and invalid bubbles. Highest bubble frequency was observed at  $r/R = 0.4$  where the sparger holes were collinear to the trailing edge of impeller blades resulting in higher number of bubbles. A qualitatively symmetrical profile was observed, and the frequencies were significantly lower at other radial positions.



(a)



(b)



(c)

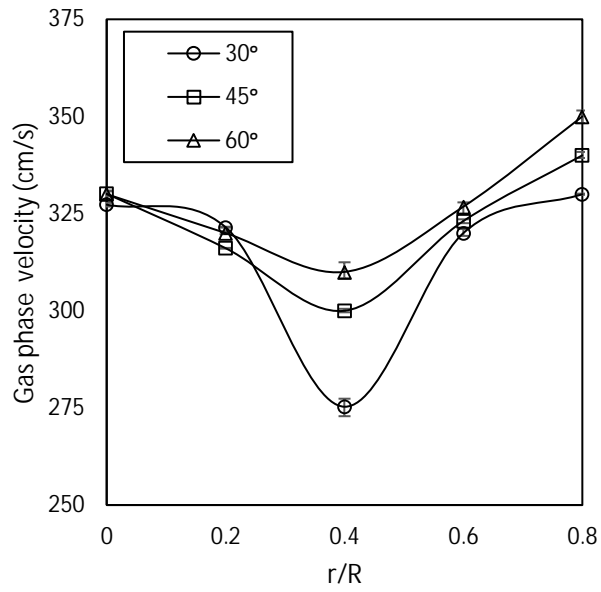
Figure-5.16: (a) Influence of blade angle on time-averaged bubble frequency; (b) PSD for HSPBT30°; (c) Effect of blade angle on PSD [ $N = 425$  rpm;  $u_g = 0.013$  m/s;  $N_p(30^\circ) = 1.2$ ;  $N_p(45^\circ) = 2.5$  and  $N_p(60^\circ) = 3.2$ ]

The peak bubble frequency value at  $r/R = 0.4$  increased by more than three times with an increase in blade angle from  $30^\circ$  to  $60^\circ$ . The highest bubble frequency at  $r/R = 0.4$

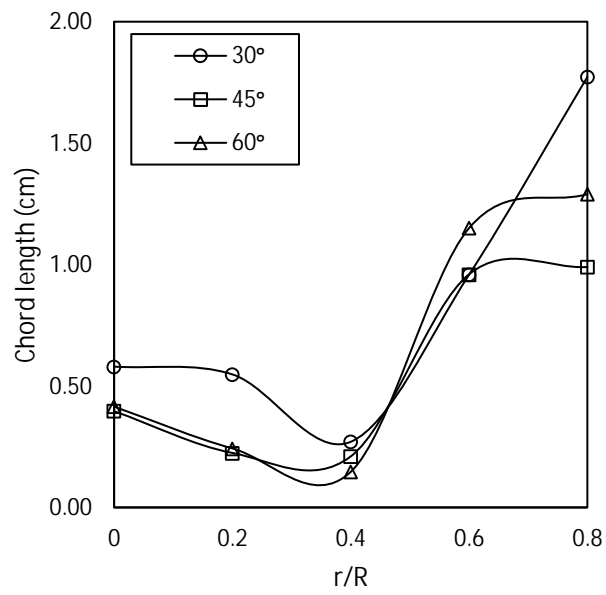
could be further related to the cavity formation behind the impeller blades. For PBT, increase in gas flow rate at a constant impeller speed results in four different shapes of cavities starting from vortex cavity at low gas flow rates to large cavity at high gas flow rates (145). In this study experiments were conducted at high gas flowrates; and therefore, predominantly large cavity structures were expected. These large cavity structures were typically unstable and break into smaller bubbles leading to increase in bubble frequency at impeller trailing edge (or  $r/R = 0.4$ ). The voltage signal ( $r/R = 0.4$ ) was further analysed using power spectra density (PSDs) for HSPBT60° (Figure-5.16b). The PSDs had several distinct dominant frequencies related to the impeller rotation frequency ( $N = 7.08$  rps). The PSDs for three angles are shown in Figure-5.16(c). As the blade angle increased, the height of the peaks also increased owing to the variation in power input for each blade angle. For 60°,  $N_p$  was approximately thrice of  $N_p$  at 30° blade angle.

### **Local bubble dynamics**

Figure-5.17(a) shows time-averaged gas phase velocity at different radial positions for the three blade angles. The velocity profiles have a convex shape with the lowest velocity at  $r/R = 0.4$  and peak velocity near the tank wall ( $r/R = 0.8$ ) for all three blade angles. Average gas phase velocity at  $r/R = 0.4$  is ~20% lower compared to the tank wall or centre. Bubble velocity below the impeller was predominantly influenced by liquid recirculation loop generated by the down-pumping action of the impeller as well as the upward velocity of the gas injected through the ring sparger. At  $r/R = 0.4$ , the impeller trailing edge was collinear with the sparger holes. The bubbles at this radial position experience two opposing forces, one caused by the upward velocity of the injected gas and the other by the downward velocity of the recirculation current. Towards the tank centre ( $r/R = 0$ ) and near the tank wall ( $r/R = 0.8$ ), only recirculation current governs the bubble movement. Influence of blade angle on chord length at different radial positions is shown in Figure-5.17(b).



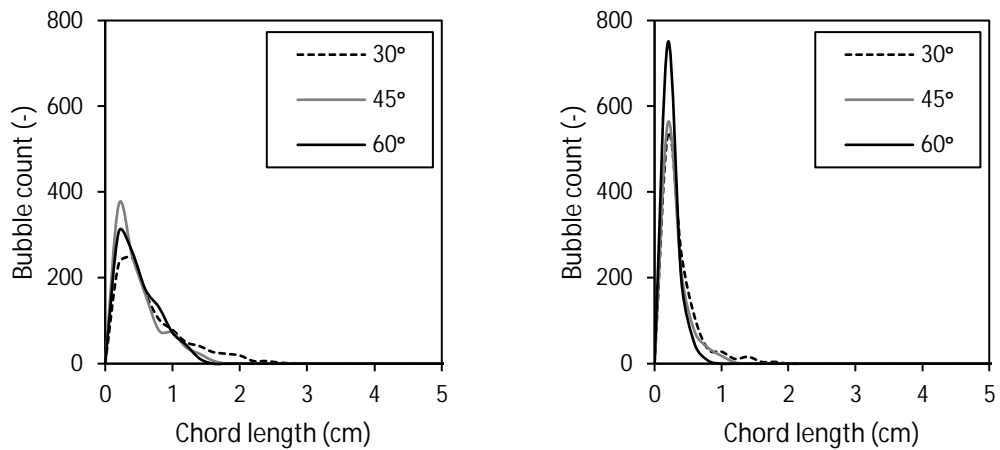
(a)



(b)

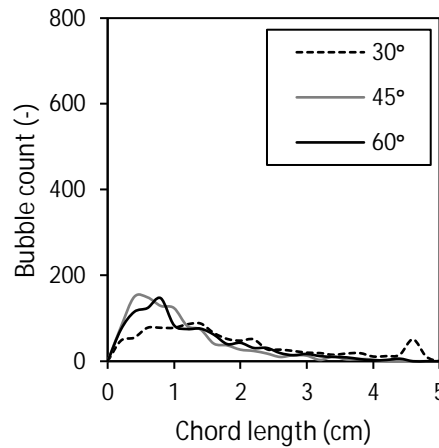
Figure-5.17: Influence of blade angle on (a) Gas phase velocity and (b) Chord length [N = 425 rpm;  $u_g = 0.013$  m/s]

For all three blade angles, average chord length reduced by half from the centre of the tank to blade's trailing edge; whereas from the blade edge to the tank wall, the chord length increased approximately three times. Higher chord lengths ( $> 1$  cm) near tank wall could be due to the bubble accumulation and coalescence. Lower chord lengths at radial positions of 0.2 and 0.4 could be attributed to impeller shear, which causes bubble break up in impeller region. HSPBT60° generates finer bubbles up to  $r/R = 0.4$ , whereas HSPBT45° generates small bubbles ( $< 1$  cm) at all radial positions.



(a)  $r/R = 0.8$

(b)  $r/R = 0.4$



(c)  $r/R = 0$

Figure-5.18: Effect of blade angle on chord length distribution (a)  $r/R = 0.8$ ; (b)  $r/R = 0.4$ ; (c)  $r/R = 0$

Average chord lengths for all three blade angles vary between 0.2 and 1.8 cm (Figure-5.18b). However, it was interesting to see the distribution of chord length at different radial positions. The chord length distribution near the tank wall ( $r/R = 0.8$ ) showed wide distribution from 0.5 to 2.75 cm. For all blade angles, a significant amount of larger bubbles with chord length more than 1 cm were observed near tank wall. However, HSPBT45° resulted in 72% and 26% higher smaller bubbles compared to 30° and 60° respectively. This could be attributed to a higher blade angle of HSPBT60°, which threw a portion of the gas bubbles radially outward towards the wall rather than pumping it towards the tank bottom. In Figure-5.18(b) for  $r/R = 0.4$ , bubble chord length became smaller and distribution became narrower than that at  $r/R = 0.8$ . At this radial position, HSPBT60° generated a significant number (>20 %) of smaller bubbles than the other blade angles. At the centre of the tank ( $r/R = 0$ ), HSPBT45° resulted in higher number of smaller bubbles compared to 30° and 60° (Figure-5.18c). At both extreme positions ( $r/R = 0$  and 0.8), HSPBT45° generated finer bubbles than HSPBT60°.

### **Bubble population classification**

The entire bubble population was classified into different size groups to analyse the gas holdup and bubble velocity contained in each size group. The chord length distribution was plotted as bubble count vs. chord length (Figure-5.19). The plot exhibited a steep decline in slope (inset Figure-5.19) up to 0.6 cm. A distinct change in slope occurs at ~0.6 cm for all three impeller blade angles. To avoid repetition, plots for HSPBT30° and 45° are not shown here. Based on the peak value at 0.6 cm, the detected bubbles were classified into two size groups, namely G1- smaller bubbles from 0 – 0.6 cm and G2- bubbles > 0.6 cm. Average gas phase velocity and a fraction of overall gas holdup contained in two size groups are shown in Table-2. The gas phase velocities of G1 increased with an increase in the blade angle, whereas that of G2 remained almost constant for all the blade angles. Also, gas phase velocities of G2 were always higher than that of G1. Gas holdup due to G2 was higher than that due to G1 for all three blade angles. HSPBT45° generated finer bubbles and had 30% higher contribution by the smaller bubbles than HSPBT30° and HSPBT60° to the overall holdup.

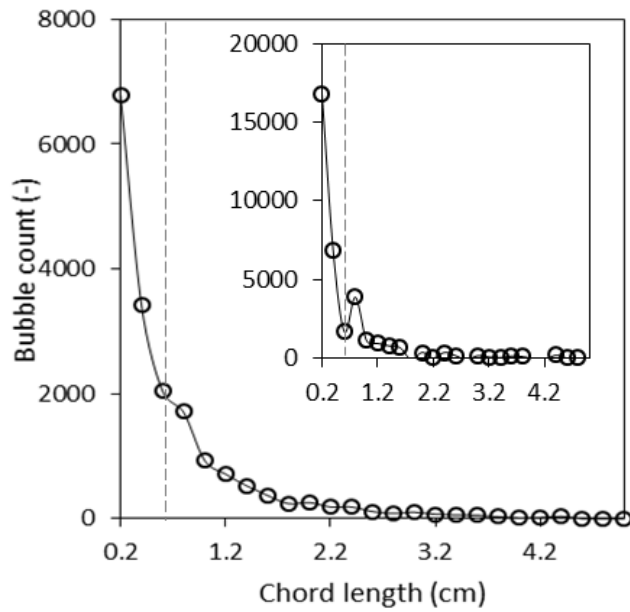
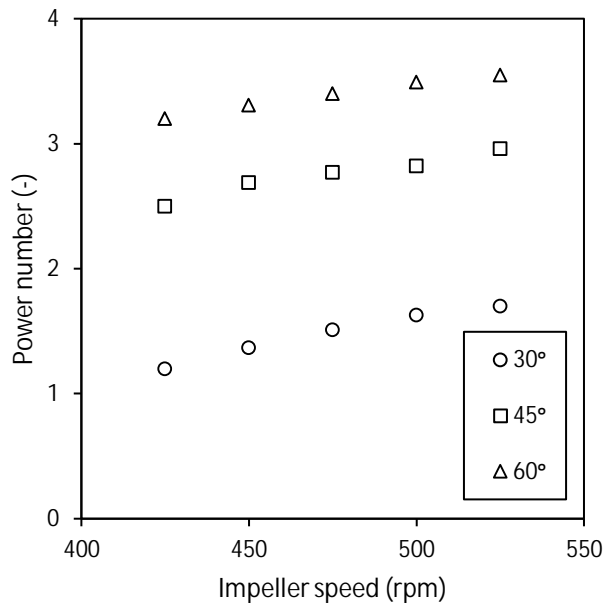


Figure-5.19: Bubble size classification (HSPBT60°) [ $N_p(30^\circ) = 1.2$ ;  $N_p(45^\circ) = 2.5$  and  $N_p(60^\circ) = 3.2$ ]

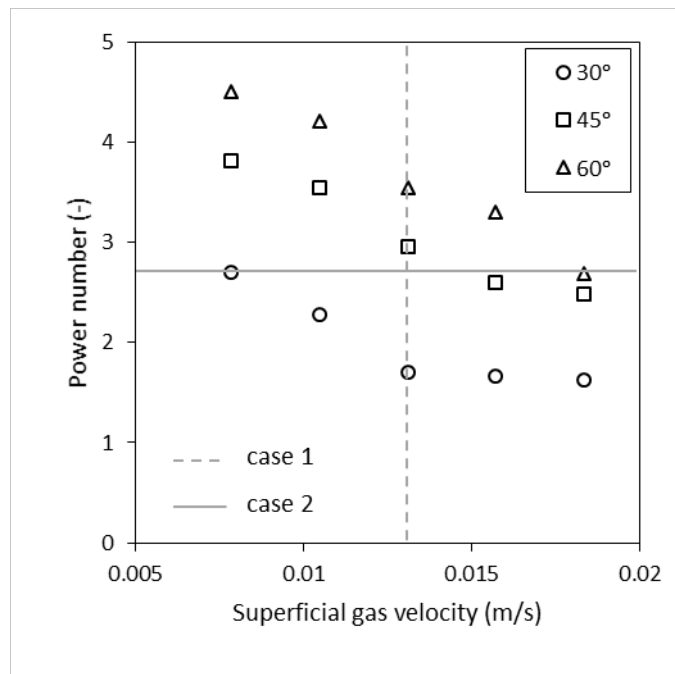
### Power consumption

Power consumption by HSPBTs of different blade angles was further analysed by comparing power numbers at different impeller speeds (Figure-5.20a), and superficial gas velocities (Figure-5.20b). Power number increased with increasing impeller speed and reduced with increasing gas velocity. For a given superficial gas velocity (Figure-5.20b), HSPBT30° consumed significantly less power; whereas, with HSPBT60°, more gas was sparged through the tank at the same power. However, this does not imply superior performance of HSPBT60° compared to the rest. Power consumed by an HSPBT in a gas-liquid stirred tank depends on impeller speed, gas velocity, and blade angle. To compare blade angles at constant power, variation in either impeller speed or gas velocity is required. Therefore, experiments were also conducted by varying impeller speed and superficial gas velocity. For the operating conditions selected in this work, distinct, non-overlapping ranges of power number were obtained at different blade angle. Thus, the blade angles could not be directly compared to a constant power number. If we broaden the range of impeller speeds, HSPBT30° showed flooding behaviour at lower impeller speeds, whereas, at higher impeller

speeds HSPBT60° reached critical impeller speed resulting in shaft bending and torque instabilities.

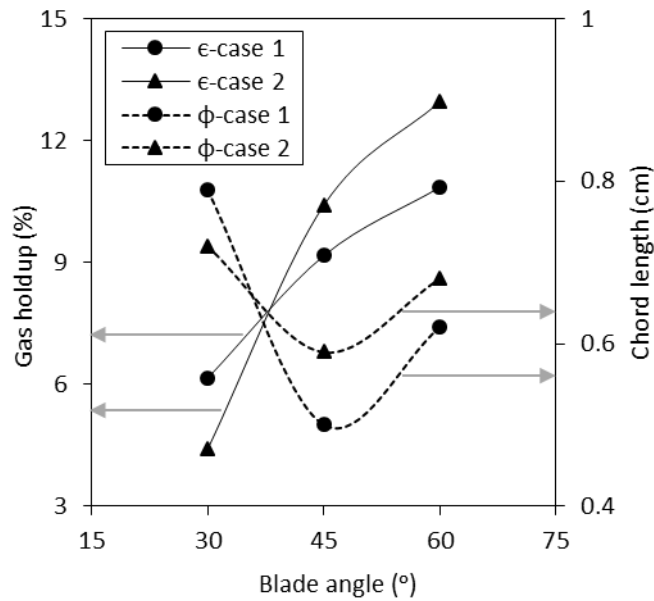


(a)



(b)





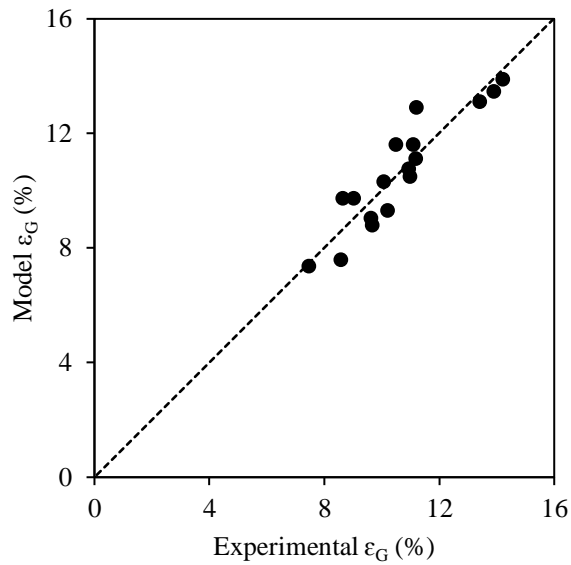
(c)

Figure-5.20: Influence of (a) impeller speed and (b) superficial gas velocity on power consumption, (c) Effect of superficial gas velocity and power number on gas holdup and bubble chord length

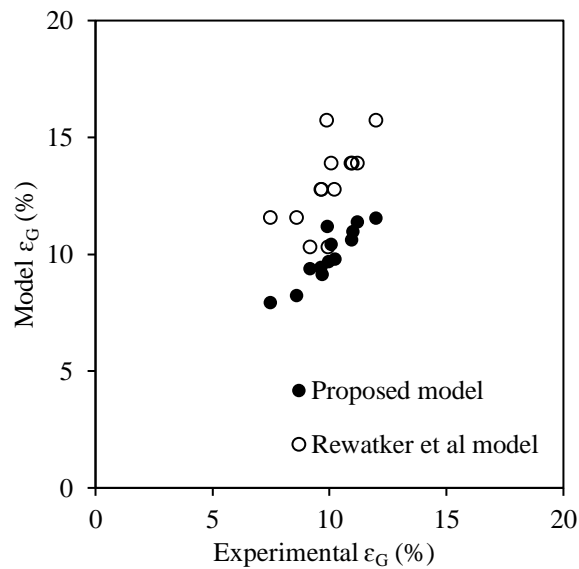
By varying the gas superficial velocity, performance of the three blade angles could be compared at constant power input. Two cases were considered (Figure-5.20b); in case-1, gas superficial velocity was kept constant at 0.013 m/s and the corresponding power number was chosen from Figure-5.20(b). In case-2, power number was kept constant at 2.7 which was the maximum power number for HSPBT30° for the experimented conditions. The impeller speed was fixed at 525 rpm for both the cases. Gas holdup and chord length for both the cases are shown in Figure-5.20(c). Gas holdup increased with an increase in blade angle for both the cases. For case 1, increase in power input resulted in an increase in shear resulting in finer bubbles, and high gas holdup. For case 2, high volumes of gas sparged into the tank led to increase in gas holdup. At the same time, high gas volumes resulted in bubble coalescence and large chord lengths in comparison with case 1. In both the cases, similar bubble chord length profile was obtained with HSPBT45° generating smaller bubbles. The analysis suggested that to select HSPBT blade angle for a given application, a rational

optimization of the gas holdup, percentage contribution to the overall holdup by smaller bubbles, and power consumption should be considered.

#### 5.4 EMPIRICAL CORRELATION



(a)



(b)

Figure-5.21: (a) Model predicted holdup vs. experimental holdup and (b) Comparison of gas holdup between proposed model and model from literature

From the calculated global gas holdup data for HSPBT (accounting all experimented impeller speeds and blade angles), an empirical correlation of global gas holdup as a function of impeller speed and blade angle (presented as Weber number) is derived. The proposed model predicts the current experimental data with the maximum discrepancy of  $\pm 13\%$  as shown in Figure-5.21 (a).

$$\varepsilon_G = 0.0485N_{we}^{0.61}\theta^{0.1068} \quad (1)$$

Almost all the available correlations in literature are developed for standard Rushton turbines. Few correlations are available to predict gas holdup for pitched blade turbines. In addition, it is noteworthy that such empirical correlations are proposed in previous studies (6, 50, 51), without considering the parameter of impeller blade angle. Figure-5.21 (b) shows the comparison of the proposed empirical correlation for HSPBT with Rewatkar et al correlation (equation 2).

$$\varepsilon = 3.54Fl^{0.43}Fr^{0.51}\left(\frac{D}{T}\right)^{2.08} \quad (2)$$

Since, Rewatkar et al performed experiments with a fixed blade angle of  $45^\circ$ , gas holdup data derived for HSPBT $45^\circ$  was compared with Rewatkar's correlation. The differences between proposed correlation and those reported in literature was found to be 6 to 30%. Such discrepancy might be due to the difference in number of blades and swept area between HSPBT and PBT. Rewatkar et al employed 6 bladed PBT whereas 4 bladed HSPBT was used in the present work.

## 5.5 SUMMARY

In this chapter, local bubble hydrodynamics in baffled stirred tanks equipped with SRT, RTs and HSPBT was investigated. In gas-liquid stirred tank fitted with SRT, gas holdup values at IP were higher than those at AIP and BIP. At BIP, there was no appreciable change in gas holdup values with respect to Fr near sparger outlet ( $r = 0.07$  and  $0.11$  m) and gas holdup was found to be lower (below 4%). SRT used in the present study was a radial impeller which discharged gas bubbles radially rather than pumping it down. Consequently, gas velocity from sparger dominated the liquid velocity generated by SRT. Hence, at BIP, fast rising gas bubbles spent less time in the probe

tip which led to reduction in bubble residence time causing lower gas holdup. At IP, chord length values were reduced by more than half (from approximately 8 to 3 cm) in comparison to other axial locations and more than 50% of entire bubble population had a chord length less than 0.5 cm. It was also observed that a large number of bubbles travelled at above 1 m/s at IP which was approximately twice as high as gas velocities observed at AIP and BIP. With solid loading, power dissipated from the impeller was mostly utilized for suspending solids rather than bubble breakup. Consequently, bubble size, and gas phase velocities increased and gas holdup reduced in comparison with GL-ST. The reduction in gas holdup was found to be maximum near tank wall where it reduced from 13.6 to 3.6%. At IP, particle velocity distribution range decreased from 2.5 to 1.7 m/s and the peak velocity reduced by 47% when the particles moved away from blade to the tank wall. It was also observed that at a given radial location, increasing Fr does not produce any significant effect on the particle velocities at low solid loading.

Influence of impeller diameter on time-averaged gas holdup, chord length and velocity was investigated. When impeller diameter was increased, blade width and length increased resulting in high contact area between blades and gas phase leading to enhanced gas dispersion. With respect to operating conditions, gas holdup and chord length increased with increasing superficial gas velocity. In addition, increasing impeller speed enhanced contact frequency between the blades and bubble causing more bubble shredding and holdup. Based on the results, empirical correlations to predict gas holdup, chord length and velocity have been proposed.

In HSPBT experiments, optical probe detected significantly more gas bubbles below the impeller blade trailing edge ( $r/R = 0.4$ ) in comparison to other radial positions. The chord length distribution suggested that finer bubbles tend to concentrate near the impeller trailing edge and tank centre than the tank wall. Consequently, higher bubble frequencies were observed at the impeller trailing edge, which might be due to breaking up of large cavity structure behind the impeller blades. The power spectra analysis of voltage signal from the optical probe showed periodic sequences of dominant frequencies related to the impeller rotation frequency. The bubble population classification suggested that HSPBT45° generated a number of smaller bubbles than larger bubbles. The increase in the blade angle increased overall gas holdup and gas fraction of larger bubbles at the expense of power dissipation. Compared to

HSPBT30°, for same power input, HSPBT45° and HSPBT60° required lower gas velocities to obtain similar gas holdup. Also, these two blade angles resulted in smaller bubble size.

# Chapter 6

## Conclusions and future work

### 6.1 CONCLUSIONS

The objective of this study was to investigate local bubble hydrodynamics in multiphase stirred tanks. To achieve this objective, different parameters such as impeller speed, gas superficial velocity, solid loading, and impeller geometry which govern the gas-liquid hydrodynamics, and power consumption were investigated. Local bubble hydrodynamics and power consumption were quantified by optical probe and strain gauge measurements respectively. In addition, vortex ingestion and gas-liquid dynamics in unbaffled tank were examined by optical probe measurements, and VOF simulations. Specific conclusions arrived from this study are summarised below:

#### **6.1.1 Simultaneous measurements of local bubble dynamics and particle velocities using optical probe**

Previous studies clearly indicated that most of the experiments on stirred tanks have been conducted using GL-STs and reported overall gas holdup and average bubble size. These studies also showed that local BSD was confined to dilute flow conditions and lab scale stirred tanks mainly due to limitations of the measurement techniques. Thus, in Chapter-3, the potential of optical probe to measure local bubble hydrodynamics, and particle velocities in a slurry bubble column at dense gas flow conditions was investigated. Preliminary validation experiments were carried out to quantify the intrusive errors caused by optical probe. Bubble chord length and seeding particle velocities measured by optical probe were quantified by high speed imaging and PIV techniques respectively. Based on the results, following conclusions are listed below:

- It was observed that optical probe interacted with the flow domain resulting in marginal reduction of seeding particle velocity (liquid velocity,  $V_L$ ). Especially, discrepancy on  $V_L$  values between PIV and optical probe was 20% at low superficial liquid velocity ( $U_L$ ), whereas the difference reduced up to 13% when  $U_L$  was increased.

- Variation in bubble chord length between probe, and high speed imaging was confined to  $\pm 8\%$ .
- The ability of probe to measure local bubble dynamics at high gas holdup conditions were demonstrated using dense gas flow experiments. Gas holdup of upto 43% were successfully captured by the probe.
- In slurry bubble column experiments, solid loading promoted bubble coalescence which led to an increase in chord length and bubble velocity, while reducing in gas holdup.
- Particle velocities were found to be approximately 50% lower than bubble velocities at all measured locations.
- It was observed that optical probe could not distinguish between two different sized particles. When a large and fine particle approached the probe tip simultaneously, optical probe was able to detect only the frequency generated by large particle.

### **6.1.2 Vortex ingestion in unbaffled tank**

The ability of probe as a reliable measurement technique to measure local bubble hydrodynamics and particle velocities was illustrated using slurry bubble column experiments. However, flow in a stirred tank is highly turbulent compared to slurry bubble column. Therefore, additional experiments on lab scale unbaffled stirred tank were carried out prior to employing probe in highly turbulent pilot scale baffled stirred tank. In unbaffled tank, vortex ingestion led to gas dispersion and therefore vortex shape and local bubble hydrodynamics were quantified using optical probe measurements. Furthermore, to understand the effect of vortex ingestion on gas-liquid dynamics, VOF simulations using multiple reference frame and Reynolds stress turbulence model were carried out. The conclusions of this chapter are as follows:

- Without vortex ingestion, the change in vortex shape with increasing impeller speed was more pronounced near the shaft as compared to the wall. On the contrary, with vortex ingestion the influence of impeller speed on vortex shape was less pronounced. This was because, when the vortex came in contact with the rotating internals, most of the energy dissipated from the impeller blades were consumed for dispersing gas rather than deformation of the vortex structure.

- Tangential velocity profiles at all axial locations, except for the one below the impeller were highly conformal to vortex width which indicated that above the impeller, tangential velocity distribution governs the shape of vortex and its free surface movement.
- It was found that impeller generated significantly higher axial and radial flow near impeller regions due to the presence of recirculation loops above and below the impeller.
- Gas holdup calculated from optical probe measurements were almost 40% under predicted by simulations which may be due to limitations in the feasibility of placing an optical probe near rotating impeller and inability of VOF model to capture bubble breakup, or coalescence that governed gas holdup throughout the tank.
- The absence of baffles promoted bubble coalescence which resulted in larger bubbles with increasing impeller speed.

### **6.1.3 Local bubble hydrodynamics in baffled stirred tanks**

After evaluating the potential of optical probe to capture local bubble dynamics at dense flow conditions in slurry bubble column and lab scale unbaffled tank, it was employed in baffled stirred tanks. All the measurements were carried out at completely dispersed flow regimes. The study was carried out with three different impeller geometries which accounted SRT, RTs and HSPBT. For SRT studies, the effect of solid loading and impeller speed on local bubble hydrodynamics and particle velocity distribution in GLS-ST was investigated. For RT, influence of impeller diameter and operating conditions on bubble dynamics and power consumption in GL-ST were examined. Finally, impact of HSPBTs blade angle on gas phase hydrodynamics and power consumption in a GL-ST analyzed. The conclusions of this study are as follows:

- For SRT studies carried out in GL-ST, gas holdup values at impeller plane were higher in comparison to other measurement locations. SRT being a radial impeller discharged more gas bubbles radially towards tank wall in comparison to tank bottom. Consequently, gas velocity from the ring sparger dominated the propelling force generated by SRT at below impeller regions. Hence, at these measurement locations, fast rising gas bubbles emerging out of sparger spent less time in the probe tip which led to reduction in bubble residence time



causing lower gas holdup. In SRT studies carried out in GLS-ST, power dissipated from the impeller was mostly utilized for suspending solids rather than bubble breakup. Consequently, bubble size, and gas phase velocities increased and gas holdup reduced in comparison with GL-ST.

- For RT studies, when impeller diameter was increased, blade width and length increased resulting in high contact area between blades and gas phase leading to enhanced gas dispersion. It was also observed that gas holdup and chord length increased with increasing gas superficial velocity. On the other hand, increasing impeller speed enhanced contact frequency between the blades and bubble causing more bubble shredding and increased holdup.
- In HSPBT experiments, optical probe detected significantly more gas bubbles below the impeller blade trailing edge in comparison to other radial positions. It was also noted that finer bubbles tend to concentrate near the impeller trailing edge and tank centre than the tank wall. Furthermore, bubble population classification suggested that HSPBT45° generated a number of smaller bubbles than larger bubbles. It was also observed that increase in the blade angle increased overall gas holdup and gas fraction of larger bubbles at the expense of power dissipation.

## **6.2 RECOMMENDATIONS FOR FUTURE WORK**

Optical probe measurements on local bubble hydrodynamics explained in Chapter-3 revealed that with vortex ingestion only marginal amount of gas was dispersed and the maximum gas holdup recorded was only 1.2%. Moreover, Figure-4.4b indicate that increase in impeller speed does not improve the spread in gas bubbles across the tank. Almost all the dispersed gas bubbles tend to concentrate around the impeller blades before escaping through the vortex. Most of the energy dissipated from the impeller to the fluid was utilised for the swirling motion resulting in poor axial circulation of bubbles causing reduced gas holdup especially in the regions near wall and tank bottom.

It is noteworthy that recently, Tamburini et al., (146) reported that power consumption of an unbaffled tank was an order of magnitude less in comparison to a baffled tank. In addition to this, vortex ingestion could eliminate the cost associated with compressor operation. Also, removal of sparger prevents fine solid particles clogging the sparger holes which leads to equipment downtime. Despite of the abovementioned

advantages, low gas holdup and poor axial liquid circulation limits the use of unbaffled tanks for industrial application.

One of the ways to improve liquid circulation and gas holdup without compromising on power consumption, the vortex should be broken without baffles. Commercially available vortex breakers used for liquid draining, or by using fractal structures can be explored to achieve this. Fractal structures are expected to consume less power without affecting the flow pattern significantly as compared to commercially available baffles. Recent advances in additive manufacturing can be used to design and develop various fractal structures.

There is a surge in the usage of unbaffled tank for solid suspension applications along with gas dispersion. It is expected that the addition of solids might alter the flow field and vortex shape. In order to design an unbaffled tank for industrial application, hydrodynamics of unbaffled GLS-STs need to be quantified. It is expected that solids will have significant impact on vortex shape and bubble hydrodynamics. Detailed experimental as well as computational studies are needed to understand this. Discrete particle modelling (DPM) simulation of the system will be required to understand the behaviour of solids and their interaction with liquid and gas phase.

Modelling of a three phase GLS-ST at high solid loading and dense gas flow conditions is complex due to poor understanding of local data and interaction between phases. Local bubble hydrodynamics and particle velocity distribution data on 0.45 m pilot scale baffled GLS-ST reported in this study will be useful for the validation of CFD models at low solid loading. The validated models could be further used for detailed numerical analysis of GLS-STs at high solid loading. Furthermore, to account for the bubble-particle, particle-particle, and dispersed phase-wall interactions, drag force, coefficient of restitution, and turbulence need to be examined.

Nevertheless, local bubble hydrodynamics are still dependent on the size of tank which limits the CFD validation on industrial scale tanks due to inadequate data (75). Therefore, scale up studies are inevitable to understand the spatial distribution of gas phase with respect to tank size. Keeping this in view, the data obtained in the 0.45 m tank should be compared with experimental data at larger scale. This comparison will reveal the similarities and differences across the scales and would be invaluable for industrial scale operations.

In this thesis impact of HSPBT's blade angle on gas phase hydrodynamics and power consumption was reported in detail. During the course of research, it was observed that for applications which required less gas dispersion (e.g: waste water treatment), there is a rising industrial demand to develop new impellers with gas dispersion efficiency between LSPBT and HSPBT. LSPBTs consume less power in comparison with HSPBT but suffer from poor gas dispersion and high torque instability. Validated CFD models can be used to evolve efficient impeller shapes and develop tailored impeller for specific applications. The data presented in this thesis would be important for validation of CFD models especially at high gassing rates, and with solid loading.

## References

1. Sardeshpande MV, Gupta S, Ranade VV. Electrical resistance tomography for gas holdup in a gas-liquid stirred tank reactor. *Chemical Engineering Science*. 2017.
2. Bakker A. *Hydrodynamics of stirred gas-liquid dispersions*. 1992.
3. Tatterson GB. *Fluid mixing and gas dispersion in agitated tanks*: McGraw-Hill Companies; 1991.
4. Ford JJ, Heindel TJ, Jensen TC, Drake JB. X-ray computed tomography of a gas-sparged stirred-tank reactor. *Chemical Engineering Science*. 2008;63(8):2075-85.
5. Lee JH, Foster NR. Mass transfer and solubility of oxygen and methane in silicone fluids. *Industrial & engineering chemistry research*. 1990;29(4):691-6.
6. Greaves M, Barigou M, editors. Estimation of gas hold-up and impeller power in a stirred vessel reactor. *Fluid Mixing III, Inst Chem Eng, Int Chem Eng Symp Series*; 1988.
7. Smith J. Simple performance correlations for agitated vessels. *Fluid Mechanics of Mixing*: Springer; 1992. p. 55-63.
8. Rewatkar V, Joshi J. Role of sparger design on gas dispersion in mechanically agitated gas-liquid contactors. *The Canadian Journal of Chemical Engineering*. 1993;71(2):278-91.
9. Yawalkar AA, Pangarkar VG, Beenackers AA. Gas hold-up in stirred tank reactors. *The Canadian Journal of Chemical Engineering*. 2002;80(1):158-66.
10. Aubin J, Le Sauze N, Bertrand J, Fletcher DF, Xuereb C. PIV measurements of flow in an aerated tank stirred by a down-and an up-pumping axial flow impeller. *Experimental Thermal and Fluid Science*. 2004;28(5):447-56.
11. Khopkar A, Rammohan A, Ranade V, Dudukovic M. Gas-liquid flow generated by a Rushton turbine in stirred vessel: CARPT/CT measurements and CFD simulations. *Chemical Engineering Science*. 2005;60(8):2215-29.
12. Khopkar AR, Aubin J, Xuereb C, Le Sauze N, Bertrand J, Ranade VV. Gas-Liquid Flow Generated by a Pitched-Blade Turbine: Particle Image Velocimetry Measurements and Computational Fluid Dynamics Simulations. *Industrial & engineering chemistry research*. 2003;42(21):5318-32.
13. Bashiri H, Alizadeh E, Bertrand F, Chaouki J. Article 2: Investigation of Turbulent Fluid Flows in Stirred Tanks using a Non-Invasive Particle Tracking. *Numerical and Experimental Investigation of Liquid and Gas/Liquid Flows in Stirred Tank Reactors*. 2015:97.
14. Montante G, Horn D, Paglianti A. Gas-liquid flow and bubble size distribution in stirred tanks. *Chemical engineering science*. 2008;63(8):2107-18.
15. Lee BW, Dudukovic MP. Determination of flow regime and gas holdup in gas-liquid stirred tanks. *Chemical Engineering Science*. 2014;109:264-75.
16. Alves S, Maia C, Vasconcelos J, Serralheiro A. Bubble size in aerated stirred tanks. *Chemical Engineering Journal*. 2002;89(1):109-17.

17. Laakkonen M, Honkanen M, Saarenrinne P, Aittamaa J. Local bubble size distributions, gas–liquid interfacial areas and gas holdups in a stirred vessel with particle image velocimetry. *Chemical Engineering Journal*. 2005;109(1):37-47.
18. Wild G, Poncin S, Reactors T-PS. Gordon and Breach Science Publishers. Amsterdam; 1996.
19. Murthy B, Ghadge R, Joshi J. CFD simulations of gas–liquid–solid stirred reactor: Prediction of critical impeller speed for solid suspension. *Chemical Engineering Science*. 2007;62(24):7184-95.
20. Dohi N, Takahashi T, Minekawa K, Kawase Y. Power consumption and solid suspension performance of large-scale impellers in gas–liquid–solid three-phase stirred tank reactors. *Chemical Engineering Journal*. 2004;97(2-3):103-14.
21. Van Deventer J, Ross V. The dynamic simulation of carbon-in-pulp systems: A review of recent developments. *Minerals Engineering*. 1991;4(7-11):667-81.
22. Yang S, Li X, Yang C, Ma B, Mao Z-S. Computational Fluid Dynamics Simulation and Experimental Measurement of Gas and Solid Holdup Distributions in a Gas–Liquid–Solid Stirred Reactor. *Industrial & Engineering Chemistry Research*. 2015;55(12):3276-86.
23. Van den Akker HE. The details of turbulent mixing process and their simulation. *Advances in Chemical Engineering*. 2006;31:151-229.
24. Mueller SG. Optical measurements in gas-liquid stirred tanks: Washington University in St. Louis; 2009.
25. Lee BW. Optical Probes in Multiphase Reactors: Washington University in St. Louis; 2016.
26. Bao Y, Chen L, Gao Z, Chen J. Local void fraction and bubble size distributions in cold-gassed and hot-sparged stirred reactors. *Chemical Engineering Science*. 2010;65(2):976-84.
27. Ranade V, Perrard M, Le Sauze N, Xuereb C, Bertrand J. Trailing vortices of Rushton turbine: PIV measurements and CFD simulations with snapshot approach. *Chemical Engineering Research and Design*. 2001;79(1):3-12.
28. Schäfer M, Wächter P, Durst F, editors. Experimental investigation of local bubble size distributions in stirred vessels using phase Doppler anemometry. 10th European Conference on Mixing; 2000: Elsevier.
29. Abdullah B, Dave C, Nguyen T-H, Cooper CG, Adesina AA. Electrical resistance tomography-assisted analysis of dispersed phase hold-up in a gas-inducing mechanically stirred vessel. *Chemical engineering science*. 2011;66(22):5648-62.
30. Devanathan N, Moslemian D, Dudukovic M. Flow mapping in bubble columns using CARPT. *Chemical Engineering Science*. 1990;45(8):2285-91.
31. Scargiali F, Tamburini A, Caputo G, Micale G. On the assessment of power consumption and critical impeller speed in vortexing unbaffled stirred tanks. *Chemical Engineering Research and Design*. 2017;123:99-110.
32. Scargiali F, Busciglio A, Grisafi F, Brucato A. Mass transfer and hydrodynamic characteristics of unbaffled stirred bio-reactors: influence of impeller design. *Biochemical Engineering Journal*. 2014;82:41-7.

33. Tamburini A, Cipollina A, Scargiali F, Micale G, Brucato A. Power Requirements for Complete Suspension and Aeration in an Unbaffled Bioslurry Reactor. *CHEMICAL ENGINEERING*. 2016;49.
34. Nienow A. On impeller circulation and mixing effectiveness in the turbulent flow regime. *Chemical Engineering Science*. 1997;52(15):2557-65.
35. Nienow A, Bujalski W. Recent studies on agitated three-phase (gas–solid–liquid) systems in the turbulent regime. *Chemical Engineering Research and Design*. 2002;80(8):832-8.
36. Kopic A, Heindel T. Correlating gas-liquid mass transfer in a stirred-tank reactor. *Chemical Engineering Research and Design*. 2006;84(3):239-45.
37. Wadnerkar D, Utikar RP, Tade MO, Pareek VK. CFD simulation of solid–liquid stirred tanks. *Advanced Powder Technology*. 2012;23(4):445-53.
38. Wadnerkar D, Tade MO, Pareek VK, Utikar RP. CFD simulation of solid–liquid stirred tanks for low to dense solid loading systems. *Particuology*. 2016;29:16-33.
39. McFarlane CM, Nienow AW. Studies of high solidity ratio hydrofoil impellers for aerated bioreactors. 1. Review. *Biotechnology progress*. 1995;11(6):601-7.
40. McFarlane CM, Zhao XM, Nienow AW. Studies of High Solidity Ratio Hydrofoil Impellers for Aerated Bioreactors. 2. Air—Water Studies. *Biotechnology progress*. 1995;11(6):608-18.
41. Hassan I, Robinson CW. Stirred-tank mechanical power requirement and gas holdup in aerated aqueous phases. *AIChE Journal*. 1977;23(1):48-56.
42. Yung C, Wong C, Chang C. Gas holdup and aerated power consumption in mechanically stirred tanks. *The Canadian Journal of Chemical Engineering*. 1979;57(6):672-6.
43. Lu W-M, Ju S-J. Local gas holdup, mean liquid velocity and turbulence in an aerated stirred tank using hot-film anemometry. *The Chemical Engineering Journal*. 1987;35(1):9-17.
44. Wang W, Mao Z-S, Yang C. Experimental and numerical investigation on gas holdup and flooding in an aerated stirred tank with Rushton impeller. *Industrial & engineering chemistry research*. 2006;45(3):1141-51.
45. Sun H, Mao Z-S, Yu G. Experimental and numerical study of gas hold-up in surface aerated stirred tanks. *Chemical engineering science*. 2006;61(12):4098-110.
46. Bombac A, Zun I, Filipic B, Zumer M. Gas-filled cavity structures and local void fraction distribution in aerated stirred vessel. *American Institute of Chemical Engineers AIChE Journal*. 1997;43(11):2921.
47. Machon V, Pacek A, Nienow A. Bubble sizes in electrolyte and alcohol solutions in a turbulent stirred vessel. *Chemical Engineering Research and Design*. 1997;75(3):339-48.
48. Mueller SG, Dudukovic MP. Gas holdup in gas– liquid stirred tanks. *Industrial & Engineering Chemistry Research*. 2010;49(21):10744-50.

49. Hampel U, Hristov H, Bieberle A, Zippe C. Application of high-resolution gamma ray tomography to the measurement of gas hold-up distributions in a stirred chemical reactor. *Flow Measurement and Instrumentation*. 2007;18(5):184-90.
50. Moucha T, Linek V, Prokopová E. Gas hold-up, mixing time and gas-liquid volumetric mass transfer coefficient of various multiple-impeller configurations: Rushton turbine, pitched blade and techmix impeller and their combinations. *Chemical Engineering Science*. 2003;58(9):1839-46.
51. Rewatkar V, Deshpande A, Pandit A, Joshi J. Gas hold-up behavior of mechanically agitated gas-liquid reactors using pitched blade downflow turbines. *The Canadian Journal of Chemical Engineering*. 1993;71(2):226-37.
52. Boden S, Bieberle M, Hampel U. Quantitative measurement of gas hold-up distribution in a stirred chemical reactor using X-ray cone-beam computed tomography. *Chemical Engineering Journal*. 2008;139(2):351-62.
53. Bouaifi M, Hebrard G, Bastoul D, Roustan M. A comparative study of gas hold-up, bubble size, interfacial area and mass transfer coefficients in stirred gas-liquid reactors and bubble columns. *Chemical engineering and processing: Process intensification*. 2001;40(2):97-111.
54. Hristov HV, Stephan B, Uwe H, Holger K, Günther H, Wilfried S. A study on the two-phase flow in a stirred tank reactor agitated by a gas-inducing turbine. *chemical engineering research and design*. 2008;86(1):75-81.
55. Kong L-n, Li W, Han L-c, Liu Y-j, Luo H-a, Al Dahhan M, et al. On the measurement of gas holdup distribution near the region of impeller in a gas-liquid stirred Rushton tank by means of  $\gamma$ -CT. *Chemical engineering journal*. 2012;188:191-8.
56. Thatte A, Ghadge R, Patwardhan A, Joshi J, Singh G. Local gas holdup measurement in sparged and aerated tanks by  $\gamma$ -ray attenuation technique. *Industrial & engineering chemistry research*. 2004;43(17):5389-99.
57. Laakkonen M, Moilanen P, Miettinen T, Saari K, Honkanen M, Saarenrinne P, et al. Local bubble size distributions in agitated vessel: comparison of three experimental techniques. *Chemical Engineering Research and Design*. 2005;83(1):50-8.
58. Saravanan K, Joshi J. Fractional gas hold-up in gas inducing type of mechanically agitated contactors. *The Canadian Journal of Chemical Engineering*. 1996;74(1):16-30.
59. Montante G, Paglianti A. Gas hold-up distribution and mixing time in gas-liquid stirred tanks. *Chemical Engineering Journal*. 2015;279:648-58.
60. Lee BW, Dudukovic MP. Time-series analysis of optical probe measurements in gas-liquid stirred tanks. *Chemical Engineering Science*. 2014;116:623-34.
61. Rousar I, Van den Akker H, editors. LDA measurements of liquid velocities in sparged agitated tanks with single and multiple Rushton turbines. *Institution of Chemical Engineers Symposium Series*; 1994: HEMISPHERE PUBLISHING CORPORATION.
62. Deen NG, Hjertager BrH. Particle image velocimetry measurements in an aerated stirred tank. *Chemical Engineering Communications*. 2002;189(9):1208-21.

63. Hassan IT, Robinson CW. Mass-transfer-effective bubble coalescence frequency and specific interfacial area in a mechanically agitated gas-liquid contactor. *Chemical Engineering Science*. 1980;35(6):1277-89.
64. Kawecki W, Reith T, Van Heuven J, Beek W. Bubble size distribution in the impeller region of a stirred vessel. *Chemical Engineering Science*. 1967;22(11):1519-23.
65. Barigou M, Greaves M. Bubble-size distributions in a mechanically agitated gas—liquid contactor. *Chemical Engineering Science*. 1992;47(8):2009-25.
66. Parthasarathy R, Ahmed N. Bubble size distribution in a gas sparged vessel agitated by a Rushton turbine. *Industrial & engineering chemistry research*. 1994;33(3):703-11.
67. Bao Y, Wang B, Lin M, Gao Z, Yang J. Influence of impeller diameter on overall gas dispersion properties in a sparged multi-impeller stirred tank. *Chinese Journal of Chemical Engineering*. 2015;23(6):890-6.
68. Alves S, Maia C, Vasconcelos J. Experimental and modelling study of gas dispersion in a double turbine stirred tank. *Chemical Engineering Science*. 2002;57(3):487-96.
69. Laakkonen M, Alopaeus V, Aittamaa J. Validation of bubble breakage, coalescence and mass transfer models for gas–liquid dispersion in agitated vessel. *Chemical engineering science*. 2006;61(1):218-28.
70. Kerdouss F, Bannari A, Proulx P. CFD modeling of gas dispersion and bubble size in a double turbine stirred tank. *Chemical Engineering Science*. 2006;61(10):3313-22.
71. Laakkonen M, Moilanen P, Alopaeus V, Aittamaa J. Modelling local bubble size distributions in agitated vessels. *Chemical Engineering Science*. 2007;62(3):721-40.
72. Sungkorn R, Derksen J, Khinast J. Euler–Lagrange modeling of a gas–liquid stirred reactor with consideration of bubble breakage and coalescence. *AIChE Journal*. 2012;58(5):1356-70.
73. Van den Hengel E, Deen N, Kuipers J. Application of coalescence and breakup models in a discrete bubble model for bubble columns. *Industrial & engineering chemistry research*. 2005;44(14):5233-45.
74. Deen NG, Solberg T, Hjertager BH. Large eddy simulation of the gas–liquid flow in a square cross-sectioned bubble column. *Chemical Engineering Science*. 2001;56(21):6341-9.
75. Nauha EK, Kálal Z, Ali JM, Alopaeus V. Compartmental modeling of large stirred tank bioreactors with high gas volume fractions. *Chemical Engineering Journal*. 2018;334:2319-34.
76. Li L, Xu B. Numerical simulation of flow field characteristics in a gas-liquid-solid agitated tank. *Korean Journal of Chemical Engineering*. 2016;33(7):2007-17.
77. Davoody M, Abdul Raman AAB, Parthasarathy R. Maximizing impeller power efficiency in gas–solid–liquid stirred vessels through process intensification. *Industrial & Engineering Chemistry Research*. 2015;54(47):11915-28.



78. Bao Y, Hao Z, Gao Z, Shi L, Smith JM, Thorpe RB. Gas dispersion and solid suspension in a three-phase stirred tank with multiple impellers. *Chemical Engineering Communications*. 2006;193(7):801-25.
79. Murthy B, Kasundra R, Joshi J. Hollow self-inducing impellers for gas–liquid–solid dispersion: Experimental and computational study. *Chemical Engineering Journal*. 2008;141(1):332-45.
80. Conway K, Kyle A, Rielly CD. Gas–liquid–solid operation of a vortex-ingesting stirred tank reactor. *Chemical Engineering Research and Design*. 2002;80(8):839-45.
81. Dohi N, Takahashi T, Minekawa K, Kawase Y. Power consumption and solid suspension performance of large-scale impellers in gas–liquid–solid three-phase stirred tank reactors. *Chemical Engineering Journal*. 2004;97(2):103-14.
82. Busciglio A, Caputo G, Scargiali F. Free-surface shape in unbaffled stirred vessels: Experimental study via digital image analysis. *Chemical Engineering Science*. 2013;104:868-80.
83. Busciglio A, Scargiali F, Grisafi F, Brucato A. Oscillation dynamics of free vortex surface in uncovered unbaffled stirred vessels. *Chemical Engineering Journal*. 2016;285:477-86.
84. Busciglio A, Montante G, Kracík T, Moucha T, Paglianti A. Rotary sloshing induced by impeller action in unbaffled stirred vessels. *Chemical Engineering Journal*. 2017;317:433-43.
85. NAGATA S, NISHIKAWA M, INOUE A, OKAMOTO Y. Turbulence in non-baffled mixing vessel. *Journal of Chemical Engineering of Japan*. 1975;8(3):243-8.
86. Deshpande S, Kar K, Walker J, Pressler J, Su W. An experimental and computational investigation of vortex formation in an unbaffled stirred tank. *Chemical Engineering Science*. 2017;168:495-506.
87. Mahmud T, Haque JN, Roberts KJ, Rhodes D, Wilkinson D. Measurements and modelling of free-surface turbulent flows induced by a magnetic stirrer in an unbaffled stirred tank reactor. *Chemical Engineering Science*. 2009;64(20):4197-209.
88. Haque J, Mahmud T, Roberts K, Liang J, White G, Wilkinson D, et al. Free-surface turbulent flow induced by a Rushton turbine in an unbaffled dish-bottom stirred tank reactor: LDV measurements and CFD simulations. *The Canadian Journal of Chemical Engineering*. 2011;89(4):745-53.
89. Montante G, Magelli F, Paglianti A. Fluid-dynamics characteristics of a vortex-ingesting stirred tank for biohydrogen production. *Chemical Engineering Research and Design*. 2013;91(11):2198-208.
90. Lamberto D, Alvarez M, Muzzio F. Experimental and computational investigation of the laminar flow structure in a stirred tank. *Chemical Engineering Science*. 1999;54(7):919-42.
91. Boyer C, Duquenne A-M, Wild G. Measuring techniques in gas–liquid and gas–liquid–solid reactors. *Chemical Engineering Science*. 2002;57(16):3185-215.
92. Wang G, Li X, Yang C, Li G, Mao Z-S. New vision probe based on telecentric photography and its demonstrative applications in a multiphase stirred reactor. *Industrial & Engineering Chemistry Research*. 2017.

93. Galletti C, Brunazzi E. On the main flow features and instabilities in an unbaffled vessel agitated with an eccentrically located impeller. *Chemical Engineering Science*. 2008;63(18):4494-505.
94. Galletti C, Pintus S, Brunazzi E. Effect of shaft eccentricity and impeller blade thickness on the vortices features in an unbaffled vessel. *Chemical Engineering Research and Design*. 2009;87(4):391-400.
95. Rieger F, Ditzl P, Novak V. Vortex depth in mixed unbaffled vessels. *Chemical Engineering Science*. 1979;34(3):397-403.
96. Assirelli M, Bujalski W, Eaglesham A, Nienow AW. Macro-and micromixing studies in an unbaffled vessel agitated by a Rushton turbine. *Chemical Engineering Science*. 2008;63(1):35-46.
97. Glover GC, Fitzpatrick J. Modelling vortex formation in an unbaffled stirred tank reactors. *Chemical Engineering Journal*. 2007;127(1):11-22.
98. Montante G, Bakker A, Paglianti A, Magelli F. Effect of the shaft eccentricity on the hydrodynamics of unbaffled stirred tanks. *Chemical engineering science*. 2006;61(9):2807-14.
99. Lamarque N, Zoppé B, Lebaigue O, Dolias Y, Bertrand M, Ducros F. Large-eddy simulation of the turbulent free-surface flow in an unbaffled stirred tank reactor. *Chemical Engineering Science*. 2010;65(15):4307-22.
100. Gimbutis J, Rielly CD, Nagy ZK, Derksen J. Detached eddy simulation on the turbulent flow in a stirred tank. *AIChE Journal*. 2012;58(10):3224-41.
101. Akita K, Yoshida F. Bubble size, interfacial area, and liquid-phase mass transfer coefficient in bubble columns. *Industrial & Engineering Chemistry Process Design and Development*. 1974;13(1):84-91.
102. Chaouki J, Larachi F, Duduković MP. Noninvasive tomographic and velocimetric monitoring of multiphase flows. *Industrial & engineering chemistry research*. 1997;36(11):4476-503.
103. Wang M, Dorward A, Vlaev D, Mann R. Measurements of gas-liquid mixing in a stirred vessel using electrical resistance tomography (ERT). *Chemical Engineering Journal*. 2000;77(1):93-8.
104. Marashdeh Q, Fan L-S, Du B, Warsito W. Electrical Capacitance Tomography- A Perspective. *Industrial & Engineering Chemistry Research*. 2008;47(10):3708-19.
105. Veera UP. Gamma ray tomography design for the measurement of hold-up profiles in two-phase bubble columns. *Chemical Engineering Journal*. 2001;81(1):251-60.
106. Li Z, Bao Y, Gao Z. PIV experiments and large eddy simulations of single-loop flow fields in Rushton turbine stirred tanks. *Chemical Engineering Science*. 2011;66(6):1219-31.
107. Sharp K, Adrian R. PIV study of small-scale flow structure around a Rushton turbine. *AIChE Journal*. 2001;47(4):766-78.
108. Aubin J, Mavros P, Fletcher DF, Bertrand J, Xuereb C. Effect of axial agitator configuration (up-pumping, down-pumping, reverse rotation) on flow patterns

generated in stirred vessels. *Chemical Engineering Research and Design*. 2001;79(8):845-56.

109. Congjing R, Xiaojing J, Jingdai W, Yongrong Y, Xiaohuan Z. Determination of critical speed for complete solid suspension using acoustic emission method based on multiscale analysis in stirred tank. *Industrial & Engineering Chemistry Research*. 2008;47(15):5323-7.

110. Wichterle K. Conditions for suspension of solids in agitated vessels. *Chemical engineering science*. 1988;43(3):467-71.

111. Rieger F, Dittl P. Suspension of solid particles. *Chemical Engineering Science*. 1994;49(14):2219-27.

112. Nienow A. Suspension of solid particles in turbine agitated baffled vessels. *Chemical Engineering Science*. 1968;23(12):1453-9.

113. Manasseh R, LaFontaine R, Davy J, Shepherd I, Zhu Y-G. Passive acoustic bubble sizing in sparged systems. *Experiments in Fluids*. 2001;30(6):672-82.

114. Prasser H-M, Scholz D, Zippe C. Bubble size measurement using wire-mesh sensors. *Flow measurement and Instrumentation*. 2001;12(4):299-312.

115. Pietruske H, Prasser H-M. Wire-mesh sensors for high-resolving two-phase flow studies at high pressures and temperatures. *Flow measurement and instrumentation*. 2007;18(2):87-94.

116. Dos Santos EN, Schleicher E, Reinecke S, Hampel U, Da Silva MJ. Quantitative cross-sectional measurement of solid concentration distribution in slurries using a wire-mesh sensor. *Measurement Science and Technology*. 2015;27(1):015301.

117. Besagni G, Brazzale P, Fiocca A, Inzoli F. Estimation of bubble size distributions and shapes in two-phase bubble column using image analysis and optical probes. *Flow Measurement and Instrumentation*. 2016;52:190-207.

118. Tyagi P, Buwa VV. Dense gas-liquid-solid flow in a slurry bubble column: Measurements of dynamic characteristics, gas volume fraction and bubble size distribution. *Chemical Engineering Science*. 2017;173:346-62.

119. Manjrekar ON, Dudukovic MP. Application of a 4-point optical probe to a Slurry Bubble Column Reactor. *Chemical Engineering Science*. 2015;131:313-22.

120. Sensors AP. [www.a2photonicsensors.com/](http://www.a2photonicsensors.com/)

121. Prakash B, Shah MT, Pareek VK, Utikar RP. Impact of HSPBT blade angle on gas phase hydrodynamics in a gas-liquid stirred tank. *Chemical Engineering Research and Design*. 2018;130:219-29.

122. Cartellier A. Simultaneous void fraction measurement, bubble velocity, and size estimate using a single optical probe in gas-liquid two-phase flows. *Review of Scientific Instruments*. 1992;63(11):5442-53.

123. Xue J, Al-Dahhan M, Dudukovic M, Mudde R. Four-point optical probe for measurement of bubble dynamics: Validation of the technique. *Flow Measurement and Instrumentation*. 2008;19(5):293-300.

124. Guet S, Fortunati RV, Mudde RF, Ooms G. Bubble Velocity and Size Measurement with a Four-Point Optical Fiber Probe. *Particle & Particle Systems Characterization*. 2003;20(3):219-30.
125. Xue J, Al-Dahhan M, Dudukovic MP, Mudde RF. Bubble Dynamics Measurements Using Four-Point Optical Probe. *The Canadian Journal of Chemical Engineering*. 2003;81(3-4):375-81.
126. Xue J, Al-Dahhan M, Dudukovic M, Mudde R. Bubble velocity, size, and interfacial area measurements in a bubble column by four-point optical probe. *AIChE journal*. 2008;54(2):350-63.
127. Kiambi S, Duquenne AM, Dupont JB, Colin C, Risso F, Delmas H. Measurements of bubble characteristics: comparison between double optical probe and imaging. *The Canadian Journal of Chemical Engineering*. 2003;81(3-4):764-70.
128. Töger J, Bidhult SL, Revstedt J, Carlsson M, Arheden H, Heiberg E. Phantom validation of 4D flow: independent validation of flow velocity quantification using particle imaging velocimetry. *Journal of Cardiovascular Magnetic Resonance*. 2015;17(1):O18.
129. Kim H, Hertzberg J, Shandas R. Development and validation of echo PIV. *Experiments in Fluids*. 2004;36(3):455-62.
130. De Jong J, Odu S, Van Buijtenen M, Deen N, van Sint Annaland M, Kuipers J. Development and validation of a novel digital image analysis method for fluidized bed particle image velocimetry. *Powder technology*. 2012;230:193-202.
131. Cheng Y, Diez F. A 4D imaging tool for Lagrangian particle tracking in stirred tanks. *AIChE Journal*. 2011;57(8):1983-96.
132. Melling A. Tracer particles and seeding for particle image velocimetry. *Measurement Science and Technology*. 1997;8(12):1406.
133. Parisien V, Farrell A, Pjontek D, McKnight CA, Wiens J, Macchi A. Bubble swarm characteristics in a bubble column under high gas holdup conditions. *Chemical Engineering Science*. 2017;157:88-98.
134. Tyagi P, Buwa VV. Experimental characterization of dense gas–liquid flow in a bubble column using voidage probes. *Chemical Engineering Journal*. 2017;308:912-28.
135. Rampure MR, Kulkarni AA, Ranade VV. Hydrodynamics of bubble column reactors at high gas velocity: experiments and computational fluid dynamics (CFD) simulations. *Industrial & Engineering Chemistry Research*. 2007;46(25):8431-47.
136. Lau Y, Sujatha KT, Gaeini M, Deen N, Kuipers J. Experimental study of the bubble size distribution in a pseudo-2D bubble column. *Chemical Engineering Science*. 2013;98:203-11.
137. Li L, Wang J, Feng L, Gu X. Computational fluid dynamics simulation of hydrodynamics in an uncovered unbaffled tank agitated by pitched blade turbines. *Korean Journal of Chemical Engineering*. 2017;34(11):2811-22.
138. Gumulya M, Utikar R, Evans G, Joshi J, Pareek V. Interaction of bubbles rising inline in quiescent liquid. *Chemical Engineering Science*. 2017;166:1-10.
139. Nagata S. *Mixing: principles and applications*: Halsted Press; 1975.

140. Deen NG, Solberg T, Hjertager BH. Flow Generated by an Aerated Rushton Impeller: Two-phase PIV Experiments and Numerical Simulations. *The Canadian Journal of Chemical Engineering*. 2002;80(4):1-15.
141. Morud K, Hjertager B. LDA measurements and CFD modelling of gas-liquid flow in a stirred vessel. *Chemical Engineering Science*. 1996;51(2):233-49.
142. Kumaresan T, Joshi JB. Effect of impeller design on the flow pattern and mixing in stirred tanks. *Chemical Engineering Journal*. 2006;115(3):173-93.
143. Mueller S. Optical measurements in gas-liquid stirred tanks. 2009.
144. Zwietering TN. Suspending of solid particles in liquid by agitators. *Chemical Engineering Science*. 1958;8(3-4):244-53.
145. Warmoeskerken MM, Speur J, Smith JM. Gas-liquid dispersion with pitched blade turbines. *Chemical Engineering Communications*. 1984;25(1-6):11-29.
146. Tamburini A, Cipollina A, Micale G, Brucato A. Measurements of Njs and power requirements in unbaffled bioslurry reactors. *CHEMICAL ENGINEERING*. 2012;27.

*Every reasonable effort has been made to acknowledge the owners of copyright material. I would be pleased to hear from any copyright owner who has been omitted or incorrectly acknowledged.*